Electrochemical & Thermochemical Behavior of CeO$_{2-\delta}$

Thesis by

William C. Chueh

In Partial Fulfillment of the Requirements for the Degree of Doctor of Philosophy
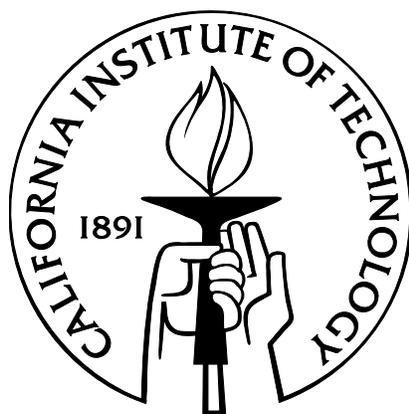
California Institute of Technology

Pasadena, California

2011

(Defended September 24, 2010)

Acknowledgements

1. W. C. Chueh, C. Falter, M. Abbott, D. Scipio, P. Furler, S. M. Haile & A. Steinfeld. High-Flux Solar-Thermochemical CO_2 & H_2O Dissociation using Nonstoichiometric Ceria. *Science* **330**, 1797-1801 (2010).

2. F. Ciucci*, W. C. Chueh*, D. G. Goodwin & S. M. Haile. Surface Reaction & Transport in Mixed Conductors with Electrochemically-Active Surfaces: A 2-D Numerical Study of Ceria. *Phys. Chem. Chem. Phys.* **13**, 2121-2135 (2011). (*Equal contribution authors)

3. W. C. Chueh & S. M. Haile. Thermochemical Study of Ceria: Exploiting an Old Material for New Modes of Energy Conversion of CO_2 Mitigation. *Phil. Trans. R. Soc. A*. **368**, 3269-3294 (2010).

4. W. C. Chueh & S. M. Haile. Electrochemical Studies of Capacitance in Cerium Oxide Thin Films and Its Relationship to Anionic and Electronic Defect Densities. *Phys. Chem. Chem. Phys.* **11**, 8144-8148 (2009).

5. W. C. Chueh & S. M. Haile. Ceria as a Thermochemical Reaction Medium for Selectively Generating Syngas or Methane from H_2O & CO_2. *Chem. Sus. Chem.* **2**, 735-739 (2009).

6. W. C. Chueh, W. Lai & S. M. Haile. Electrochemical Behavior of Ceria with Selected Metal Electrodes. *Solid State Ionics* **179**, 1036 - 1041 (2008).

Abstract

The mixed-valent nature of nonstoichiometric ceria ($CeO_{2-\delta}$) gives rise to a wide range of intriguing properties, such as mixed ionic and electronic conduction and oxygen storage. Surface and transport behavior in rare-earth (samaria) doped and undoped ceria were investigated, with particular emphasis on applications in electrochemical and thermochemical energy conversion processes such as fuel cells and solar fuel production. The electrochemical responses of bulk-processed ceria with porous Pt and Au electrodes were analyzed using 1-D and 2-D transport models to decouple surface reactions, near-surface transport and bulk transport. Combined experimental and numerical results indicate that hydrogen electro-oxidation and hydrolysis near open-circuit conditions occur preferentially over the ceria | gas interface rather than over the ceria | gas | metal interface, with the rate-limiting step likely to be either surface reaction or transport through the surface oxygen vacancy depletion layer. In addition, epitaxial thin films of ceria were grown on zirconia substrates using pulsed-laser deposition to examine electrocatalysis over well-defined microstructures. Physical models were derived to analyze the electrochemical impedance response. By varying the film thickness, interfacial and chemical capacitance were decoupled, with the latter shown to be proportional to the small polaron densities. The geometry of microfabricated metal current collectors (metal = Pt, Ni) was also systematically varied to investigate the relative activity of the ceria | gas and the ceria | metal | gas interfaces. The data suggests that the electrochemical activity of the metal-ceria composite is only weakly dependent on the metal due to the relatively high activity of the ceria | gas interface. In addition to electrochemical experiments, thermochemical reduction-oxidation studies were performed on ceria. It was shown that thermally-reduced ceria, upon exposure to H_2O and/or CO_2, can be

reoxidized to form H_2, CO, and/or CH_4. Analysis of gas evolution rates confirms that the kinetics of ceria oxidation by H_2O and CO_2 are dominated by surface reactions, rather than by ambipolar oxygen diffusion. Temperature-programmed oxidation experiments revealed that, even under thermodynamically favored conditions, carbonaceous species do not form on the surface of neat ceria, thereby giving a high CO selectivity when dissociating CO_2. A scaled-up ceria-based solar reactor was designed and tested to demonstrate the feasibility of solar fuel production via thermochemical cycling.

Table of Contents

List of Figures

List of Tables

List of Symbols & Notations

μ	chemical potential
μ^0	chemical potential at standard state
$\tilde{\mu}$	electrochemical potential
$\tilde{\mu}^*$	reduced electrochemical potential
e	elementary charge
z	formal charge
ϕ	electric potential
ϕ^*	non-dimensional electric potential
k_B	Boltzmann constant
T	temperature
c	carrier concentration
c^0	carrier concentration at standard state
c^{eq}	equilibrium carrier concentration
c^*	non-dimensional carrier concentration
ΔG^0	standard Gibbs free energy of reaction
p^*	gas activity
p^{*eq}	equilibrium gas activity
$\mathbf{j}^{chg}$	charge flux
D	diffusion coefficient
ε	permittivity
k	surface reaction rate-constant
k^0	partial-pressure independent surface reaction rate-constant
I^{IP}	in-plane current
I^{CP}	cross-plane current
σ	conductivity

R	resistance
$R_{ion}^{\perp}$	electrode resistance
$\tilde{R}_{ion}^{\perp}$	electrode resistance normalized by the total electrode area ($W_1 + W_2$); identical to the conventional, macroscopically defined interfacial resistance
$\tilde{R}_{ion}^{*\perp}$	electrode resistance normalized by the active reaction area (W_2)
R_{rxn}	surface reaction resistance (tildes indicate normalization – see $\tilde{R}_{ion}^{\perp}$ & $\tilde{R}_{ion}^{*\perp}$)
R_{eon-DD}	in-plane electron diffusion-drift resistance
f_{surf}	fractional surface reaction resistance
W_1	half of metal current collector width
W_2	half of MIEC width exposed to gas
l	half of the sample thickness or thin film thickness
d_{SIZ}	depth of the surface-influence-zone

Superscripts

eq	equilibrium
*	dimensionless
(1)	perturbed
IP	in-plane
CP	cross-plane

Subscripts

ion	ionic species (oxygen vacancy)
eon	electronic species (polaron)
dop	dopant species
red	reduction (specifically for standard Gibbs free energy of oxide reduction)
oxd	oxidation (specifically for standard Gibbs free energy of oxide oxidation)
g	gas (specifically for standard Gibbs free energy for gas phase reaction of oxygen, hydrogen and water)
W	hydrogen oxidation to water (specifically for standard Gibbs free energy of

reaction

rxn   surface reaction (MIEC | gas interface)

eon-DD   electron diffusion-drift (between MIEC | metal and MIEC | gas interface)

Chapter 1

Introduction & Background

1.1 Motivation

Chemical bonds are one of the most effective mediums for storing energy because of their high energy densities. However, efficiencies for sustainable energy conversion (*e.g.* solar-to-fuel, and fuel-to-electricity) remain low and uncompetitive with those of conventional routes. In this work, fundamental surface reaction and transport properties of bulk and thin film cerium-based oxides (ceria) are investigated as they relate to the efficient production of solar fuel from H_2O and CO_2 (via thermochemical dissociation) and the subsequent conversion to electricity (via fuel cells) at elevated temperatures. As most chemical reactions are thermally activated, even a modest increase in the operating temperature can produce drastic effects on the rates and reduce or eliminate the use of precious elements.

Under ambient pressures and from room temperature to the melting point, fully oxidized ceria adopts the ideal cubic fluorite crystal structure, Figure 1.1. Under reducing conditions, a
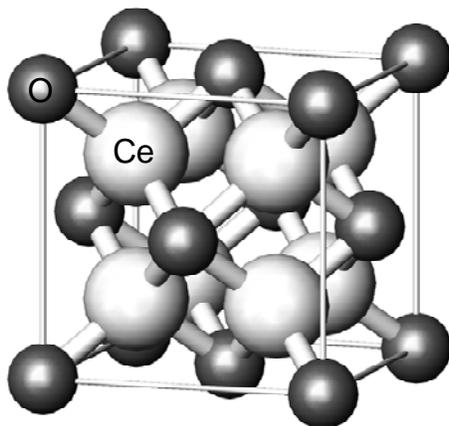
Figure 1.1: Cubic fluorite crystal structure.

portion of the Ce converts to the 3+ oxidation state, and the resulting electrons are charge balanced by oxygen vacancies, where δ in the stoichiometry $CeO_{2-\delta}$ represents the vacancy concentration. A remarkable feature of ceria, particularly at elevated temperatures, is that exceptionally high vacancy concentration can be accommodated without a change in crystallographic structure (or phase).[4] Furthermore, high oxygen vacancy mobility combined with mixed ionic and electronic conductions under reducing conditions make ceria a suitable material for catalytic and electro-catalytic applications.[5-6]

1.1.1 Application in Electrochemical Devices

Solid-state mixed ionic and electronic conductors (MIECs), such as ceria, have received significant attention as candidate materials for solid oxide fuel cell (SOFC) and solid oxide electrolyzer (SOEC) electrodes and electrolytes as well as electrochemical sensors.[7-10] Doped ceria has an exceptional ionic conductivity at intermediate temperatures ($\sigma_{ion} \approx 10^{-2}$ S cm^{-1} at 550 °C in air) and a moderate electronic conductivity under reducing atmospheres ($\sigma_{eon} \approx 10^{-2}$ S cm^{-1} at 550 °C, $p_{O_2} = 10^{-25}$ atm),[2,5,11-13] and was demonstrated as a viable electrolyte for high power fuel cells, delivering 1 W cm^{-2} power density at 600 °C.[14] As the fabrication of thin electrolytes, either by ceramics processing or by thin film deposition, is perfected, SOFCs and SOECs are increasingly limited by electrode activity.[15-16] Therefore, a better understanding of fundamental processes at the electrode is needed in order to design the next generation of intermediate-temperature fuel cells.

For oxygen-vacancy-conducting SOFCs, the cathode and anode global reactions are

$$O_2(g) + 2V_O^{\bullet\bullet} + 4e' \rightarrow 2O_O^{\times} \qquad (1.1)$$

$$2H_2(g) + 2O_O^{\times} \rightarrow 2H_2O(g) + 2V_O^{\bullet\bullet} + 4e' \qquad (1.2)$$
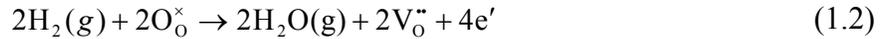
respectively, where the Kröger-Vink notation is used. In a SOEC, the reactions are reversed. At the active reaction sites, the appropriate reactions are catalyzed and electrons, gas species and oxygen ions (or vacancies) must be transported to and from these sites. In conventional, non-mixed-conducting fuel cell electrodes (*e.g.* Pt-(Y,Zr)O$_2$ cathodes and Ni-(Y,Zr)O$_2$ anodes), electrochemical reactions are limited to triple-phase boundaries (3PB) where electrode, electrolyte and gas phase are in simultaneous contact.[8,10] MIECs have the potential to broaden the electrochemical reaction zone beyond the 3PB since they conduct ions and electrons simultaneously. Recognition of this inherent advantage of MIECs has driven efforts to develop oxides with both high ionic and high electronic conductivity as solid oxide fuel cell anodes and/or cathodes.[7-9,14,17] Because of its moderate electronic conductivity and high ionic conductivity under reducing atmospheres, ceria has been used extensively in the anode, typically as a component in a metal-ceramic composite electrode.[11,18-27] Use of a ceria-based interlayer (placed between the electrolyte and the anode) was also shown to substantially improve performance.[18,24-25] Despite the wide use of ceria in fuel cell electrodes, however, knowledge of the electrochemical reaction pathways remains limited.

Consider the simplified metal-MIEC composite electrode structure shown in Figure 1.2. Reactions can take place on two types of macroscopic surface sites: (1) the 3PB reaction sites, and (2) the dual-phase-boundary (2PB) reaction sites where the MIEC meets the gas phase. Assuming that ionic diffusion is rapid, material properties (activity of 3PB and 2PB sites and
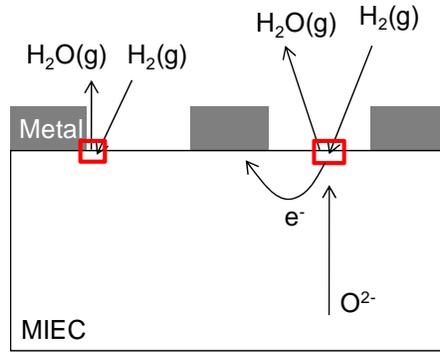
Figure 1.2: A schematic depicting electrochemical reactions (in this case, hydrogen electro-oxidation) taking place in a metal-MIEC composite electrode. Surface reaction site on the left is known as the triple-phase boundary (3PB) site where metal phase, gas phase, and ionic phase meet. Surface reaction site on the right is known as the double-phase boundary (2PB) site in which the metal is not directly involved.
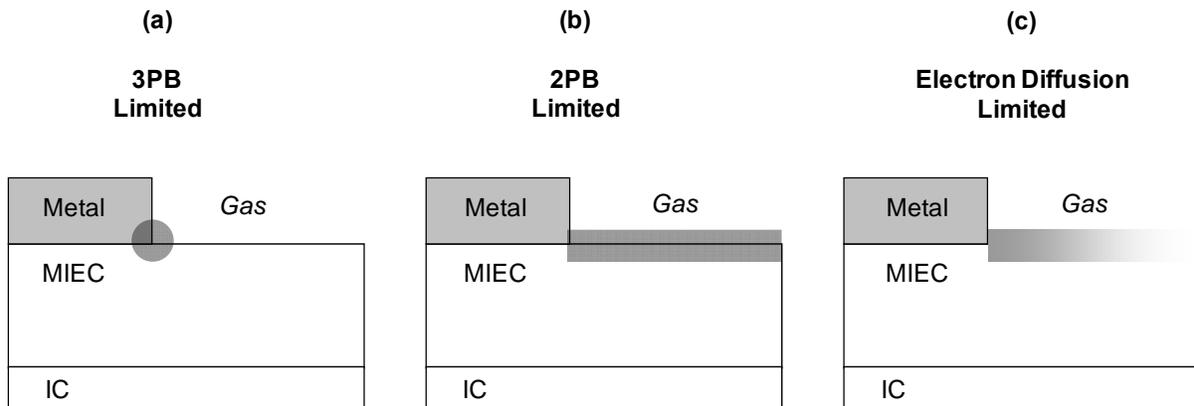
Figure 1.3: Three limiting regimes for electrochemical reactions in metal-MIEC electrodes. **(a)** Majority of the reactions are catalyzed by the metal. **(b)** Majority of the reactions are catalyzed by the MIEC without diffusion limits, and **(c)** with diffusion limits.

characteristic electron diffusion length) and microstructural parameters (reaction site densities and the distance between the site and the current collector) govern reaction rates in this model electrode structure. In the case where the 3PB site activity and/or density are high, Figure 1.3(a), reactions are localized and electron transport unimportant. However, in the case where 2PB site activity and/or density are high, Figure 1.3(b-c), electron transport becomes crucial. To a first-order approximation, the width of the active zone is determined by the ratio of the electronic conductivity to the surface activity. The surface reaction-transport coupling in MIEC near surfaces are discussed in detail in Chapters 3 and 4.

1.1.2 Application in Thermochemical Processes

More energy from sunlight strikes the earth in one hour than all of the energy consumed on the planet in one year.[28] Thus, the challenge modern society faces is not one of identifying a sustainable energy source, but rather one of capitalizing on the vast solar resource base. Despite its intermittent supply, solar electricity levels of up to about 20 % can be integrated into existing electricity delivery networks through careful management of grid resources.[29] For significantly greater penetration and an eventual complete transition away from fossil energy, however, the photon energy must be stored and made available for use when and where energy is needed.

To enable this objective, several plausible storage solutions are already being pursued in laboratories worldwide including high energy density batteries, hydrogen production via electrolysis, and hydrogen production via direct photolysis. Despite these efforts, large-scale energy storage remains elusive. In this work, the change in the valence state in ceria (or equivalently, oxygen content) in response to changes in temperature and oxygen partial pressure,

where the thermal cycling is, ideally, induced by exposure to solar radiation, is utilized for fuel production (Figure 1.4). For example, for hydrogen production from water vapor, the reaction cycle for the metal oxide MO_2, where M represents Ce and often also a dopant element, can be described as follows:

(Higher Temperature, T_H) $\quad\quad \frac{1}{\delta} MO_2 \rightarrow \frac{1}{\delta} MO_{2-\delta} + \frac{1}{2} O_2(g)$ $\quad\quad\quad\quad\quad\quad\quad\quad$ (1.3)

(Lower Temperature, T_L) $\quad H_2O(g) + \frac{1}{\delta} MO_{2-\delta} \rightarrow \frac{1}{\delta} MO_2 + H_2(g)$ $\quad\quad\quad\quad\quad$ (1.4)

Total $\quad\quad\quad\quad\quad\quad\quad H_2O(g) \rightarrow \frac{1}{2} O_2(g) + H_2(g)$ $\quad\quad\quad\quad\quad\quad\quad\quad$ (1.5)
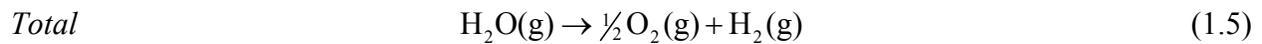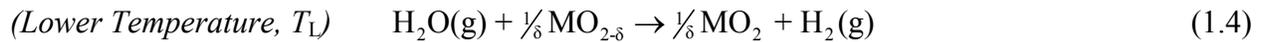
An analogous reaction cycle can be written for CO_2 reduction (though carbonaceous species and hydrocarbons need to be considered).

This thermochemical approach has its roots in reaction schemes developed in the 1970's aimed at utilizing the heat from nuclear reactors.[30-31] The early schemes typically involved corrosive gases such as H_2SO_4 and HBr and cycles with as many as 3-5 individual reaction steps. The concept of using metal oxides as substrates for the thermochemical production of hydrogen first appeared in the literature in a publication by Nakamura[32], in which cycling between Fe_3O_4 and FeO was demonstrated. The specific reactions employed were

T_H $\quad\quad\quad\quad\quad\quad\quad\quad Fe_3O_4 \rightarrow 3FeO + \frac{1}{2} O_2(g)$ $\quad\quad\quad\quad\quad\quad\quad\quad$ (1.6)

T_L $\quad\quad\quad\quad\quad\quad\quad\quad 3FeO + H_2O(g) \rightarrow Fe_3O_4 + H_2(g)$ $\quad\quad\quad\quad\quad\quad$ (1.7)
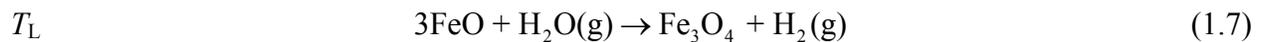
The thermochemistry of this pair of reactions is such that (under standard pressures) the first is favored at temperatures above 2,250 °C and the latter at temperatures below about 700 °C. The extremely high temperatures required for the reduction step (which exceeds the melting temperatures of both FeO and Fe_3O_4) render this specific cycle impractical, but the approach

nevertheless introduced the notion of metal oxides as a thermochemical reaction medium and a new strategy for thermochemical fuel production. To lower the temperature of the second step, substitution of Fe by more easily reduced metals has been pursued.[31,33-35] Thermodynamic analyses have shown Co, Ni and Zn to be the most promising. State-of-the-art approaches now utilize these substitutional compounds, with cycles between the wustite (MO) and spinel (M_3O_4) phases. An alternative metal oxide approach, the Zn(g)/ZnO cycle, embraces rather than avoids the volatility of the material in the reduced state.[36] Difficulties arise in this case from the need to quench the Zn from the gaseous state to prevent reoxidation and the need to utilize nanoparticle Zn in the hydrolysis step to obtain sufficient reaction kinetics.[37-38]

In the thirty years since the first report by Nakamura on the Fe_3O_4/FeO cycle, significant effort has been directed towards practical implementation of the alternatives described. It has been recognized that for the doped MO/M_3O_4 systems, stability of the particles – against sintering, vaporization, or even melting – is essential for ensuring easy access of the gaseous phase to the entirety of the material. One strategy that has emerged is the utilization of zirconia
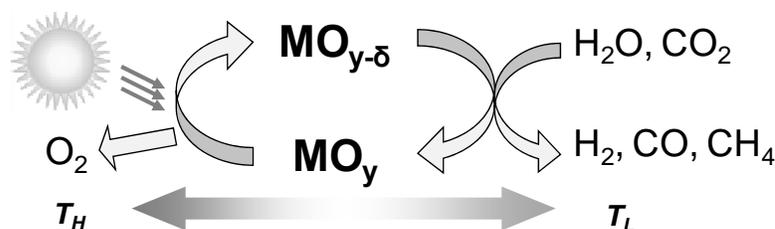
Figure 1.4: A fuel-production thermochemical cycle in which a metal-oxide is thermally reduced by heating it to T_H (ideally with concentrated solar radiation), cooled to T_L, and then reoxidized with H_2O or CO_2.

as a support that prevents high temperature coagulation of the active oxide.[39-41] While this approach improves short-term cyclability, it introduces redox-inactive material into the reaction vessel, thereby lowering efficiency and gravimetric fuel productivity, and the long-term stability of such systems is unknown. For the $Zn(g)/ZnO$ system, the challenges of delivering mass quantities of nanoparticles through reactor systems have just begun to be tackled. Thus, despite significant progress, substantial hurdles remain for the thermochemical production of hydrogen using oxides and, accordingly, additional efforts in materials development may be necessary.

Based on the lessons learned from the fully solid-state MO/M_3O_4 systems, one can surmise that for realistic implementation of solar-thermal fuel production, materials with excellent thermal stability, a high tendency towards reduction under moderate heating, and an ability to maintain open architectures, at both the crystal structure and microstructure levels, under aggressive thermal cycling are desirable. Furthermore, development of thermochemical cycles that produce not only hydrogen but fuels such as CH_4, CH_3OH, or CO (the latter as a synthesis gas component) utilizing CO_2 as an input may have greater immediate acceptability into our energy production and delivery infrastructure. In totality, these considerations suggest that ceria, which undergoes substantial oxygen stoichiometry changes without a change in crystal structure, has an extremely high melting temperature of ~ 2,500 °C, displays high catalytic activity towards carbon-containing gases[6,42-43] and resistance towards carbon deposition[26,44], is an attractive material for thermochemical fuel production. Indeed, preliminary reports of the suitability of ceria for H_2O dissociations have appeared in the recent literature.[41,45-49]

1.2 Bulk Defect Chemistry of Doped & Undoped Ceria

The extent of oxygen nonstoichiometry in ceria is governed by the equilibration of solid-state and gas phase oxygen:

$$\tfrac{1}{2}O_2(g) + \tfrac{1}{\delta}CeO_{2-\delta} \leftrightarrow \tfrac{1}{\delta}CeO_2 \tag{1.8}$$

For the purpose of discussing defect equilibria, reaction (1.8) can be rewritten for an infinitesimal change in nonstoichiometry (on a per mole atomic oxygen basis) such that the composition of the oxide remains the same on both sides of the reaction:

$$\lim_{\alpha \to 0} \tfrac{1}{2}O_2(g) + \tfrac{1}{\alpha}CeO_{2-\delta-\alpha} \leftrightarrow \tfrac{1}{\alpha}CeO_{2-\delta} \tag{1.9}$$

At equilibrium, the chemical potential of neutral lattice oxygen μ_O (which depends on the nonstoichiometry of the solid) must be equal to that of the gaseous oxygen:

$$\tfrac{1}{2}\mu_{O_2}^{eq} = \mu_O^{eq}(\delta) \tag{1.10}$$

where the superscript 'eq' denotes equilibrium. The chemical potential of the lattice oxygen is typically given relative to the standard energy of gaseous oxygen:

$$\Delta\mu_O^{eq}(\delta) = \mu_O^{eq}(\delta) - \tfrac{1}{2}\mu_{O_2}^0 = k_B T \ln \frac{p_{O_2}}{p_{O_2}^0} \tag{1.11}$$

where $\mu_{O_2}^0$ is the chemical potential of oxygen at the standard pressure $p_{O_2}^0$.

So far, the defect chemistry of ceria has not been explicitly taken into account. It has been widely established that the main defects in ceria are oxygen vacancies and small polarons localized on the Ce sites.[1,50-52] When the electrons migrate through the ionic solid, it polarizes the lattice which results in a potential well that traps the charge.[53] A polaron is a quasi-particle

consisting of the electron and the polarization field. Written in Kröger-Vink notation, the defect reaction is

$$\tfrac{1}{2}O_2(g) + 2Ce'_{Ce} + V_O^{\bullet\bullet} \leftrightarrow 2Ce_{Ce}^{\times} + O_O^{\times} \tag{1.12}$$
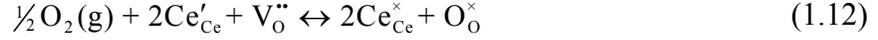
where the species Ce'_{Ce} is equivalent to a small polaron. As ceria is a large bandgap semiconductor, electron-hole pair creation is negligible at the interested temperatures. Doping with tetravalent rare-earth oxides (*e.g.* samaria, yttria, and gadolinia) leads to the formation of extrinsic oxygen vacancies[11]:

$$M_2O_3 + 2Ce_{Ce}^{\times} + O_O^{\times} \leftrightarrow 2Sm'_{Ce} + V_O^{\bullet\bullet} + 2CeO_2 \tag{1.13}$$
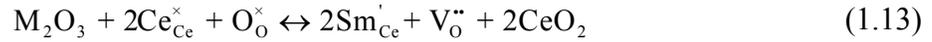
In doped ceria with oxygen nonstoichiometry δ up 0.03 to 0.04, treatment of all defects as randomly-located and non-interacting in the dilute solution limit using reaction (1.12) yields excellent agreement between computed and experimental nonstoichiometry data.[50,54-56] In undoped ceria, dilute solution approximation breaks down when δ is greater than 0.01, with non-idealities typically attributed to the formation of intrinsic $Ce'_{Ce}V_O^{\bullet\bullet}Ce'_{Ce}$ defect complexes, with the effects generally being more pronounced at higher δ and lower temperatures.[1,57-58] As the majority of this work concerns samaria doped ceria with nonstoichiometry values less than 0.05, reaction (1.12) is taken to be the sole defect reaction and all defect species assumed to behave ideally.

At equilibrium, the sum of the chemical potentials of all species must be zero locally ($\sum_j v_j \mu_j(x) = 0$, where v_j is the stoichiometric coefficient). Thus, the following is true at any given position in the solid at equilibrium:

$$\tfrac{1}{2}\mu_{O_2}^{eq}(x) = \mu_O^{eq}(x) = -\mu_{ion}^{eq}(x) - 2\mu_{eon}^{eq}(x) \tag{1.14}$$

where the subscripts 'O$_2$', 'ion', and 'eon' denote gaseous oxygen, oxygen vacancies, and localized electrons, respectively. In the absence of a chemical or electrochemical gradient, potentials are uniform within the material. The chemical potential of a crystallographic defect is written as

$$\mu_i = \mu_i^0 + k_B T \ln \frac{c_i}{c_i^0 - c_i} \tag{1.15}$$

where μ_i^0 is the standard chemical potential, c_i is the defect concentration, c_i^0 is the standard state for solid state defects, taken to correspond to all available crystallographic sites, k_B is Boltzmann's constant, and T is temperature. In the case of a gaseous species (*e.g.* oxygen), concentrations are replaced with partial pressures. In the absence of a chemical or electrochemical gradient, electroneutrality is further obeyed in the bulk:

$$\sum_i z_i c_i^{eq} = -c_{eon}^{eq} + 2c_{ion}^{eq} - c_{dop}^{eq} = 0 \tag{1.16}$$

where the subscript 'dop' denotes dopant. Now, considering the defect model (*i.e.* reaction (1.12)), combining Eq. (1.14) and (1.15) gives:

$$\frac{\frac{1}{2}\mu_{O_2}^0 + \mu_{ion}^0 + \mu_{eon}^0}{T} = -k_B \left(\ln \frac{p_{O_2}}{p_{O_2}^0} + \ln \frac{c_{ion}^{eq}}{c_{ion}^0 - c_{ion}^{eq}} + 2\ln \frac{c_{eon}^{eq}}{c_{eon}^0 - c_{eon}^{eq}} \right) \tag{1.17}$$

where the right-hand side gives the total configurational entropy and the numerator on the left-hand side gives the sum of the standard enthalpy and the standard entropy (*i.e.* non-configurational contributions). Rearranging the above equation yields the familiar law of mass action, corresponding to reaction (1.12):

$$K_{oxd} = \exp\left(-\frac{\Delta G_O^0}{k_B T}\right) = \frac{\left(1 - c_{ion}^{eq}/c_{ion}^{0,eq}\right)\left(1 - c_{eon}^{eq}/c_{eon}^{0,eq}\right)^2}{\left(p_{O_2}^{*eq}\right)^{1/2}\left(c_{ion}^{eq}/c_{ion}^{0,eq}\right)\left(c_{eon}^{eq}/c_{eon}^{0,eq}\right)^2} \approx \frac{\left(p_{O_2}^{*eq}\right)^{-1/2}}{c_{ion}^{*eq}\left(c_{eon}^{*eq}\right)^2} \tag{1.18}$$

where K_{oxd} is the equilibrium constant for ceria oxidation, ΔG_{red}^0 is the standard Gibbs free energy of oxidation, $p_{O_2}^*$ is the activity of gaseous oxygen (taken to be the ratio of the partial pressure of oxygen to the standard state of 1 atm), and c_i^* is the fraction of crystallographic sites occupied by defects. In this work, the defect fractions are much less than unity, allowing the denominator to be approximated as 1.

In an undoped system, the electroneutrality condition is $c_{eon}^{eq} = 2c_{ion}^{eq}$. It follows from Eq. (1.18) that:

$$c_{eon}^{*eq} = \exp\left(\frac{\Delta G_O^0}{3k_B T}\right)\left(p_{O_2}^{*eq}\right)^{-1/6} \tag{1.19}$$

For a heavily-doped system, one can make an additional approximation that the dopant concentration is much larger than the polaron concentration ($2c_{ion}^{eq} - c_{dop}^{eq} \approx 0$) under moderately reducing conditions, yielding:

$$c_{eon}^{*eq} \approx \sqrt{\frac{2}{\left(c_{dop}^{*eq}\right)}}\exp\left(\frac{\Delta G_O^0}{2k_B T}\right)\left(p_{O_2}^{*eq}\right)^{-1/4} \tag{1.20}$$

This expression gives the well-observed $p_{O_2}^{-1/4}$ dependence of the electron concentration.[2,50,54-56,59]

Lastly, the gas phase reaction and equilibrium condition can be written as:

$$H_2(g) + \frac{1}{2}O_2(g) \rightarrow H_2O(g) \tag{1.21}$$

$$K_W = \exp\left(-\frac{\Delta G_g^0}{k_B T}\right) = \frac{p_{H_2O}^{*eq}}{p_{H_2}^{*eq}\left(p_{O_2}^{*eq}\right)^{\frac{1}{2}}} \tag{1.22}$$

where K_W is the equilibrium constant. Eq.(1.16), (1.18) and (1.22), in combination with the reported values of the thermodynamic parameters for reactions (1.12) and (1.21) ($\Delta G_{red}^0(T)$ and $\Delta G_g^0(T)$, respectively) enables computation of the equilibrium concentration of the charge carrier species under a given temperature and oxygen partial pressure, within the limits of ideal solution behavior.

1.3 Transport in Mixed Conductors

Equations described the migration of charged and neutral species in MIECs are reviewed. In Chapter 3, 4, and 5, transport models based on these equations are developed for electrochemical and chemical systems to elucidate bulk and surface phenomena.

1.3.1 Diffusion-Drift of Charge Carriers

The driving force for charge carrier migration is the electrochemical potential $\tilde{\mu}_i$, given as:

$$\tilde{\mu}_i = \mu_i + ez_i\phi \tag{1.23}$$

where μ_i and z_i are the chemical potential and charge of species i, respectively, e is the electron charge, and ϕ is the electric potential. Charge transport of oxygen vacancies and electrons can be described by the generalized transport equation:

$$\mathbf{j}_i^{chg} = -\frac{(ez_i)^2 D_i c_i}{k_B T} \nabla \tilde{\mu}_i^* \tag{1.24}$$

where D_i is the diffusion coefficient and $\tilde{\mu}_i^* = \tilde{\mu}_i / ez_i$ is the reduced electrochemical potential. Cross-terms are neglected. Utilizing the Nernst-Einstein relation and the conductivity equation ($\sigma_i = ez_i c_i \bar{\mu}_i$, where $\bar{\mu}_i$ is the mobility)

$$D_i = \frac{(k_B T) \bar{\mu}_i}{ez_i} = \frac{k_B T \sigma_i}{(ez_i)^2 c_i} \tag{1.25}$$

and substituting the definition of electrochemical potential, Eq. (1.23) can be rewritten as

$$\mathbf{j}_i^{chg} = -\frac{ez_i D_i c_i}{k_B T} \nabla \mu - \sigma_i \nabla \phi \tag{1.26}$$

where the first term is attributed to diffusion and the second attributed to drift.

Ionic transport in ceria occurs by thermally-activated hopping, with the mobility given as

$$\bar{\mu}_{ion} = \frac{\bar{\mu}_{ion}^0}{T} \exp\left(-\frac{\Delta H_{ion}}{k_B T}\right) \tag{1.27}$$

where $\bar{\mu}_{ion}^0$ is a constant and ΔH_{ion} is the migration enthalpy. On the other hand, electron transport in ceria, as evident by its low mobility ($\sim 10^{-3}$ cm^2 V^{-1} s^{-1} at 650 °C),[2] occurs via small polaron hopping.[52] In ceria, the polaron is localized on the cerium site and migrates from site to site via thermally-activated hopping. In the case of adiabatic hopping, polaron mobility takes the same form as Eq. (1.27).

Using the carrier concentration expression derived in Eq. (1.19) and assuming that carrier mobilities are concentration-independent, the total conductivity in undoped ceria (under the

dilute limit assumption) is given as

$$\sigma_{tot} = \left(\sigma_{ion}^0 + \sigma_{eon}^0\right)\left(p_{O_2}^*\right)^{-\frac{1}{6}}$$ (1.28)

where σ_i^0 is the p_{O_2}-independent conductivity. In heavily-doped systems, oxygen vacancy concentration is pinned by the dopant concentration and Eq. (1.20) gives the total conductivity

$$\sigma_{tot} = \sigma_{ion} + \sigma_{eon}^0\left(p_{O_2}^*\right)^{-\frac{1}{4}}$$ (1.29)

where the first and second terms are the oxygen vacancy and polaron conductivities, respectively.

Several additional equations govern transport. Under the assumption that there is no internal source or sink of species in the material under study, species conservation during transport implies that

$$ez_i\frac{\partial c_i}{\partial t} + \nabla\cdot\mathbf{j}_i^{chg} = 0$$ (1.30)

In the steady state case ($\frac{\partial c_i}{\partial t} = 0$), combining (1.24) and (1.30), and assuming that the diffusion coefficients and temperature are uniform (generally valid for small bias perturbations), yields

$$\nabla\cdot\left(c_i\nabla\tilde{\mu}_i^*\right) = 0$$ (1.31)

Finally, the carrier concentrations are coupled to the electrical potential via the Poisson equation:

$$\nabla^2\phi = -\frac{e}{\varepsilon}\sum_i z_i c_i$$ (1.32)

where ε is the permittivity of the material.

1.3.2 Ambipolar Diffusion of Neutral Oxygen

The presence of both oxygen vacancies and polarons in ceria implies that neutral oxygen can migrate within the solid via coupled diffusion of both defects. In the absence of an externally applied electric field or current, the total charge fluxes must be conserved. The ambipolar diffusion of neutral oxygen, denoted by the subscript 'O', is governed by Fick's first law and the continuity equation:

$$\mathbf{j}_O(x,t) = -\tilde{D}_O(x,t)\nabla c_O(x,t) \tag{1.33}$$

$$\frac{\partial c_O(x,t)}{\partial t} = -\nabla J_O(x,t) \tag{1.34}$$

with the effective diffusion coefficient, $\tilde{D}_O$, given as[60]

$$\tilde{D}_O = -\frac{1}{4k_BT}\left(\frac{4D_{ion}D_{eon}c_{ion}c_{eon}}{4D_{ion}c_{ion}+D_{eon}c_{eon}}\right)\frac{\partial \mu_O}{\partial c_O} \tag{1.35}$$

where the partial derivative term in the ambipolar diffusion coefficient can be determined from the defect model.

Chapter 2
Experimental Methods

2.1 Synthesis & Fabrication

2.1.1 Fabrication of Bulk-Processed Electrochemical Cells

Results presented in Chapter 3.

Commercial $Sm_{0.15}Ce_{0.85}O_{1.925}$ nanoparticles (SDC15, Nextech Materials, where the suffix indicates Sm doping level) nanoparticles were precalcined at 950 °C for 5 h in air to ensure the desired sintering characteristics and then uniaxially pressed at 280 MPa for 2 min. The resulting disk pellets were sintered at 1,350 °C in air for 5 h to obtain a density of > 95 % theoretical, with final dimensions of 0.6 to 0.8 mm in thickness and 13 mm in diameter. The discs were polished using SiC sandpapers to 600 grit roughness in order to remove impurities and dopant that may have segregated during high-temperature sintering. Subsequent sonication removed lose particles from sanding. Electrodes were applied by brush-painting commercial pastes, either Englehard 6082 Pt or Electro Science 8884-G Au, to completely cover the opposing sides of the pellets. After drying, the samples were then fired at 950 °C for 120 min under stagnant air. The electrode layers so prepared had thicknesses of ~ 20 µm and grain sizes of ~ 2-10 µm. Silver mesh current collectors, measuring approximately 2 × 2 mm, were attached using silver adhesive paste (Alfa Aesar 44075). A schematic of the electrochemical cell is shown in Figure 2.1(a).

(a)   **(b)**   **(c)**
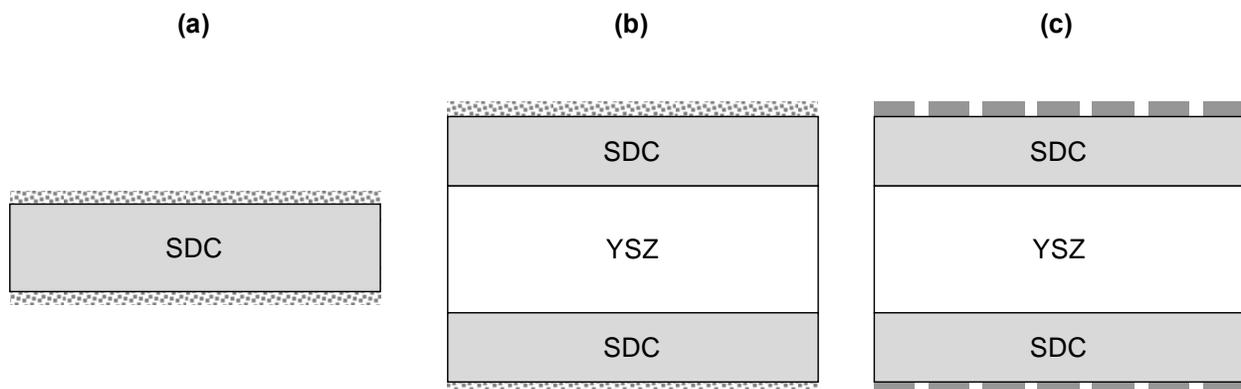
Figure 2.1: Schematic depiction of electrochemical cells examined. **(a)** samaria-doped ceria (SDC) symmetric cell with porous current collector on both sides. **(b)** SDC thin-film deposited on both sides of a ion-conducting, electron-insulating substrate (yttria-stabilized zirconia, YSZ), with porous current collector on both sides. **(c)** same as (b) except the current collector is metal thin film patterns prepared via lithography. Not drawn to scale.

2.1.2 Fabrication of Thin Film Electrochemical Cells

Results presented in Chapter 4.

Thin films of SDC15 and SDC20 with thicknesses ranging from 195 to 2241 nm were deposited onto both sides of 10×10 mm $Y_{0.16}Zr_{0.84}O_{1.92}$ (YSZ, MTI Corp.) (100), (110) and (111) oriented single crystal substrates via pulsed-laser deposition (PLD, Nocera, with Coherent 102 KrF 248 nm excimer laser, ~ 2 J cm^{-2}, 20 Hz). The PLD targets were compacted from commercial SDC powder (Fuel Cell Materials) at pressures of 190 to 380 MPa and sintered at 1,250 or 1,350 °C for 5 h in a tube dedicated to the processing of ceria and covered in excess ceria powder to avoid contamination. Double-sided deposition was achieved using sacrificial layers, also YSZ, placed between the substrate and the heater stage. The substrate temperature, as determined by a thermocouple in direct contact with the YSZ wafer (bonded with Pt adhesive

paste), was ~ 650 °C for all depositions. Average heating rates ranged between 3 and 7 °C min^{-1}. The deposition atmosphere was pure oxygen, with pressures ranging from 5 to 20 mTorr. All samples were annealed in oxygen (100 Torr) for 60 or 120 min after deposition of the second side was completed.

Current collectors were fabricated on both sides of the electrochemical cell either by metal ink painting or by metal liftoff lithography. Painted current collectors were prepared according to the procedures described in Section 2.1.1 and are shown schematically in Figure 2.1(b). Collectors produced via metal liftoff lithography were prepared using microfabrication routes. First, positive photoresist (Shipley 1813) was spin-coated onto YSZ substrates (already with the thin films deposited) at 2,000 to 3,000 rpm, and baked at 115 °C for 150 s. To obtain a photoresist layer suitable for depositing thicker current collectors, multiple spin-coating cycles were sometimes employed. Next, a glass mask plate metalized by chromium and with defined metal patterns was aligned with the samples in a contact aligner (Karl Suss MJB 3) and exposed to UV-light for 45 s. The photoresist, with portions cross-linked by exposure to radiation, were developed by immersing the samples in MF-319 developer for ~ 20 s. The above procedure was repeated for the other side of the substrate.

After drying, the samples were cleaned using an oxygen plasma to remove residual organics and then transferred to a custom DC magnetron sputtering system (AJA International) where Pt (99.99 % purity) or Ni (99.999 % purity) were deposited atop the photoresist layer on both sides. Ar pressure during film growth was 3 mTorr. Growth rates were typically 8.5 and 10.0 nm min^{-1} for Pt and Ni respectively. Deposited current collectors were typically 150 to 200 nm thick for Pt and 300 – 400 nm thick for Ni. Metal liftoff was performed by immersing the samples in acetone at room-temperature and gently rubbing with a cotton-ball swab. Prior to

electrochemical characterizations, the completed electrochemical cells were cleaned by rinsing and soaking in acetone, isopropanol, deionized water and methanol, and dried by ultra-high-purity compressed helium.

2.1.3 Fabrication of Porous Ceria Samples

Results presented in Chapter 5.

CeO_2 (Alfa Aesar 11328) or $Sm_{0.15}Ce_{0.85}O_{1.925}$ (Nextech) was ball milled with 30 wt.% starch in ethanol, uniaxially pressed into a pellet, and sintered either at 1,400 or 1,500 °C for 24 h. To examine the effect of metal cocatalysts on SDC15, Ni and Rh particles were dispersed onto SDC15. 2 wt% Rh-SDC15 and 10 wt% Ni-SDC15 were prepared via wetness impregnation by dissolving metal nitrates. After calcining at 750 °C, the powder was sintered at 1,350 °C for 24 h and pressed into a pellet. SDC15 without the addition of metal catalyst was also prepared identically as the metal-SDC15 composites and used for mechanistic comparisons.

2.2 Characterization

2.2.1 Chemical, Microstructural and Structural Analysis

X-ray diffraction (XRD) was used to determine the crystal structure, phase purity, and orientation distributions for bulk and thin film samples. Philips X'Pert Pro MPD diffractometer (Cu Kα source, 45 kV, 40 mA), was employed for polycrystalline samples and Philips X'Pert Pro MRD Pro diffractometer (Cu Kα source, 45 kV, 40 mA, 4-crystal Ge(220)/(440)

monochromator), equipped with a four-circle goniometer, was employed for thin film samples. Lattice constants were determined by Rietveld refinement using the Philips X'Pert Plus software.

Electron imaging and qualitative chemical analysis were performed on Carl Zeiss LEO 1550VP field emission scanning electron microscope (FE-SEM) equipped with Oxford INCA Energy 300 energy dispersive spectrometer (EDS). Samples were typically coated with carbon or with gold to prevent charging. JOEL JXA-8200 electron probe microanalyzer (EPMA) was used for quantitative chemical analysis. $CePO_4$ and $SmPO_4$ were used standards for the EPMA. For high-resolution imaging and local chemical analysis, FEI Tecnai F20 and F30 transmission electron microscopes (TEM), equipped with EDAX EDS, were used. Two sample surfaces were glued together, thinned, dimpled, and milled with Ar ions. FEI dual beam Nova 600 focused-ion beam was then used to prepare a cross-section sample. Pt or W was used to protect the sample during milling. High resolution EDS was performed in the scanning TEM (STEM) mode.

Surface topography imaging was obtained using an Agilent 4500 Series PicoSPM atomic force microscope (AFM).

2.2.2 Electrochemical Impedance Spectroscopy

Results presented in Chapter 3 & 4.

Electrochemical impedance spectroscopy is a powerful tool for probing serial and parallel processes that exhibit different relaxation times. For a general introduction to impedance spectroscopy, see references 61-62. Transport measurements were made by electrochemical impedance spectroscopy under controlled temperatures and atmospheres in a custom characterization system. The electrochemical cells were placed inside a continuous-flow tube

(17 mm in diameter for quartz tubes and 20 mm for alumina tubes) to which gases were delivered via digital mass flow controllers. A four-wire setup was employed to minimize inductance effects from the wiring. Dry, oxidizing conditions were obtained by delivering mixtures of pure O_2 and Ar (> 99.9995 % purity) directly to the sample, whereas humidification was achieved by flowing the dry gas through a bubbler placed inside a variable-temperature water bath. Effluent humidity was monitored using a Rotronic Hygroflex capacitative sensor. Reducing conditions were obtained by delivering mixtures of pure H_2 and Ar (> 99.9995 % purity), with some of gas passed through a bubbler. The total flow rate was kept constant at 101 cm^3 min^{-1} (standard temperature and pressure, STP). Impedance measurements were made using a Solartron 1260A frequency response analyzer at a zero-bias with perturbation amplitude of 20 to 50 mV.

2.2.3 Gas-Solid Catalytic Reactions

Results presented in Chapter 5.

Two types of reactor systems were utilized to characterize heterogeneous (gas-solid) reactions, one based on a rapid-heating infrared furnace and the other based on an electric furnace. In the infrared furnace system (Ulvac-Riko VHT-E44), porous ceria pellets (0.25 to 0.50 g in weight, 7 mm in diameter, and 2 to 4 mm in thickness) were loaded into a horizontal alumina tube reactor (9.5 mm in diameter). A thermocouple, enclosed in an alumina sheath, was placed in direct contact with the sample and used to control the furnace. Digital mass flow controllers delivered a variety of gases to the reactor. Humidification of inlet gases was achieved by passing dry gas through a bubbler inside a temperature-controlled oven. Effluent humidity

was measured using a Rotronic Hygroflex 2 sensor and dried, effluent gas composition determined using a Pfeiffer Thermostar GSD301 quadrupole mass spectrometer. Quantification of the mass spectrometry data (H_2 and O_2) was achieved by performing daily, six-point calibration curves for all gas species at the concentrations of interests. To reduce ceria, the porous samples were heated to until it becomes partially reduced (1,500 to 1,600 °C) under 10^{-5} atm O_2. To oxidize ceria, the thermally-reduced samples were exposed to weakly oxidizing gases (H_2O or CO_2) at 800 °C.

In the electric-furnace-based system, samples containing 1 g of material (porous pellets lightly crushed and sieved to obtain particle sizes between 150 and 500 μm) were loaded into a continuous flow packed bed reactor (10 mm in diameter) with the particles held in place by a porous quartz frit. Reaction gases were delivered by digital mass flow controllers, and the effluent gas characterized by a Varian CP-4900 gas chromatograph (GC) equipped with PoraPak Q and Molecular Sieve 5A columns. H_2, CH_4, CO and CO_2 concentrations were converted to flow rates using an internal N_2 standard, which also served as a diluent. In some cases, Ar was also used as a diluent. GC calibration curves were established using analytical grade premixed gases. The reduction of ceria was achieved by flowing a mixture of H_2, H_2O, and Ar at either $p_{O_2} = 2.0 \times 10^{-21}$ atm at 800 °C or 3.8×10^{-18} atm at 900 °C (oxygen partial pressures were calculated by assuming gas phase equilibrium and verified using an oxygen sensor). Humidification was achieved by passing the reaction gas through a H_2O bubbler inside a temperature-controlled bath. The oxidation of ceria was achieved by passing diluted water vapor and/or CO_2 over the packed bed of ceria particles. The temperature excursion upon oxidation of the ceria in no case exceeded 6 °C.

Temperature-programmed oxidation (TPO) experiments were also performed to characterize solid products that may have formed during reaction. Using the electric-furnace-based system described above, samples were heated from room temperature to 800 °C under 0.21 atm O_2 (balance N_2) while monitoring CO and CO_2 levels using the GC.

2.2.4 Solar Reactor

Results presented in Chapter 5.

To examine solar fuel production via thermochemical cycling, a solar reactor was constructed, Figure 2.2. Designed as a cavity-receiver that allows the efficient capture of incoming concentrated solar radiation, the reactor consists of a cylindrical volume 102 mm in both inner diameter and height, with a 4 cm-diameter circular aperture. A highly-reflective compound parabolic concentrator (CPC)[63] is incorporated at the aperture to augment the solar flux concentration and reduce re-radiation losses. The cavity is closed by a 3 mm-thick clear fused quartz window mounted in front of the CPC on a water-cooled copper ring that also serves as a shield for spilled radiation. The cavity walls are made from Inconel 600 and are lined with thermally-insulating porous alumina tiles of 2.5 cm thickness. Reacting gases were injected through four inlets into the annular gap between the porous ceria cylinder and the alumina insulation tiles. Product gases exited the cavity through an axial outlet port at the bottom. Experiments were conducted at Paul Scherrer Institute's High-Flux Solar Simulator (HFSS)[64]: an array of ten 15 kW_e high-pressure xenon arcs, each closed-coupled with truncated ellipsoidal specular reflectors of common focus. This facility provides an external source of intense thermal radiation, mostly in the visible and infrared spectra, that closely approximates the heat transfer
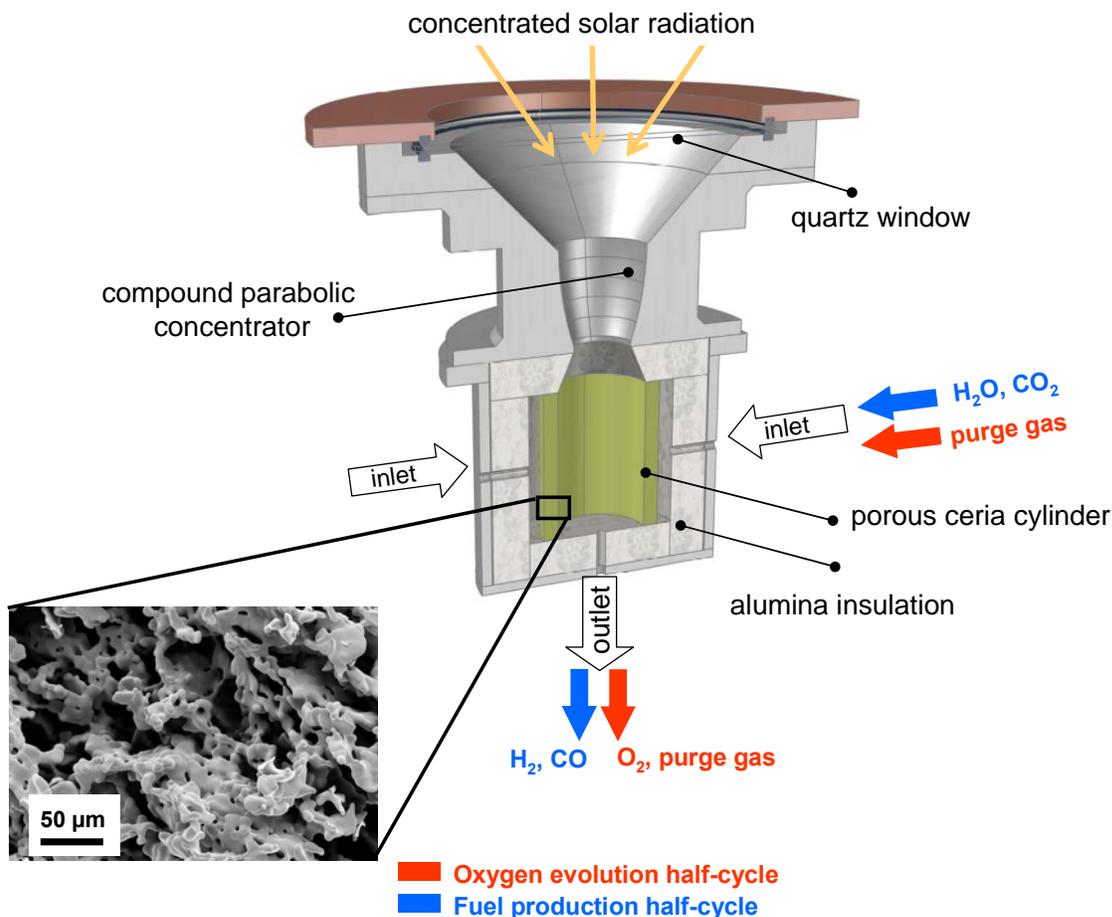
Figure 2.2: Schematic of the solar reactor configuration (aperture and window not shown). Inset shows the scanning electron micrograph of the porous ceria tube after 23 cycles.

characteristics of highly concentrating solar systems such as solar towers and solar parabolic dishes. Power flux intensities were adjustable by the number of Xe arcs in operation, the position of the venetian-blind shutter, and the position of the solar reactor relative to the focal plane. Radiative fluxes incident into the solar reactor were measured optically with a calibrated CCD camera on a water-cooled Al_2O_3-plasma-coated Lambertian target, positioned at the aperture plane. Incident radiative power was obtained by numerical integration of the measured fluxes

and verified by a calorimeter. Gaseous products were analyzed on-line by gas chromatography (Agilent High Speed Micro G2890A, detection limit: 10 ppm, sampling rate: 0.01 Hz), supplemented by infrared-based detectors for CO and CO_2 (Siemens Ultramat-23, detection threshold: 0.2 %, sampling rate 1 Hz), and by thermal conductivity-based detectors for H_2 and O_2 (Siemens Calomat 6 and Oxymat 6, detection threshold: 50 ppm, sampling rate: 1 Hz).

Chapter 3
Electrochemistry of Bulk-Processed Ceria

3.1 Summary

In this section, experimental data and numerical modeling results are combined to elucidate the surface electrochemistry of M | SDC15 | M model electrodes, where M is a porous metal, and SDC15 is fabricated using bulk ceramics methods. Surface and bulk properties of this MIEC system were examined at temperatures between 575 and 650 °C in a H_2-H_2O environment over a wide range of gas composition, as both surface and bulk properties of this MIEC system depend strongly on gas activities. The contribution of the metallic phase (M) to surface electrochemistry is further elucidated by comparing the reaction rates over Pt and Au on SDC15. Finally, experimental results are analyzed using a two-dimensional numerical transport model which calculates the potential and current distributions in ceria near reactive surfaces.

Experimental results confirm that the rate-limiting step in hydrogen electro-oxidation and hydrolysis near open-circuit conditions depends on oxygen partial pressure (rather than on hydrogen or water vapor pressure independently, as found in typical electrode materials) and, furthermore, does not change with the metal type, suggesting that the ceria | gas surface (2PB), rather than the ceria | gas | metal interface (3PB), is the active site. Numerical calculations indicate that the rate-limiting step is approximately two orders of magnitude faster than the electron drift-diffusion between the active site and the metal current collector and is, therefore, likely to be either surface reaction at the ceria surface or transport through the surface oxygen vacancy depletion layer.

3.2 Cell Configuration & Materials Characterization

Unlike those commonly employed in literature, the M | SDC15 | M cell configuration used here does not employ a pure ionic conductor support. Growing interest in the SOFC community to use MIECs with high ionic conductivity and acceptable levels of electronic conductivity (*e.g.* doped ceria) both as electrolytes and as components in metal-MIEC composite electrodes motivates the use of this configuration.

Powder x-ray diffraction confirmed that the sintered SDC15 pellets are single phase with a cubic fluorite structure ($a = $ 5.430 Å). From cross-sectional SEM images (not shown), the average grain size was estimated, using the mean-intercept method, to be 0.36 µm. By

(a)   (b)
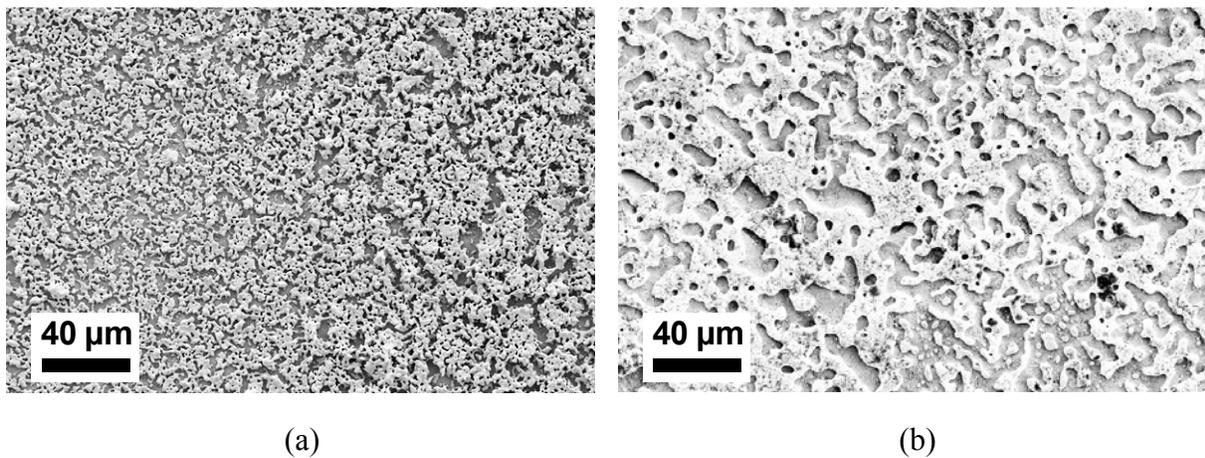
Figure 3.1: Scanning electron micrographs of **(a)** porous Pt and **(b)** porous Au current collectors on SDC15. Light and dark regions correspond to the metal and oxide phases, respectively.

Table 3.1: Experimentally-determined microstructural parameters for the M | SDC15 | M electrochemical cells. $2W_1$ is the average metal feature width and $2W_2$ is the average pore width.

Current Collector Metal	W_1 (µm)	W_2 (µm)
Pt	1.5	2.5
Au	6.0	3.2
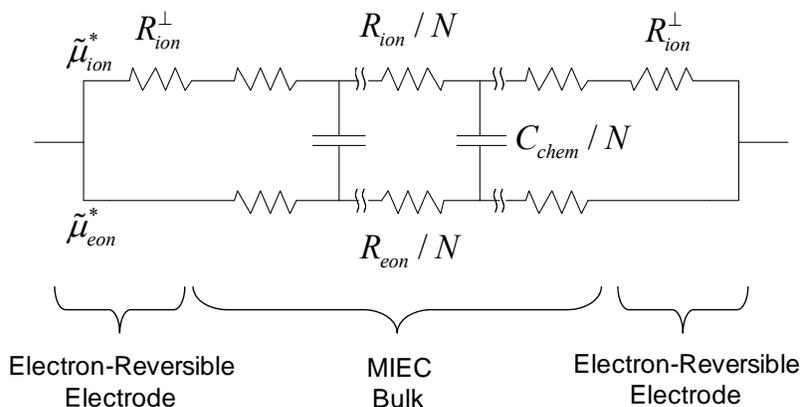
Figure 3.2: Physically-derived equivalent circuit for a MIEC symmetric cell with electron-reversible metal electrodes. The driving force on the top and bottom current rails are the electrochemical potentials of ions and electrons, respectively. N is the total number of differential elements.

performing image analysis on surface SEM images (Figure 2.1), the average metal feature width ($2W_1$) and average pore size ($2W_2$) were determined (Table 3.1). Generally speaking, the Pt electrodes consist of multiple layers of interconnected particles, whereas the Au electrodes consist of one layer of particles.

3.3 One-dimensional Impedance Model

The bulk and surface impedance model of a MIEC has recently been derived from physical equations[65-66] and has been demonstrated to rigorously apply to doped ceria with metal electrodes used in this section[2] (see Figure 2.1 for the schematic of electrochemical cells and Figure 3.2 for the equivalent circuit used for the analysis). In contrast to the case of a pure ionic

conductor (also with simple metal electrodes), the interfacial response of a MIEC appears in the Nyquist representation (Z_{real} vs. $-Z_{imag}$) as an asymmetric, tear-drop shaped arc, rather than a depressed, symmetric semi-circle. Specifically, under the conditions of large macroscopic sample dimensions relative to the Debye length, local electroneutrality, electron reversible electrodes, and negligible interfacial capacitance relative to the chemical capacitance (defined below), the impedance, Z, expressed as a function of angular frequency, ω, is

$$Z(\omega) = R_\infty + (R_0 - R_\infty) \frac{\tanh \sqrt{\frac{i\omega L^2}{4\tilde{D}}} + \frac{R_{ion} + R_{eon}}{2R_{ion}^\perp} \tanh \sqrt{\frac{i\omega L^2}{4\tilde{D}}}}{\sqrt{\frac{i\omega L^2}{4\tilde{D}}} + \frac{R_{ion} + R_{eon}}{2R_{ion}^\perp} \tanh \sqrt{\frac{i\omega L^2}{4\tilde{D}}}} \tag{3.1}$$

where

$$\tilde{D} = \frac{L^2}{(R_{ion} + R_{eon})C_{chem}} \tag{3.2}$$

$$C_{chem} = \frac{e^2}{k_B T} AL \left(\frac{1}{4c_{ion}} + \frac{1}{c_{eon}} \right)^{-1} \tag{3.3}$$

$$R_\infty = \left(\frac{1}{R_{eon}} + \frac{1}{R_{ion}} \right)^{-1} \tag{3.4}$$

$$R_0 = \left(\frac{1}{R_{ion} + 2R_{ion}^\perp} + \frac{1}{R_{eon}} \right)^{-1} \tag{3.5}$$

$$R_{ion} = \frac{1}{\sigma_{ion}} \frac{L}{A} \tag{3.6}$$

$$R_{eon} = \frac{1}{\sigma_{eon}} \frac{L}{A} \tag{3.7}$$

and where R_{ion} and R_{eon} are the bulk ionic and electronic resistances, respectively, $\tilde{D}$ is the chemical diffusion coefficient, C_{chem} is the chemical capacitance, $R_{ion}^\perp$ is the electrode resistance,

L is the sample length, and A is the sample cross-sectional area. The terms R_∞ and R_0 correspond to the high and low frequency intercepts of the asymmetric electrode arc and reflect, respectively, the total bulk resistance and the total system resistance. Bulk and grain boundary impedance arcs were experimentally inaccessible due to the high characteristic frequencies and therefore not explicitly included in the model.

Electrolyte and electrode parameters were obtained for M | SDC15 | M electrochemical cells under H_2-H_2O-Ar environment by fitting to Eq. (3.1) using ZView (Scribner Associates). At sufficiently oxidizing conditions (*i.e.* O_2-Ar atmospheres), the electronic conductivity of SDC15 becomes negligible (Eq. (1.29)), and the electrolyte can be treated as a pure ionic conductor. Accordingly, impedance data collected at p_{O_2} = 0.21 atm were analyzed using a simple $R_{ion}(R_{ion}^\perp Q)$ equivalent circuit, where Q is a constant phase element. The ionic resistance, determined from this fitting, was taken to be constant over the range of oxygen partial pressures examined. With this value at hand, the fit parameters for the spectra collected under reducing conditions were R_{eon}, $R_{ion}^\perp$ and c_{eon}.

3.4 Bulk Parameters

Under all experimental conditions, excellent agreement was achieved between the fit and the experimental data, confirming the validity of the model (Figure 3.3). Impedance spectra collected under identical conditions at the beginning and end of the experiment showed negligible change (Figure 3.4), indicating that bulk and electrode properties of the electrochemical cell were stable over the course of the experiment. Before analyzing surface electrochemistry, the impedance model is first validated by comparing the fitted bulk transport
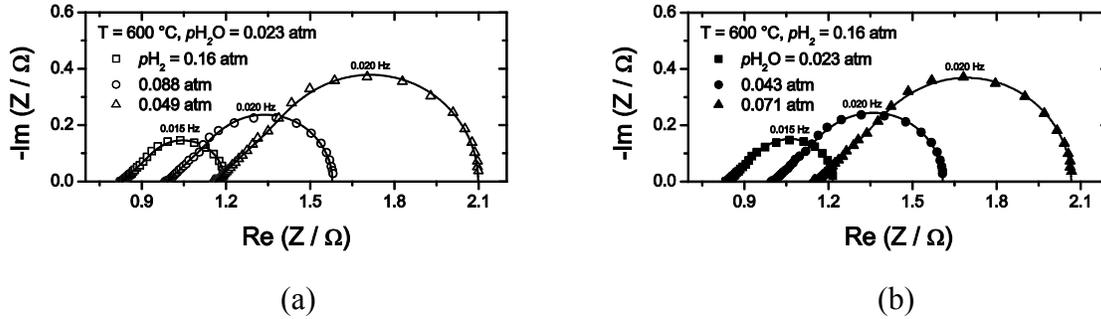
Figure 3.3: Impedance spectra of Pt | SDC15 | Pt **(a)** collected under several p_{H_2} at a fixed p_{H_2O} (as indicated), and **(b)** collected under several p_{H_2O} at a fixed p_{H_2}. The p_{H_2} and p_{H_2O} values were selected so they give the same equilibrium oxygen partial pressure for the corresponding measurements in (a) and (b). Solid lines indicate fit.
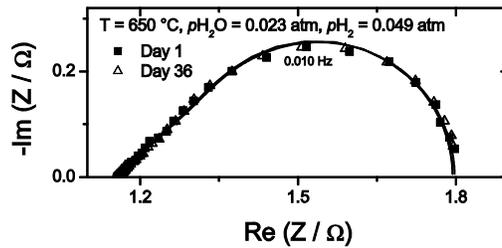
Figure 3.4: Impedance spectra measured under identical conditions at the beginning of the experiment and at the end of the experiment. Solid lines indicate fit. Degradation was negligible over the course of the experiment.

properties to known literature values.

Under humidified hydrogen atmospheres (575 to 650 °C), the high frequency intercept, R_0, in the Nyquist plot is taken to be the sum of the grain boundary and bulk resistances, with contributions from ionic and electronic transport (protonic transport is negligible in ceria). Because of the higher activation energy associated with the effective grain boundary conductivity relative to bulk conductivity, the high temperatures employed in this work, and the low grain boundary density due to large grain size (0.3 µm), the grain boundary contributions to
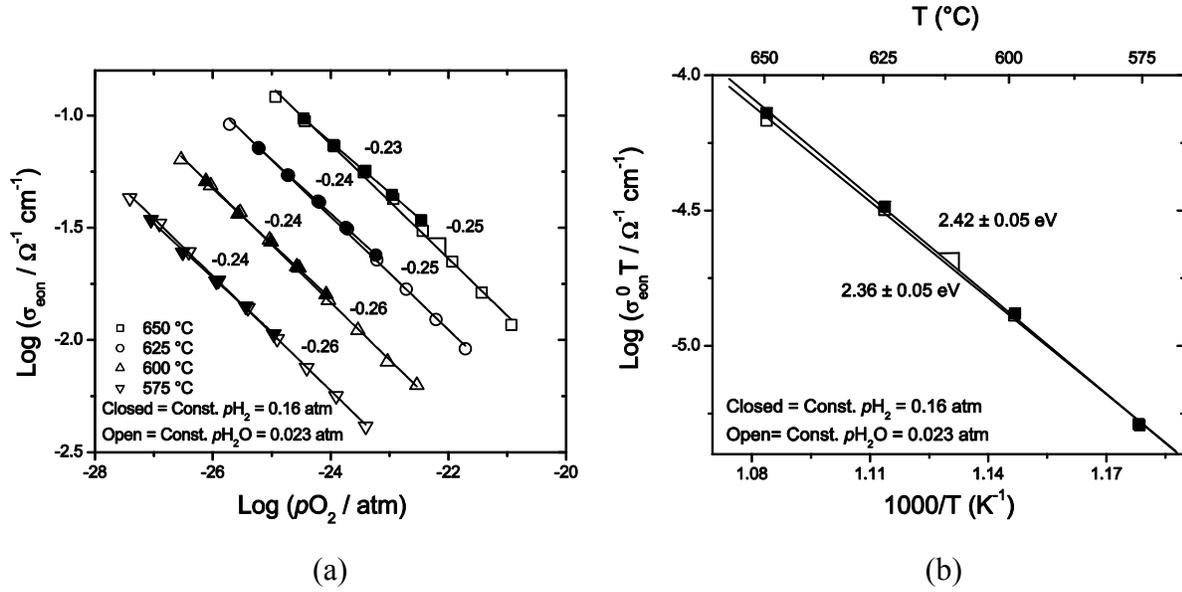
Figure 3.5: SDC15 bulk properties obtained from fitting the physical impedance model (see text) to raw impedance data. Open and closed data points indicate measurements made under a constant p_{H_2O} and constant p_{H_2}, respectively. **(a)** Electronic conductivity. **(b)** p_{O_2}-independent electronic conductivity (σ_{eon}^0 in $\sigma_{eon} = \sigma_{eon}^0 p_{O_2}^{-1/4}$) determined from each conductivity isotherm in (a) and plotted in the Arrhenius form.

R_0 is relatively small. By extrapolating the low-temperature bulk and grain boundary ionic conductivities to higher temperatures, the bulk resistance is estimated to be ~ 4 times greater than the grain boundary resistance at 575 °C. Accordingly, R_0 is approximated as the bulk resistance and grain boundary contribution ignored.

As already discussed, the electronic conductivity of SDC15, σ_{eon}, is determined from R_0 using the independently measured ionic conductivity obtained under oxidizing conditions (Figure 3.5). Fitting σ_{eon} to a power-law expression, $\sigma_{eon} = \sigma_{eon}^0 p_{O_2}^n$, yields exponent values ranging from -0.23 to -0.26. These values agree closely with the expected value of $-1/4$ for heavily-doped ceria. Furthermore, fitting the data to the power-law expression with $n = -1/4$ (*i.e.* Eq. (1.29))
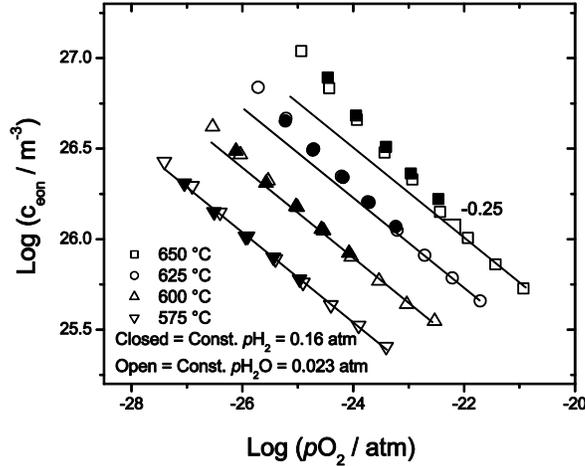
Figure 3.6: Electron carrier concentrations calculated from the chemical capacitance (solid lines are guides for the eye – deviation from the expected oxygen partial pressure is attributed to non-ideal solution behavior).

yields an activation energy of 2.4 eV (with contributions from polaron formation and migration enthalpy), which agrees well with previously reported values.[2,12-13]

The remaining bulk parameter obtained through the impedance spectra fitting is the electronic carrier concentration. Assuming dilute solution behavior and that the electron concentration is much smaller than the oxygen vacancy concentration $(c_{ion} = \frac{1}{2}[Sm'_{Ce}] \times 8/a^3 = 4 \times 10^{27}$ m^{-3}, where a is the room-temperature lattice constant), chemical capacitance directly yields the electron concentration (Figure 3.6). Like conductivity, the electron concentration is expected to scale with $p_{O_2}^{-1/4}$. With the exception of several data points in which the dilute solution assumption is not satisfied, the theoretically expected dependence of c_{eon} on oxygen partial pressure is assumeds.

3.5 Effect of Gas Activity on Surface Reaction Pathways

The activities of gaseous species influences the concentrations of surface species, such as adsorbed hydroxyl, oxygen, etc., and therefore play a significant role in the surface electrochemistry of ceria. Additionally, the bulk and surface electronic properties of ceria, namely the defect concentrations and the Fermi level, depend on the oxygen activity. As a first step for exploring the reaction pathways in M | SDC15 | M, the interfacial resistance was examined as a function of hydrogen and water vapor pressure independently.

The electrode resistance was measured at various hydrogen and water vapor pressures and temperatures (Figure 3.7). For a water vapor pressure held constant at 0.023 atm, the p_{H_2} reaction order, *i.e.* n in $\left(\tilde{R}_{ion}^{\perp} \right)^{-1} = k^0 p_{H_2}^n$, (where $\tilde{R}_{ion}^{\perp}$ is the electrode resistance normalized by the macroscopic electrode area) was found to be 0.49, 0.44, 0.41, and 0.41 at 650, 625, 600, and 575 °C, respectively. At these same temperatures, and for a hydrogen partial pressure held constant at 0.16 atm, the p_{H_2O} reaction order was found to be -0.45, -0.41, and -0.38, -0.39, respectively. The somewhat unexpected observation that the reaction orders of p_{H_2} and p_{H_2O} almost differ only in sign implies that the electrode resistance scales with p_{O_2}, which, in turn, scales with $p_{H_2}^{-2} p_{H_2O}^2$, Eq. (1.22) (Figure 3.8(a)). Indeed, similar to the bulk electronic conductivity, the electrode resistance does not scale with p_{H_2} or p_{H_2O} independently but, rather, attains the same value as long as the oxygen partial pressure is not changed. Given this result, the following empirical rate law is proposed to describe the electrode reaction rate (or more specifically, inverse area-normalized electrode resistance) near equilibrium conditions:

$$\left(\tilde{R}_{ion}^{\perp} \right)^{-1} = a k^0 p_{O_2}^{-\frac{1}{4}} = a \left(k^0 K_W^{\frac{1}{2}} \right) p_{H_2}^{\frac{1}{2}} p_{H_2O}^{-\frac{1}{2}} \tag{3.8}$$
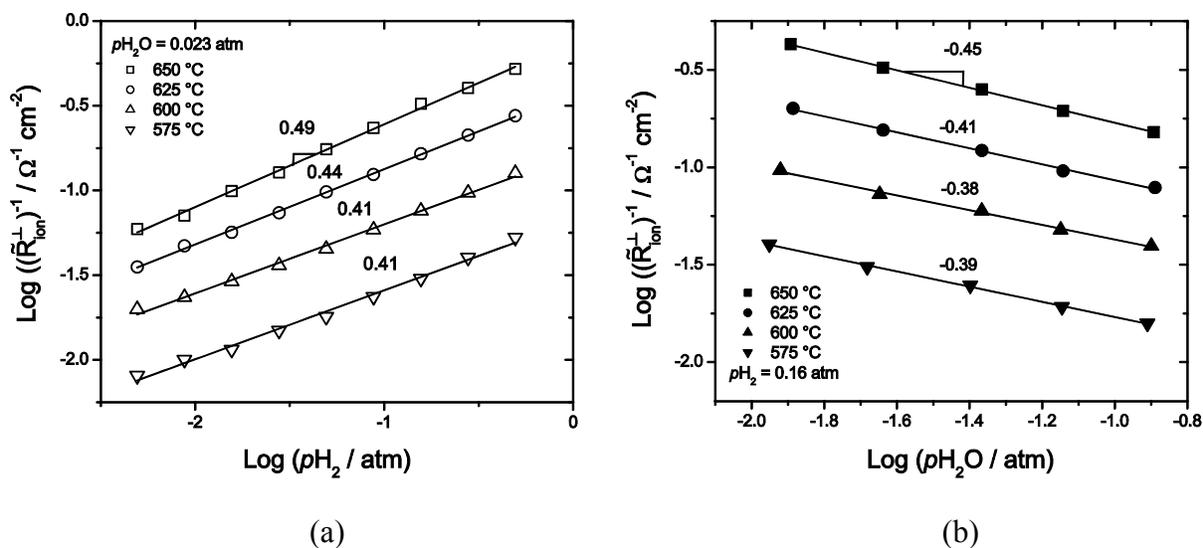
Figure 3.7: Inverse Pt | SDC15 electrode resistance normalized by the macroscopic electrode area as a function of **(a)** p_{H_2} and **(b)** p_{H_2O}. Slope gives the reaction order.
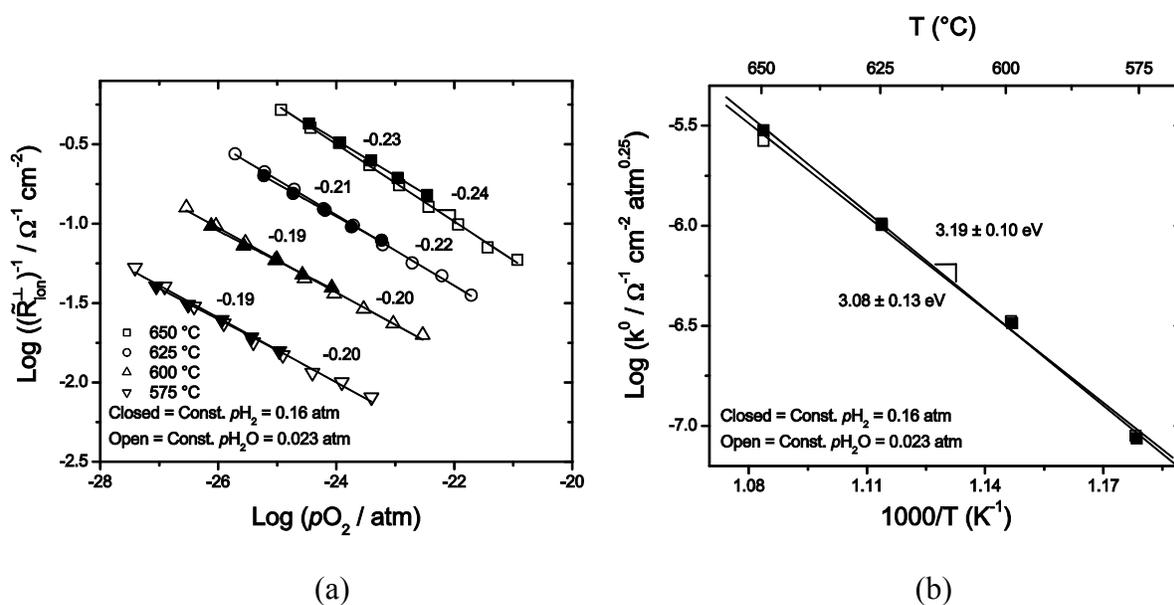
Figure 3.8: **(a)** Inverse Pt | SDC15 electrode resistance plotted a function of equilibrium p_{O_2}. **(b)** Temperature dependence of the electrode reaction rate-constant, obtained using the empirical rate law in Eq. (3.8). Open and closed data points indicate measurements made under a constant p_{H_2O} and constant p_{H_2}, respectively.

where a is an area-normalization constant (which can be determined only if the nature of the rate-limiting step is known), k^0 is the p_{O_2}-independent rate-constant, K_W is the equilibrium constant for gas-phase hydrogen oxidation, and the reaction order is obtained by averaging the eight values shown in Figure 3.8(a) and rounding to the nearest reasonable fraction. Fitting the electrode resistance isotherms at various temperatures to Eq. (3.8) yields the activation energy (Figure 3.8(b)). Values of 3.19 ± 0.10 eV and 3.08 ± 0.13 eV were identical, to within error, for measurements performed under constant p_{H_2} and constant p_{H_2O}, respectively, further supporting the above rate law. The observation that the rate-limiting step depends on oxygen partial pressure rather than on hydrogen and water vapor pressure independently will be discussed in tandem with other experimental and numerical results.

3.6 Effect of Metallic Phase on Surface Electrochemistry

In the M | SDC15 | M system, both the 2PB and the 3PB reaction pathways proceed in parallel. In order to examine the relative rates of these two competing pathways, the interfacial resistances of M = Pt and Au on SDC15 are compared. Unlike Pt, micrometer scale Au is catalytically inactive,[67] and therefore, such pairing of materials is ideal for evaluating the relative contributions of the two parallel pathways.

In principle, changing the metal type should not impact the bulk properties of SDC15. As a verification, the bulk properties were compared between the Pt and Au systems. The bulk electronic conductivity and the electron concentration scale with $p_{O_2}^{-1/4}$ for both electrode systems. Furthermore, as summarized in Table 3.2, the activation energies for electronic and ionic conductivities are essentially the same between the Pt and Au systems. Overall, the bulk

Table 3.2: Summary of activation energies for various processes for SDC15 with Au and Pt current collectors.

Symbol	Process	Pt | SDC15 | Pt (eV) This Work	Au | SDC15 | Au (eV) This Work	Pt | SDC15 | Pt (eV)[2]
$-\frac{1}{2}\,\Delta H_{oxd} + \Delta H_{eon}$	Electronic Conduction	2.41	2.68	2.31
$-\frac{1}{2}\,\Delta H_{oxd}$	Creation of Electronic Charge Carriers	2.09	2.22	2.09
ΔH_{eon}	Electron Migration	0.32	0.46	0.22
ΔH_{ion}	Ion Migration	0.70	0.69	0.67

(a)

(b)
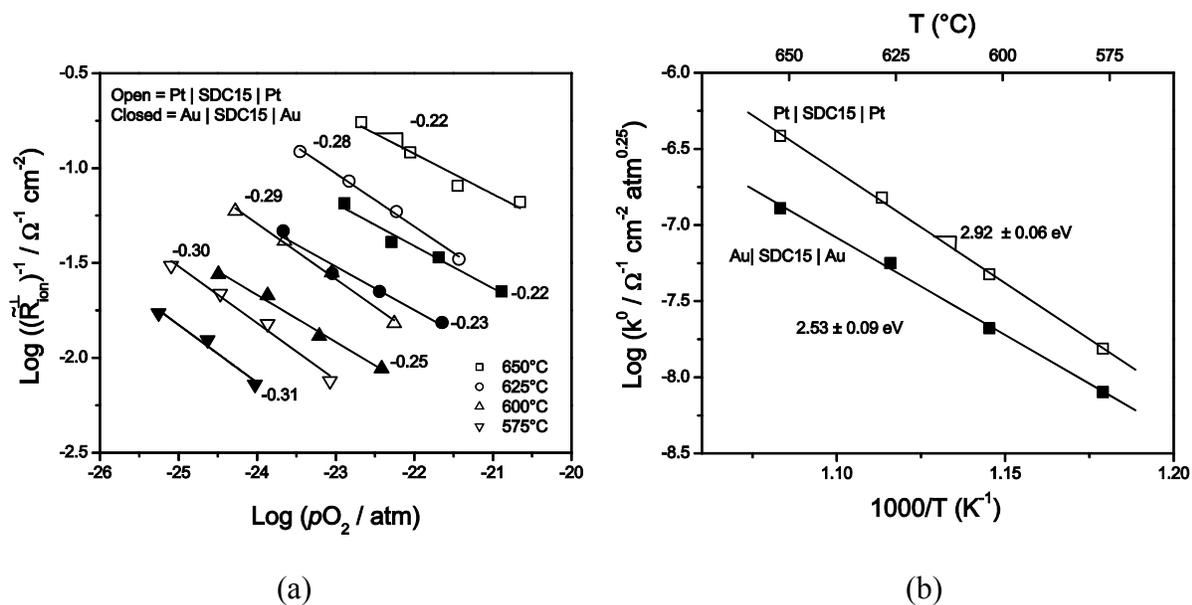
Figure 3.9: (a) The dependence of the inverse of the area-specific interfacial resistance on p_{O_2} at various temperatures for Pt \| SDC \| Pt (open) and Au \| SDC \| Au (closed). **(b)** The temperature dependence of the rate-constant.

transport properties of SDC15 are not metal-dependent, and the parameters agree with those documented in the literature.[2,12-13]

The inverse of area-specific electrode resistance, $\left(\tilde{R}_{ion}^{\perp} \right)^{-1}$ is presented in Figure 3.9(a) as a function of oxygen partial pressure. Consistent with the rate law obtained in the previous section (Eq. (3.8)), $\left(\tilde{R}_{ion}^{\perp} \right)^{-1}$ displays an approximate $p_{O_2}^{-1/4}$ dependence for both Pt and Au systems. Moreover, the oxygen partial pressure independent rate-constant, k^0, obtained from fitting to the rate law (Eq. (3.8), displays Arrhenius behavior in both cases, with similar activation energies of 2.92 eV for Pt and 2.53 eV for Au (Figure 3.9(b)). The observation that the choice of metal has little impact on the oxygen partial pressure and temperature dependence of the interfacial resistance in metal│ceria electrode, in turn, indicates that ceria, rather than the metal (or the metal│ceria interface), is the predominant electrochemically active component. However, from the data presented in Figure 3.9(b), it is also apparent that the interfacial resistance of the Au electrodes is about a factor of ~ 3 greater than that of the Pt electrodes. This discrepancy is attributed to differences between the electrode microstructures, which dictates the surface area of ceria exposed as well as the distance electrons migrate from the reaction site to the metal current collector. Normalization of the electrode resistance requires details of the rate-limiting step that is yet to be established (*i.e.* a surface- or a diffusion-limited reaction). A more detailed analysis using a two-dimensional transport model will be presented in the next section.

3.7 Two-Dimensional Investigation of Electrochemical Potential & Current Distributions near Surfaces

As reported in the earlier sections of this Chapter, experimental results have confirmed that (1) the rate-limiting step exhibits an explicit oxygen partial pressure dependence, and (2) the electrode reaction mechanism is unaffected by the choice of metal in the M | SDC15 | M system. Furthermore, the electrode oxygen partial pressure and temperature dependence are in reasonable agreement to those for electron conduction and formation. Specifically, the measured activation energies for the electrode reaction (2.5 – 3.2 eV) are comparable to those for bulk electronic conductivity (~ 2.5 eV) as well the enthalpy for electron formation (~ 2.1 eV). These results suggest that reactions takes place on the ceria | gas 2PB sites preferentially, and electron concentrations and/or electronic conduction near the surface could play a dominant role in the reaction pathway. As described in Section 1.1.1, for reactions to occur on the 2PB sites, electrons must be transported to and from the metal current collector. The one-dimensional impedance model used earlier in this Chapter does not treat surface reaction-diffusion coupling resulting from in-plane electron migration, as depicted in Figure 1.2. The aim of this section is to determine the relative roles of reaction rates and electron transport rates in the near-surface region of ceria using two-dimensional, numerical methods.

There have been extensive modeling efforts focusing on surface reaction-transport interactions in MIECs.[2,65-66,68-86] Many of the modeling efforts employ porous medium theory and effective transport parameters to reduce the system from three to one dimension.[70-72,81-82,86] While such one-dimensional models are inherently unable to treat local potential and flux distributions at small length scales, they are directly applicable to certain geometries or materials systems (*e.g.* thin film and thin-column electrodes with homogeneous properties) and hence have

been useful under appropriate conditions for decoupling surface reaction and bulk diffusion kinetics.[65-66,73,87] Beyond these effective medium models, a handful of two-dimensional current-voltage and impedance models have been developed to quantify the behavior of a wider range of electrode structures, with the majority of them focused on SOFC cathode materials in which the electronic conductivity greatly exceeds that of the ions.[76,78-80,83-85] In addition, the aforementioned one- and two-dimensional MIEC electrode models involve a pure ionic conductor support, in which the electron current is confined within the electrode. Growing interests in the SOFC community to use MIECs with acceptable levels of electronic conductivity both as electrolytes and as components in metal-MIEC composite electrodes, motivate the development of a generalized model to investigate transport of ionic and electronic carriers in the bulk and near interfaces.

3.7.1 Physical Model

As an approximation of the electrochemical cells used in the experiment, the physical model, depicted in Figure 3.10(a), consists of a MIEC conductor (doped ceria) with patterned metal current collectors on both sides, placed in a uniform gas environment. The patterned metal current collectors permit the system to be described, Figure 3.10(b), by repeating domains using mirror symmetry lines (Γ_2 and Γ_3). The thickness of the cell is fixed at $2l = 1$ mm. Mirror symmetry along Γ_1 implies the computational domain can be further limited to one-half this total thickness. The current collector dimensions, the width of the MIEC | metal interface (Γ_4 boundary), $2W_1$, and the width of the MIEC | gas interface (Γ_5 boundary), $2W_2$, are, unless stated otherwise, fixed at values of 3 and 5 μm, respectively. These dimensions are selected to

(a)

Interconnected
Metal Patterns

(b)
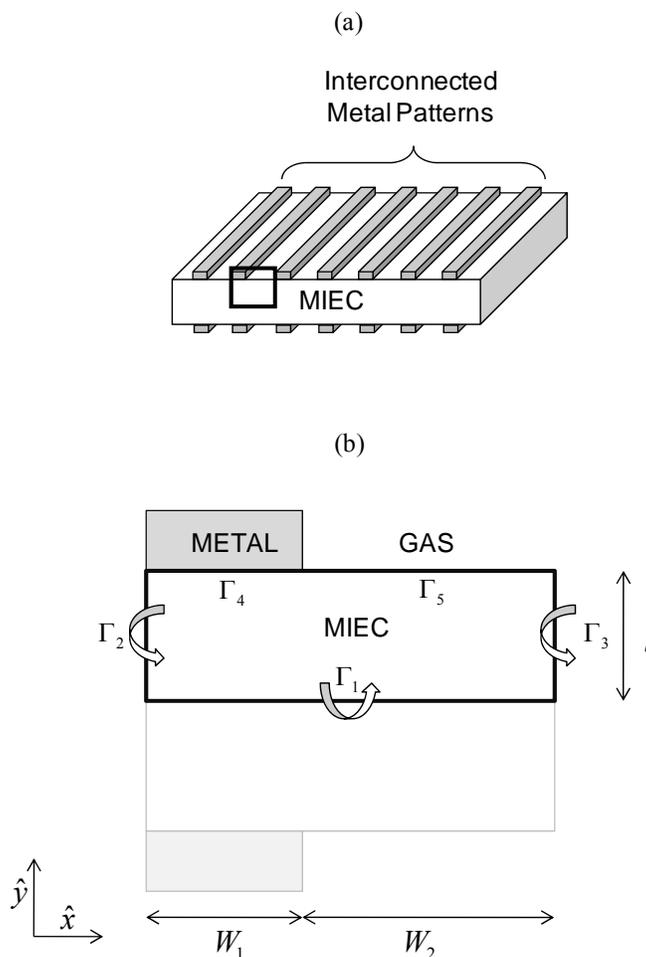
Figure 3.10: (a) Schematic of the electrochemical cell modeled: a symmetric cell with patterned metal current collectors on both sides of a MIEC placed in a uniform gas atmosphere. **(b)** The modeling domain with the boundaries shown: Γ_1, Γ_2, and Γ_3 are symmetry lines, Γ_4 is the MIEC | metal interface, and Γ_5 is the MIEC | gas interface. $2W_1$ is the width of the metal current collector stripe, $2W_2$ is distance between each current collector stripe , and $2l$ is the thickness of the sample. Not drawn to scale.

approximate the Pt | SDC15 | Pt cell examined in Section 3.4 through 3.6. A different set of

dimensions representing Au | SDC15 | Au will also be used in Section 3.7.2.4 (Table 3.1).

Consistent with the experimental data earlier this Chapter, the contribution of the 3PBs

(with effective reaction widths of no more than several nanometers) to the overall

electrochemical reaction can, to a first approximation, be neglected. This assumptions implies that reactions occur exclusively on the ceria | gas 2PB. The analysis is further simplified by taking the MIEC | metal and MIEC | gas interfaces to be reversible to electrons, by ignoring interfacial space-charge effects and charge double-layers, and by treating the electrochemical reaction, Eq. (1.2), in terms of a single, global step, without consideration of detailed mechanisms. The use of a global reaction constant is an operational definition and does not impact the analysis of interest here. The inevitable modification of the electric potential at interfaces can be considered, to a first approximation, to be reflected in the value of the global reaction rate and need not be directly modeled. Finally, electrochemical impedance spectroscopy results (a single arc is observed rather than two arcs, Figure 3.3) suggest that electron transfer across the metal | doped ceria interfaces is extremely rapid relative to the formation or breaking of chemical bonds, justifying an assumption of electron reversibility for the present analysis.[2,88] In combination, this set of simplifications allows examination of the two steps of interest in the electrochemical reaction pathway: the surface reaction, and the electron diffusion-drift from the active site to the metal current collector.

A general presentation of the two-dimensional (non-steady-state) transport model developed to address the geometry of Figure 3.10 has been presented elsewhere.[74] The model, described in full here, adopts the following sequence of steps. First, the carrier concentrations are solved analytically under equilibrium conditions (Section 1.2). Next, transport induced by a small-bias perturbation is described using Nernst-Planck and Poisson equations (Section 3.7.1.1). Subsequently, appropriate boundary conditions describing heterogeneous and homogeneous interfaces are applied (Section 3.7.1.2). Finally, carrier concentration, flux, and electric potential are solved numerically using an adaptive finite-element method (Section 3.7.1.3).

3.7.1.1 Small-Bias Transport

Bulk transport occurs in response to the application of a small bias away from equilibrium. Experimentally, this is achieved by subjecting the electrochemical cell to a small voltage relative to the unbiased system. Upon perturbation of the system with a small voltage, the properties $\{q_k\} = \{\tilde{\mu}_i^*, c_i, \phi\}$ each adopt a value described as

$$q_k = q_k^{eq} + q_k^{(1)} \tag{3.9}$$

where q_k^{eq} is the equilibrium value and $q_k^{(1)}$ is the small perturbation in q_k (such that $\left|q_k^{(1)}\right| \ll \left|q_k^{eq}\right|$)

It follows from the assumption that the equilibrium concentration and electrical potential are uniform within the system that

$$\nabla q_k^{eq} = \nabla^2 q_k^{eq} = 0 \tag{3.10}$$

Substituting the above definitions and properties above into Eq. (1.31), and ignoring second and higher order terms, yields the following equation

$$\nabla^2 \tilde{\mu}_i^{*(1)} = 0 \tag{3.11}$$

Expanding the chemical and electric potential (Eq. (1.23) and (1.15)) about their equilibrium values and ignoring higher order terms gives the following approximation for the reduced electrochemical potential under perturbation:

$$\tilde{\mu}_i^{*(1)} = \frac{k_B T}{e z_i} \frac{c_i^{(1)}}{c_i^{eq}} + \phi^{(1)} \tag{3.12}$$

Substituting Eq. (3.12) into (3.11), in turn, yields

$$\frac{1}{z_i} \nabla^2 c_i^{*(1)} + \nabla^2 \phi^{*(1)} = 0 \tag{3.13}$$

where the dimensionless carrier concentration and electric potential under perturbation are defined as

$$c_i^{*(1)} = \frac{c_i^{(1)}}{c_i^{eq}} \tag{3.14}$$

$$\phi^{*(1)} = \phi^{(1)} \left(\frac{k_B T}{e} \right)^{-1} \tag{3.15}$$

The perturbed reduced electrochemical potential can also be written in terms of the dimensionless quantities defined above:

$$\tilde{\mu}_i^{*(1)} = \frac{k_B T}{e} \left[\frac{c_i^{*(1)}}{z_i} + \phi^{*(1)} \right] \tag{3.16}$$

Eq. (3.13), together with the Poisson equation (Eq. (1.32)), represents a system of coupled nonlinear differential equations. The evaluation is simplified by making use of the electroneutrality condition (Eq. (1.16)) which links the equilibrium ionic and electronic carrier concentrations. A small perturbation in the concentration of one carrier must be accompanied by a change in the concentration for the other carrier. For the specific case of doped ceria system, this relationship is:

$$2c_{ion}^{(1)} \approx c_{eon}^{(1)} \tag{3.17}$$

Writing Eq. (3.13) for both ionic and electronic charge carriers and applying the above approximation gives:

$$\nabla^2 c_{eon}^{*(1)} = 0 \tag{3.18}$$

$$\nabla^2 \phi^{*(1)} = 0 \tag{3.19}$$

Under a small perturbation, carrier concentration and electrical potential obey the partial

differential equations Eq. (3.18) and (3.19). With the application of appropriate boundary conditions, the carrier concentration profile and electrical potential distribution can be computed. In turn, these results give the electrochemical potential distribution and the charge flux. In principle, a non-uniform carrier concentration profile implies spatially varying conductivities. However, because the perturbation is small, this effect is sufficiently small that it can be ignored. Specifically, for a typical voltage perturbation of 50 mV the impact on electron concentration is less than a factor of two, whereas the vacancy concentration remains fixed by the dopant concentration.

3.7.1.2 *Boundary Conditions*

As shown in Figure 3.10(b), the boundary conditions along a total of five boundaries must be specified. As already noted, although the behavior of charge carriers near boundaries is complex in the real system as a result of the formation of charge double-layers, for the purposes of evaluating the relative roles of electronic transport and electrochemical reaction rates, a detailed description of these phenomena is not required. Accordingly, such effects are ignored here.

By symmetry arguments, electric potential and carrier concentration do not vary along the mirror symmetry line Γ_1 and current flows only along the direction perpendicular to the boundary. In addition, the assumption of linearity upon small bias implies that the magnitude of the perturbation can be set arbitrarily on Γ_1 and Γ_4 (see Appendix A). It is further assumed that the MIEC | metal interface (Γ_4) is blocking to the ionic species:

$$\left. \frac{\partial \tilde{\mu}_{ion}^{*(1)}}{\partial y} \right|_{\Gamma_4} = 0 \tag{3.20}$$

Evaluating this derivative (*i.e.* differentiating Eq. (3.16)) for the ionic species, and applying the electroneutrality condition (justified by the assumption that electron transfer is facile across the interface), gives, with some rearrangement

$$\left.\frac{\partial c_{eon}^{*(1)}}{\partial y}\right|_{\Gamma_4} = -4\frac{c_{ion}^{eq}}{c_{eon}^{eq}}\left.\frac{\partial \phi^{*(1)}}{\partial y}\right|_{\Gamma_4} \tag{3.21}$$

Turning to the Γ_2 and Γ_3 boundaries, it follows from symmetry that there is no change in electrochemical potentials for both ions and electrons (and therefore no change in $c_{eon}^{*(1)}$ or $\phi^{*(1)}$) across the boundaries between each repeating domain.

The next boundary of interest is that at the MIEC | gas interface (Γ_5). It is assumed that, as in the bulk, the interfacial reaction behaves linearly upon a small bias. The reaction rate, or equivalently, the current flux, is thus taken to be proportional to the step-change in the electrochemical potential across the interface. For the case of oxygen vacancy (ion) transfer:

$$\mathbf{j}_{ion}^{chg}\cdot\hat{\mathbf{y}}\Big|_{\Gamma_5} = -k\left(\left.\tilde{\mu}_{ion}^{*(1)}\right|_{\Gamma_{5+}} - \left.\tilde{\mu}_{ion}^{*(1)}\right|_{\Gamma_5}\right) \tag{3.22}$$

with

$$k = \tilde{R}_{rxn}^{*-1} \tag{3.23}$$

where k is the surface reaction rate-constant and $\tilde{R}_{rxn}^*$ is the reaction resistance normalized by the active surface area W_2, Γ_{5+} denotes the exposed surface of the MIEC, Γ_5 denotes the MIEC immediately beneath the surface, and $\hat{y}$ is a unit vector in the direction perpendicular to the interface. This is essentially the Chang-Jaffe boundary condition.[89] The electrochemical potential of the ionic species on the exposed surface Γ_{5+} can be evaluated as follows. By the requirement

of local equilibrium (Eq. (1.14)), the following is true everywhere in the MIEC and on the Γ_5 surface:

$$\frac{1}{4e}\mu_{O_2} + \tilde{\mu}_{ion}^* - \tilde{\mu}_{eon}^* = 0 \tag{3.24}$$

where μ_{O_2} is the chemical potential of gaseous oxygen and it is assumed there is no gas-phase concentration gradient near the MIEC | gas interface. For a small perturbation this is readily achieved by maintaining a sufficiently high gas flow rate. Under a small bias Eq. (3.24), specifically on the exposed surface of the oxide, becomes:

$$\tilde{\mu}_{ion}^{*(1)}\Big|_{\Gamma_{5+}} - \tilde{\mu}_{eon}^{*(1)}\Big|_{\Gamma_{5+}} = 0 \tag{3.25}$$

The assumption of reversibility of the electron transfer reaction implies

$$\tilde{\mu}_{eon}^{*(1)}\Big|_{\Gamma_{5+}} - \tilde{\mu}_{eon}^{*(1)}\Big|_{\Gamma_5} = 0 \tag{3.26}$$

Substituting Eqs. (3.25) and (3.26) into Eq.(3.22), the chemical reaction rate can be rewritten as:

$$\mathbf{j}_{ion}^{chg} \cdot \hat{\mathbf{y}}\Big|_{\Gamma_5} = -k\left(\tilde{\mu}_{eon}^{*(1)}\Big|_{\Gamma_5} - \tilde{\mu}_{ion}^{*(1)}\Big|_{\Gamma_5}\right) \tag{3.27}$$

Substituting the expression for $\tilde{\mu}_i^{*(1)}$ of Eq. (3.16) into Eq. (3.27), the ion flux across the interface is given as:

$$\mathbf{j}_{ion}^{chg} \cdot \hat{\mathbf{y}}\Big|_{\Gamma_5} = \frac{k_B T}{e} k\left(c_{eon}^{*(1)} + \frac{c_{ion}^{*(1)}}{2}\right)\Bigg|_{\Gamma_5} \tag{3.28}$$

This expression can be further reduced by inserting the electroneutrality approximation:

$$\mathbf{j}_{ion}^{chg} \cdot \hat{\mathbf{y}}\Big|_{\Gamma_5} = \frac{k_B T}{e} k c_{eon}^{*(1)}\left(1 + \frac{c_{eon}^{eq}}{4c_{ion}^{eq}}\right)\Bigg|_{\Gamma_5} \tag{3.29}$$

To complete the boundary condition expression, it is recognized that the current is conserved across the MIEC | gas interface. That is, the flux of species i leaving the MIEC | gas interface as a result of diffusion-drift as given by Eq. (1.24), must equal the flux of that species injected as a result of the electrochemical reaction at the interface:

$$-\frac{\left(ez_i\right)^2 D_i c_i}{k_B T}\frac{\partial \tilde{\mu}_i^{*(1)}}{\partial y}\bigg|_{\Gamma_5} = \mathbf{j}_i^{chg}\cdot\hat{\mathbf{y}}\big|_{\Gamma_5} \qquad (3.30)$$

Furthermore, electroneutrality implies that the ionic current generated by the chemical reaction must be balanced by the electronic current:

$$\mathbf{j}_{ion}^{chg}\cdot\hat{\mathbf{y}}\big|_{\Gamma_5} = -\mathbf{j}_{eon}^{chg}\cdot\hat{\mathbf{y}}\big|_{\Gamma_5} \qquad (3.31)$$

Substituting Eqs. (3.16) and (3.31) into Eq. (3.30) and writing out the equation for both ionic and electronic carriers gives:

$$D_{eon}c_{eon}^{eq}\left(\frac{\partial c_{eon}^{*(1)}}{\partial y} - \frac{\partial \phi^{*(1)}}{\partial y}\right)\bigg|_{\Gamma_5} = -\frac{k_B T}{e^2}kc_{eon}^{*(1)}\left(1+\frac{c_{eon}^{eq}}{4c_{ion}^{eq}}\right)\bigg|_{\Gamma_5} \qquad (3.32)$$

$$D_{ion}c_{ion}^{eq}\left(\frac{c_{eon}^{eq}}{c_{ion}^{eq}}\frac{\partial c_{eon}^{*(1)}}{\partial y} + 4\frac{\partial \phi^{*(1)}}{\partial y}\right)\bigg|_{\Gamma_5} = -\frac{k_B T}{e^2}kc_{eon}^{*(1)}\left(1+\frac{c_{eon}^{eq}}{4c_{ion}^{eq}}\right)\bigg|_{\Gamma_5} \qquad (3.33)$$

Combining Eqs. (3.32) and (3.33) and rearranging gives the following boundary conditions which describe the first-order chemical reaction taking place on the MIEC | gas interface:

$$\frac{\partial c_{eon}^{*(1)}}{\partial y}\bigg|_{\Gamma_5} = -\frac{k_B T}{e^2}\frac{kc_{eon}^{*(1)}}{4D_{ion}c_{ion}^{eq}}\left(1+\frac{4D_{ion}c_{ion}^{eq}}{D_{eon}c_{eon}^{eq}}\right)\bigg|_{\Gamma_5} \qquad (3.34)$$

$$\frac{\partial \phi^{*(1)}}{\partial y}\bigg|_{\Gamma_5} = -\frac{k_B T}{e^2}\frac{kc_{eon}^{*(1)}}{4D_{ion}c_{ion}^{eq}}\left(1-\frac{D_{ion}}{D_{eon}}\right)\bigg|_{\Gamma_5} \qquad (3.35)$$

3.7.1.3 Numerical Methods

Numerical solutions to the differential equations and boundary conditions (summarized in Appendix A) were pursued using an h-adapted, finite element method (FEM) on an anisotropic triangular mesh.[90] The equations were discretized on a triangular conforming mesh, using quadratic lagrangian basis functions with a third order bubble, and then solved using FreeFem++.[91] The mesh was adaptively refined up to seven times at each solution step according to the method illustrated in previous work.[74] The h-adaptation ensures high regularity of the H^1 estimator, locally below 0.01%, and it guarantees that the mesh is finer where the sharpest gradients occur. Accordingly, the mesh adaptivity results in coarseness everywhere except in the vicinity of the interfaces (Figure 3.11); in particular, the refinement increases as the triple phase boundary is approached. Integral tests were also implemented in order to ensure that at each iterated solution the numerical method is consistent with the boundary conditions and that it satisfies global conservation of charge. Finally it should be noted that FreeFem++ execution time is comparable to custom-written C++ code. Due to the sparsity of the problem and its relatively small size (typically involving less than 2×10^5 degrees of freedom), UMFPACK fast direct linear solver[92] was utilized to reduce the solution time.

3.7.1.4 Simulation Parameters

Oxygen vacancy and polaron diffusion coefficients in SDC15, along with formation energies, were extracted from electrochemical impedance spectroscopy measurements (Section 3.4). These parameters are essentially identical to values determined by a similar experiment,
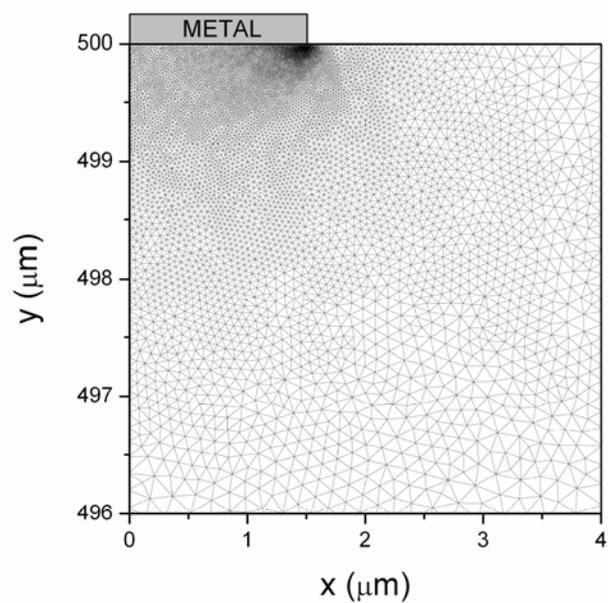
(a)
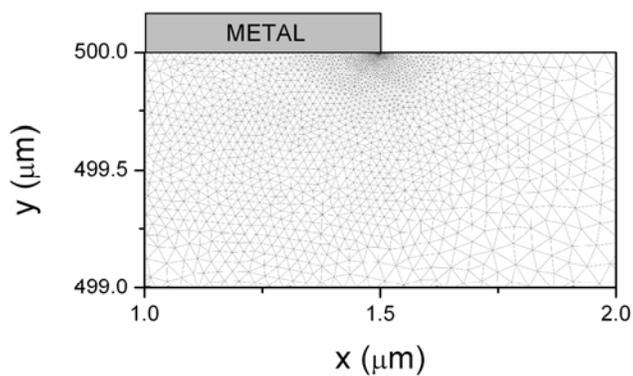
(b)

Figure 3.11: Example of a refined mesh-grid used for the numerical finite-element solution. (b) is a zoomed-in view of (a).

reported by Lai & Haile.[2] For this simulations, bulk parameters from Lai & Haile were used. Turning to the remaining parameter, the surface reaction rate-constant (describing hydrogen electro-oxidation over ceria surface), the p_{O_2}-dependent rate law reported in Section 3.5 ($k = \tilde{R}_{rxn}^{*-1} = k^0 p_{O_2}^{-1/4}$) is used. Because the absolute value of k^0 depends on surface microstructure

Table 3.3: Simulation parameters for porous metal | SDC15 | porous metal symmetric cell in H_2-H_2O-Ar. Values inside parentheses indicate range examined.

Parameter	Value	Unit
T	650	°C
p_{O_2}	$(2 \times 10^{-21} - 4 \times 10^{-26})$	atm
D_{ion}	1.96×10^{-10}	$m^2\ s^{-1}$
D_{eon}	6.46×10^{-9}	$m^2\ s^{-1}$
ΔG^0_{red}	3.09	eV
ΔG^0_g	-4.08	eV
c_{dop}	3.75×10^{27}	m^{-3}
W_1	1.5 (0.5 to 3)	μm
W_2	2.5 (0.1 to 15)	μm
l	500	μm
k^0	$(6 \times 10^{-3} - 6 \times 10^{-8})$	$\Omega^{-1}\ cm^{-2}\ atm^{\frac{1}{4}}$

and cannot be readily extracted from typical experiments, a range of discrete values of k^0 were

utilized in the calculations. In general, the effects of surface reaction rate, oxygen partial pressure

and current collector pattern dimension on carrier distribution and equipotential and flux lines

(for both ionic and electronic carriers) were explored. The bulk parameters were, in all cases,

held fixed as those listed in Table 3.3.

3.7.2 **Numerical Results**

3.7.2.1 Analysis Quantities: Resistances and the 'Surface-Influence-Zone'

The computed iso-electrochemical potential and flux lines for oxygen vacancies and

electrons are presented in Figure 3.12 for a typical set of conditions ($T =$ 650 °C,

$p_{O_2} = 4.1 \times 10^{-26}$ atm, at which the electronic transference number is 0.86) and three

representative reaction rate-constants: $k^0 =$ 3 × 10^{-7}, 6 × 10^{-7}, and 3 × 10^{-5} Ω^{-1} cm^{-2} $atm^{\frac{1}{4}}$).

While the calculation is explicitly carried out for a voltage perturbation of 1 V between Γ_1 and Γ_4, the assumption of linearity, which applies to small perturbations, implies that the relative values of the electrochemical potentials are more meaningful than their absolute values. In general, the oxygen vacancy equipotential and flux lines are linear through the bulk of the cell. In the vicinity of the termination of the MIEC, these lines bend gently around the vacancy-blocking MIEC | metal interface (Γ_4) (Figure 3.12 (b,d,f)). In contrast, the equipotential and flux lines for electrons are sharply non-linear even at some distance removed from the termination of the MIEC (Figure 3.12 (a,c,e)). Moreover, the plots clearly reveal that, in addition to a flow of electronic current between the electrodes on opposing sides of the cell, electronic current flows laterally between the metal current collector (Γ_4) and the MIEC | gas (Γ_5) surface.

To establish the resistance terms that characterize the electrode interfacial impedance, it is necessary to describe and quantify these various currents. Current that crosses Γ_1, in direct response to an applied bias across the metal current collector at Γ_4, is termed cross-plane current and is denoted by the superscript 'CP'; that which does not cross Γ_1 is termed in-plane current and denoted by 'IP'. Because of the vacancy-blocking behavior of the MIEC | metal interface, the entirety of the ionic current is cross-plane in nature. In contrast, both cross-plane and in-plane electronic current exist, as already noted, where the in-plane electronic current is generated as a result of the electrochemical reactions. The magnitude of the in-plane electronic current is precisely equal to the ionic cross-plane current, in accord with the global electrochemical reaction, Eq. (1.2). The charge flow associated with each of these three currents is explicitly indicated in Figure 3.12(a). Noting that current is simply the integrated flux over a given area, the following formal definitions and relationships apply to these currents:
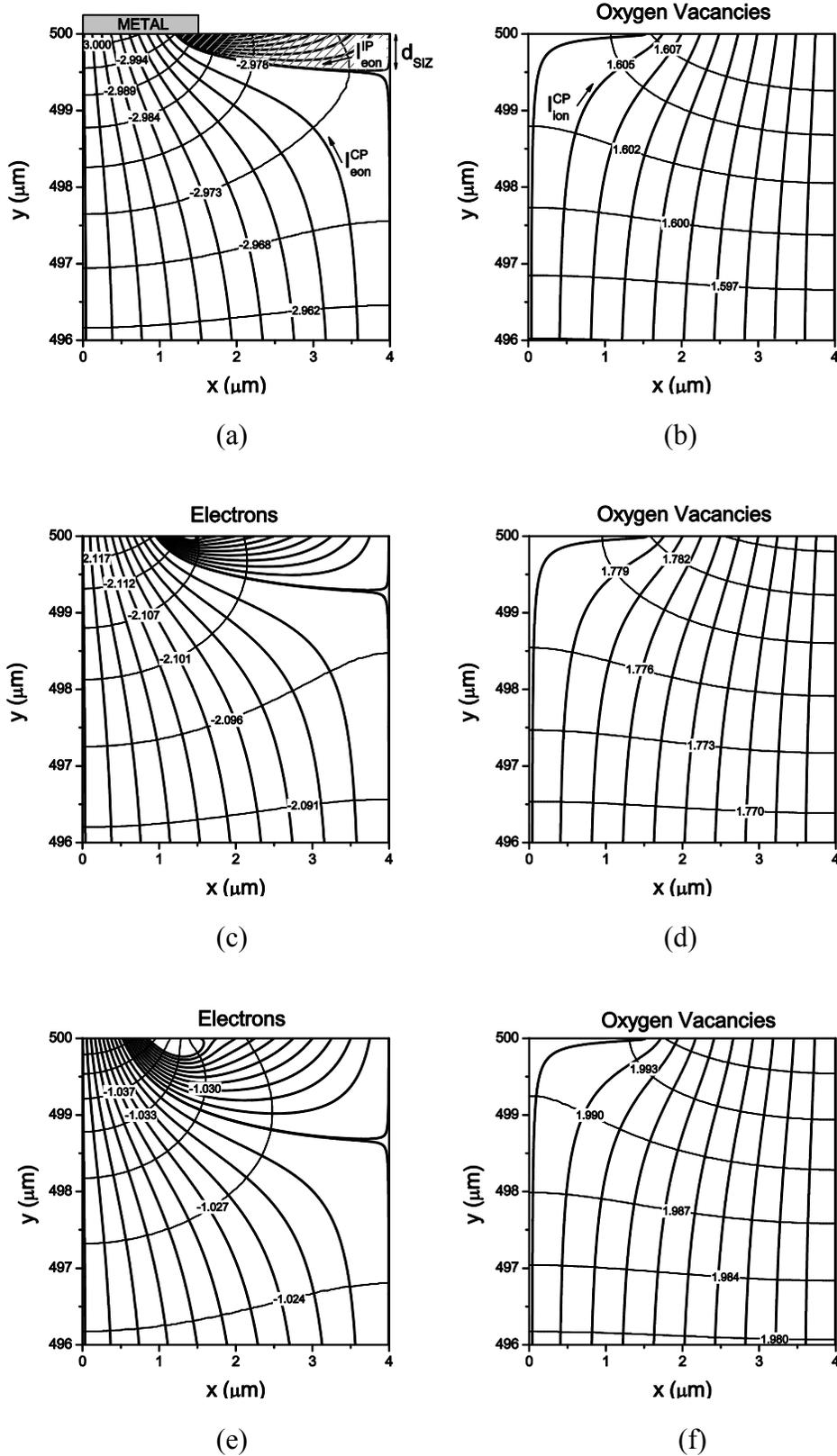
Figure 3.12: Electronic and ionic electrochemical equipotential lines (thin) and the corresponding current flux lines (thick) computed at $T=650\,°C$ and $p_{O_2} = 4.1 \times 10^{-26}$ atm for **(a & b)** $k^0 = 3 \times 10^{-7}$, **(c & d)** $k^0 = 6 \times 10^{-7}$, and (e-f) $k^0 = 3 \times 10^{-5}$ Ω^{-1} cm^{-2} atm$^{\frac{1}{4}}$. Highlighted area in (a) is the surface-influence-zone. Only the region close to the interface is shown; the potentials and fluxes are essentially linear beyond the region plotted.
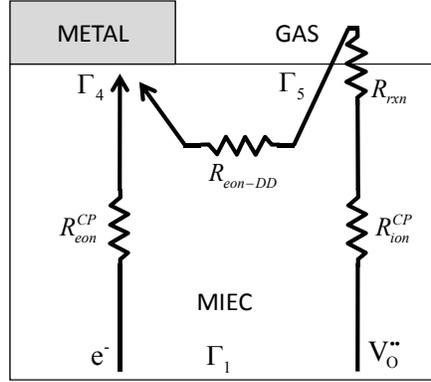
Figure 3.13: Schematic of the various current and corresponding resistances in the MIEC. Arrows indicate direction of the charge flux.

$$I_{ion}^{CP} = \int_{\Gamma_1} \mathbf{j}_{ion}^{chg} \cdot \hat{y} dx = \int_{\Gamma_5} \mathbf{j}_{ion}^{chg} \cdot \hat{y} dx \qquad (3.36)$$

$$I_{eon}^{IP} = \int_{\Gamma_5} \mathbf{j}_{eon}^{chg} \cdot \hat{y} dx \qquad (3.37)$$

$$I_{eon}^{CP} = \int_{\Gamma_1} \mathbf{j}_{eon}^{chg} \cdot \hat{y} dx \qquad (3.38)$$

$$I_{ion}^{CP} = -I_{eon}^{IP} \qquad (3.39)$$

$$I_{ion}^{IP} = 0 \qquad (3.40)$$

An experimental measurement of the total resistance across the entire electrochemical cell corresponds to a measurement of the ratio of the perturbation of the electrochemical potential of electrons on the Γ_4 surface to the total electronic and ionic current:

$$R_{TOT} = \tilde{\mu}_{eon}^{*(1)}\big|_{\Gamma_4} \Big/ \left(I_{eon}^{CP} + I_{ion}^{CP} \right) \qquad (3.41)$$

Several individual resistive steps contribute to this total cell resistance. They can be numerically

isolated by inserting the flux definitions given above with the electrochemical potential drops that occur at various positions within the cell, Figure 3.13. Four resistances are identified: the cross-plane bulk electronic resistance, R_{eon}^{CP}, the cross-plane bulk ionic resistance, R_{ion}^{CP}, the in-plane electron diffusion-drift resistance, R_{eon-DD}, and the surface reaction resistance, R_{rxn}. From Figure 3.13 , one can see that R_{rxn}, R_{eon-DD}, and R_{ion}^{CP} are connected in series because these terms correspond to the electrochemical reaction, surface and bulk diffusions necessary to form and transport oxygen vacancies across the electrochemical cell. In parallel with the transport of oxygen vacancies is the transport of electrons across the cell. Thus, the total resistance can be written as:

$$R_{TOT} = \left(\left(R_{eon-DD} + R_{rxn} + R_{ion}^{CP} \right)^{-1} + \left(R_{eon}^{CP} \right)^{-1} \right)^{-1} \tag{3.42}$$

with

$$R_{ion}^{CP} = \frac{\left\langle \tilde{\mu}_{ion}^{*} \right\rangle_{\Gamma_1} - \left\langle \tilde{\mu}_{ion}^{*} \right\rangle_{\Gamma_5}}{I_{ion}^{CP}} \tag{3.43}$$

$$R_{eon}^{CP} = \frac{\left\langle \tilde{\mu}_{eon}^{*} \right\rangle_{\Gamma_1} - \left\langle \tilde{\mu}_{eon}^{*} \right\rangle_{\Gamma_4}}{I_{eon}^{CP}} \tag{3.44}$$

$$R_{eon-DD} \approx \frac{\left\langle \tilde{\mu}_{eon}^{*} \right\rangle_{\Gamma_4} - \left\langle \tilde{\mu}_{eon}^{*} \right\rangle_{\Gamma_5}}{I_{eon}^{IP}} \tag{3.45}$$

$$R_{rxn} = \frac{\left\langle \tilde{\mu}_{ion}^{*} \right\rangle_{\Gamma_5} - \left\langle \tilde{\mu}_{eon}^{*} \right\rangle_{\Gamma_5}}{I_{ion}^{CP}} \tag{3.46}$$

where the brackets indicate averaging over the specified interface. Eq. (3.45) involves a subtle approximation in which electrons are taken to migrate between the entirety of the MIEC | metal interface and the MIEC | gas interface. Strictly, the in-plane electron diffusion-drift resistance is

given by

$$R_{eon-DD} = \frac{\left\langle \tilde{\mu}_{eon}^{*} \right\rangle_{\varphi(\Gamma_4)} - \left\langle \tilde{\mu}_{eon}^{*} \right\rangle_{\Gamma_5}}{I_{eon}^{IP}} \tag{3.47}$$

where the numerator is the difference between the reduced electrochemical potential for oxygen

vacancies averaged (as indicated by the brackets) over the MIEC | gas interface and the potential

for electrons averaged over portions of the MIEC | metal interface (indicated by $\varphi(\Gamma_4)$) that is

accessed by the in-plane diffusion-drift current. As illustrated in Figure 3.12(a), although

electrons will originate from the entire MIEC | gas interface, they will reach only a portion of the

MIEC | metal interface, due to interactions with the cross-plane electronic current coming from

the current collector on the opposite side of the cell. To properly compute $\varphi(\Gamma_4)$, one should

follow the trajectories of the electrons migrating in the in-plane direction. However, error in

R_{eon-DD} by making the approximation $\varphi(\Gamma_4) \approx \Gamma_4$ is less than 11 % under the simulation

conditions of this work. For computational simplicity, the electrochemical potential of electrons

is averaged over the entire MIEC | metal interface when calculating the electrode resistance.

The total electrode resistance, $R_{ion}^{\perp}$, is readily recognized from Figure 3.13 as the sum of

R_{rxn} and R_{eon-DD}. Combining Eq. (3.39), (3.45) and (3.46) this becomes:

$$R_{ion}^{\perp} = \frac{\left\langle \tilde{\mu}_{ion}^{*} \right\rangle_{\Gamma_5} - \left\langle \tilde{\mu}_{eon}^{*} \right\rangle_{\Gamma_4}}{I_{ion}^{CP}} = R_{rxn} + R_{eon-DD} \tag{3.48}$$

The proportion of the electrode resistance due to the surface reaction is simply:

$$f_{rxn} = \frac{R_{rxn}}{R_{rxn} + R_{eon-DD}} = \frac{R_{rxn}}{R_{ion}^{\perp}} \tag{3.49}$$

where f_{rxn} is termed the fractional surface resistance. The conventional, area-specific interfacial

resistance, $\tilde{R}$, is given by a normalization of the resistance terms relative to the macroscopic electrode area, $W_1 + W_2$ (for unit thickness). Normalization with respect to the active area, W_2, is denoted here as $\tilde{R}^*$.

In addition to interfacial resistance, it is valuable to consider the features of the surface-electron penetration into the MIEC as a result of the interaction between the in-plane and cross-plane electronic current. Figure 3.12(a,c,e) reveal that electrons injected/removed from the surface reaction site furthest from the metal current collector (the intersection of Γ_3 and Γ_5 in Figure 3.10(b)) follow a trajectory of maximum penetration and defining the boundary of the surface-influence-zone. Within this region, the entirety of the electronic current flows in the in-plane direction. The maximum penetration depth of the surface-influence-zone, d_{SIZ}, is used hereafter to quantifying the magnitude of this region.

3.7.2.2 *Influence of surface reaction rate and oxygen partial pressure*

The computed equipotential and flux lines of Figure 3.12 reveal that the oxygen vacancy behavior depends very weakly on the surface reaction rate-constant. The same is true of their dependence on oxygen partial pressure (not shown). In contrast, the electron equipotential and flux lines depend strongly on both the magnitude of the surface reaction rate-constant and the oxygen partial pressure. Accordingly, the penetration depth of the surface-reaction-zone, d_{SIZ}, also varies strongly with p_{O_2} and k^0, spanning a wide range of values from less than 0.1 to more than 4 μm under the conditions explored, Figure 3.14. The manner in which these terms establish d_{SIZ} can be understood from an evaluation of the relative magnitudes of the in-plane and

(a)

(b)

(c)

(d)
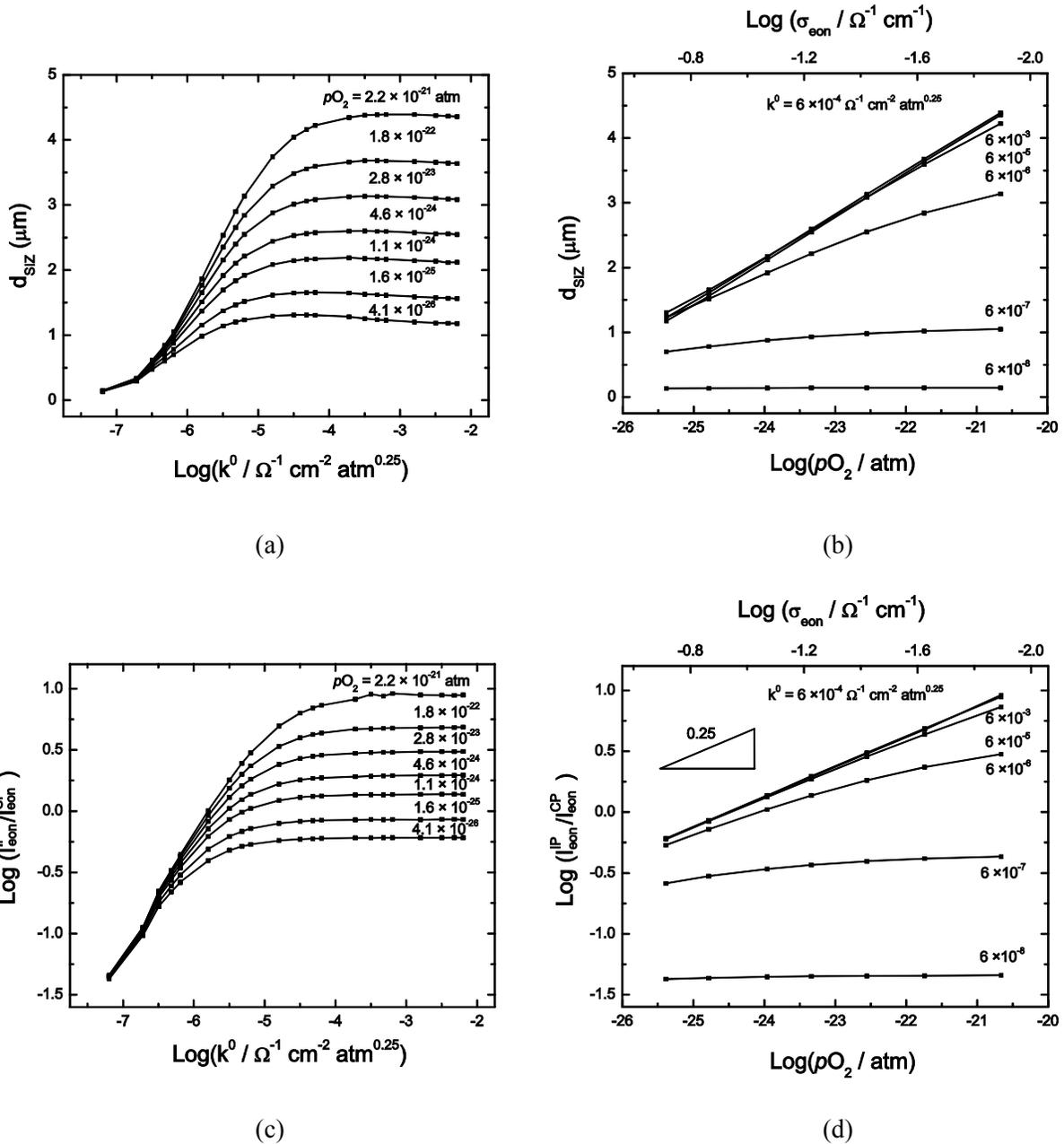
Figure 3.14: (a,b) Penetration-depth of the surface-influence-zone at various surface reaction rate-constants and oxygen partial pressures. **(c,d)** Ratio of the in-plane to the cross-plane electronic current. $T=650\,^{\circ}\text{C}$ for all plots. The bulk electronic conductivity for SDC15 is also shown for plots b & d.

cross-plane electronic currents, also presented in Figure 3.14. It is immediately evident that the two derived quantities trend in almost an identical manner with the two input variables. This behavior results because the penetration depth, Figure 3.14, reflects the position at which the two types of electronic flux attain a balance within the volume of the MIEC. For this reason, the ratio $I_{eon}^{IP}/I_{eon}^{CP}$ directly sets the magnitude of the surface-influence-zone.

The results summarized in Figure 3.14 reveal that, at fixed oxygen partial pressure, the ratio of the currents (and hence d_{SIZ}) generally increases with k^0, but eventually reaches a limiting value beyond with further increases in reaction rate have no impact. The dependence on p_{O_2} at fixed k^0 is somewhat more subtle. When k^0 is small, $I_{eon}^{IP}/I_{eon}^{CP}$ (and d_{SIZ}) are independent of p_{O_2}, but when k^0 is large, they display a $p_{O_2}^{1/4}$ dependence. These trends can be understood as follows. Because the in-plane electron current is equal in magnitude to the cross-plane ionic current (Eq. (3.39) and Figure 3.14), $I_{eon}^{IP}/I_{eon}^{CP}$ can be written as

$$\left|\frac{I_{eon}^{IP}}{I_{eon}^{CP}}\right| = \left|\frac{I_{ion}^{CP}}{I_{eon}^{CP}}\right| = \frac{R_{eon}^{CP}}{R_{ion}^{CP} + R_{rxn} + R_{eon-DD}} \tag{3.50}$$

Essentially, $I_{eon}^{IP}/I_{eon}^{CP}$ represents the relative contributions of the two parallel current paths shown in Figure 3.14.

For very low values of k^0, the surface reaction resistance dominates the denominator, and the above ratio becomes:

$$\left|\frac{I_{eon}^{IP}}{I_{eon}^{CP}}\right| \approx \frac{R_{eon}^{CP}}{R_{rxn}} \tag{3.51}$$

In this limit, $I_{eon}^{IP}/I_{eon}^{CP}$ is approximately proportional to k (Eq. (3.8)) and, hence, at fixed p_{O_2} this ratio and d_{SIZ} increase monotonically with k^0. In terms of the dependence on oxygen partial pressure both R_{rxn} and R_{eon}^{CP} scale with $p_{O_2}^{1/4}$, and thus $I_{eon}^{IP}/I_{eon}^{CP}$ and d_{SIZ} do not depend on p_{O_2}.

In the limit of very large k^0, the surface reaction resistance tends to zero, and Eq. (3.50) becomes:

$$\left| \frac{I_{eon}^{IP}}{I_{eon}^{CP}} \right| \approx \frac{R_{eon}^{CP}}{R_{ion}^{CP} + R_{eon-DD}} \approx \frac{R_{eon}^{CP}}{R_{ion}^{CP}} \tag{3.52}$$

The elimination of R_{rxn} from this expression implies both $I_{eon}^{IP}/I_{eon}^{CP}$ and d_{SIZ} become independent of k^0, as is observed. Physically, this corresponds to a situation in which the reaction rate is so fast that the rate at which electrons can be injected/removed at the MIEC | gas surface exceeds the rate at which they are removed from by diffusion-drift and hence the reaction rate no longer has any influence on the system behavior. Under the simulation conditions used in this work, $R_{ion}^{CP} \gg R_{eon-DD}$ and the role of R_{eon-DD} is also minimal in setting the behavior, as indicated in the right-side simplification to Eq. (3.52) Hence, at fixed (large) k^0 the oxygen partial pressure dependence of $I_{eon}^{IP}/I_{eon}^{CP}$ (and of d_{SIZ}) is largely established by the properties of R_{eon}^{CP}. As R_{eon}^{CP} scales with $p_{O_2}^{1/4}$, so do $I_{eon}^{IP}/I_{eon}^{CP}$ and d_{SIZ}. This combination of trends implies that the largest penetration of the surface-influence zone occurs at large k^0 and, counter-intuitively, high p_{O_2} (under which the surface injection current is low). At these extremes, which correspond to plausible physical conditions and material properties, the penetration depth exceeds the width of the MIEC | gas interface.

The explicit influences of oxygen partial and reaction rate-constant on the interfacial resistance terms, R_{eon-DD} and R_{rxn}, computed according to Eqs. (3.45) and (3.46), respectively, are presented in Figure 3.15. By definition, Eqs. (3.23) and (3.8), the surface reaction resistance scales decreases with k^0 and scales linearly with $p_{O_2}^{1/4}$, Figure 3.15(a,b). The in-plane electron diffusion-drift resistance displays a similar $p_{O_2}^{1/4}$-dependence, Figure 3.15(d), in this case due to the nature of the dependence of electronic resistivity on oxygen partial pressure, also shown in the figure. In contrast to R_{rxn}, however, R_{eon-DD}, decreases then plateaus with increasing reaction rate-constant, mirroring to some extent, the behavior of d_{SIZ}. The limiting behavior as k^0 increases simply indicates that beyond some reaction rate, the discontinuity in oxygen vacancy electrochemical potential at the Γ_5 boundary, Eq. (3.22), approaches zero, $i.e. \left\langle \tilde{\mu}_{ion}^* \right\rangle_{\Gamma_4} = \left\langle \tilde{\mu}_{eon}^* \right\rangle_{\Gamma_5}$, and the solutions (*i.e.* equipotential and flux lines) no longer depend on reaction rate, as noted above. If one considers the behavior of the overall interfacial impedance term, $R_{ion}^{\perp}$, (the sum of the reaction and electron diffusion-drift terms, Eq. (3.48)), because both component terms depend on oxygen partial pressure according to $p_{O_2}^{1/4}$, $R_{ion}^{\perp}$ will also scale with $p_{O_2}^{1/4}$ (Figure 3.16). Again, this is an immediate consequence of the selected rate law, Eq. (3.8). With respect to variations in k^0, limiting behavior also occurs for $R_{ion}^{\perp}$ as it does for other quantities, consistent with the behavior of the system overall. Specifically, as k^0 increases, the surface reaction resistance becomes negligible and $R_{ion}^{\perp}$ approaches R_{eon-DD} (Eq.(3.48)), where the latter is, in general, a finite quantity. The relative contributions of R_{rxn} and R_{eon-DD} to $R_{ion}^{\perp}$ as a function of p_{O_2} and k^0 are immediately revealed from a plot of f_{rxn} (the ratio of the R_{rxn} to $R_{ion}^{\perp}$) as a function of these two quantities, Figure 3.17. As expected, when the surface reaction is
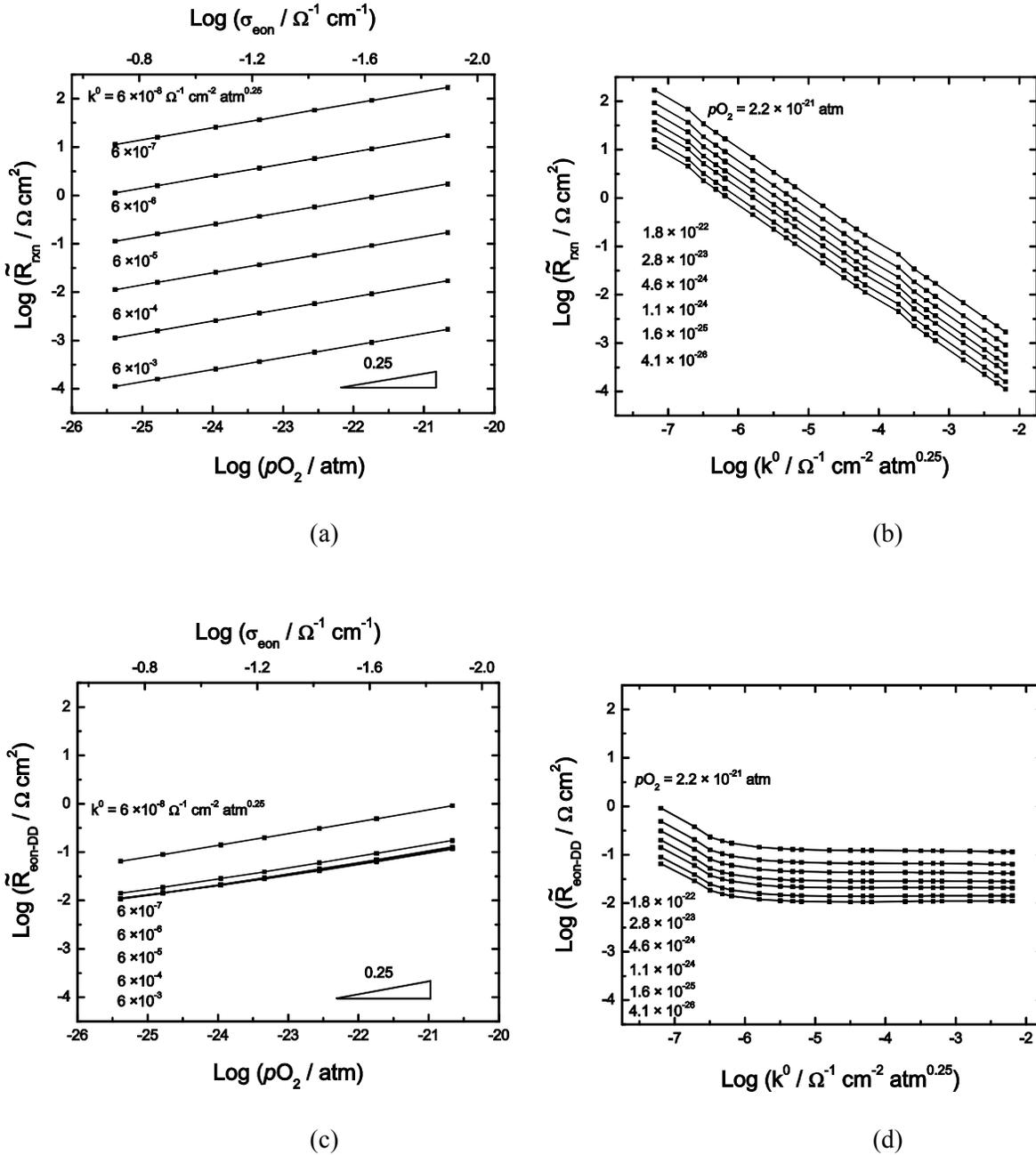
Figure 3.15: (a,b) The surface reaction resistance R_{rxn} and (c,d) the electron diffusion-drift resistance R_{eon-DD} as a function of surface reaction rate-constant and oxygen partial pressure at $T=650\,°C$. The bulk electronic conductivity for SDC15 is also shown for plots b & d.
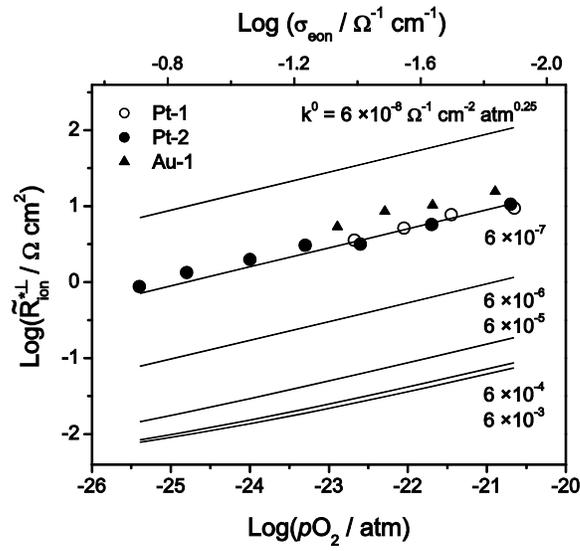
Figure 3.16: (lines) Area-specific electrode polarization resistance (normalized by the active reaction area, W_2) plotted as a function of oxygen partial pressure and surface reaction rate-constant at $T = 650\,°C$. Experimental data for SDC15 symmetric cells with Pt (circle) and with Au (triangle) metal current collectors.
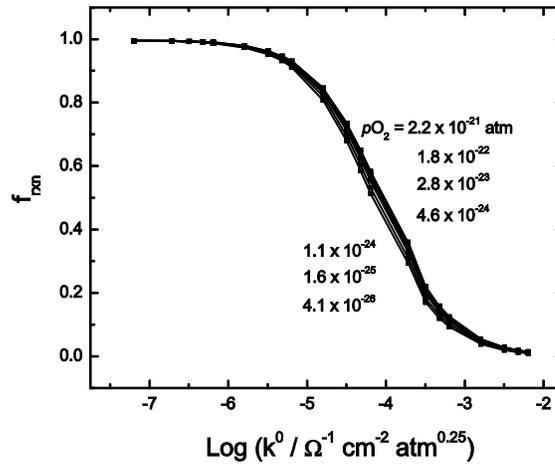
Figure 3.17: Fractional surface reaction resistance as a function of surface reaction rate-constant and oxygen partial pressure. $f_{rxn} = 1$ indicates that the electrode reaction is limited entirely by the surface-reaction, while $f_{rxn} = 0$ indicates that the electrode reaction is limited entirely by in-plane electron diffusion-drift. $T = 650\,°C$.

the electrode resistance is dominated by in-plane electron diffusion-drift resistance (f_{rxn} approaches zero). On the other hand, when the surface reaction is very slow, the electrode resistance is dominated by the surface reaction resistance (f_{rxn} approaches unity). The relative contributions of R_{eon-DD} and R_{rxn} to $R_{ion}^{\perp}$, are largely independent of oxygen partial pressure, as the surface reaction resistance and the in-plane resistance scale with pressure in the same way.

In an one-dimensional analog to the present problem, whether limiting behavior can be expected is readily predicted from an evaluation of a quantity $(kW)/\sigma$ (briefly discussed in Section 1.1.1) where W is the diffusion length. Specifically, when $(kW)/\sigma \gg 1$, the system behavior is independent of the reaction rate. In the present problem, the influence of reaction rate similarly decreases as $(kW_2)/\sigma_{eon}$ increases, but a preliminary analysis indicates that the solutions do not scale directly with this dimensionless quantity, primarily due to that the fact that the electron penetration-depth is not constant with respect to k. While a precise determination of the relevant scaling law is beyond the scope of this study, it is clear that the behavior of the system under consideration here can be approximated by the one-dimensional result (with f_{rxn} being a single-valued function of $(kW_2)/\sigma_{eon}$) *only* when k is large, underscoring the importance of a complete, two-dimensional analysis.

3.7.2.3 *Geometrical Considerations*

The influence of pattern dimensions (at a fixed temperature of 650 °C and oxygen partial pressure of $p_{O_2} = 4.1 \times 10^{-26}$ atm) are captured in a series of contour plots presented in Figure 3.18. The geometric degrees of freedom are the metal stripe width ($2W_1$) and the inter-metal-
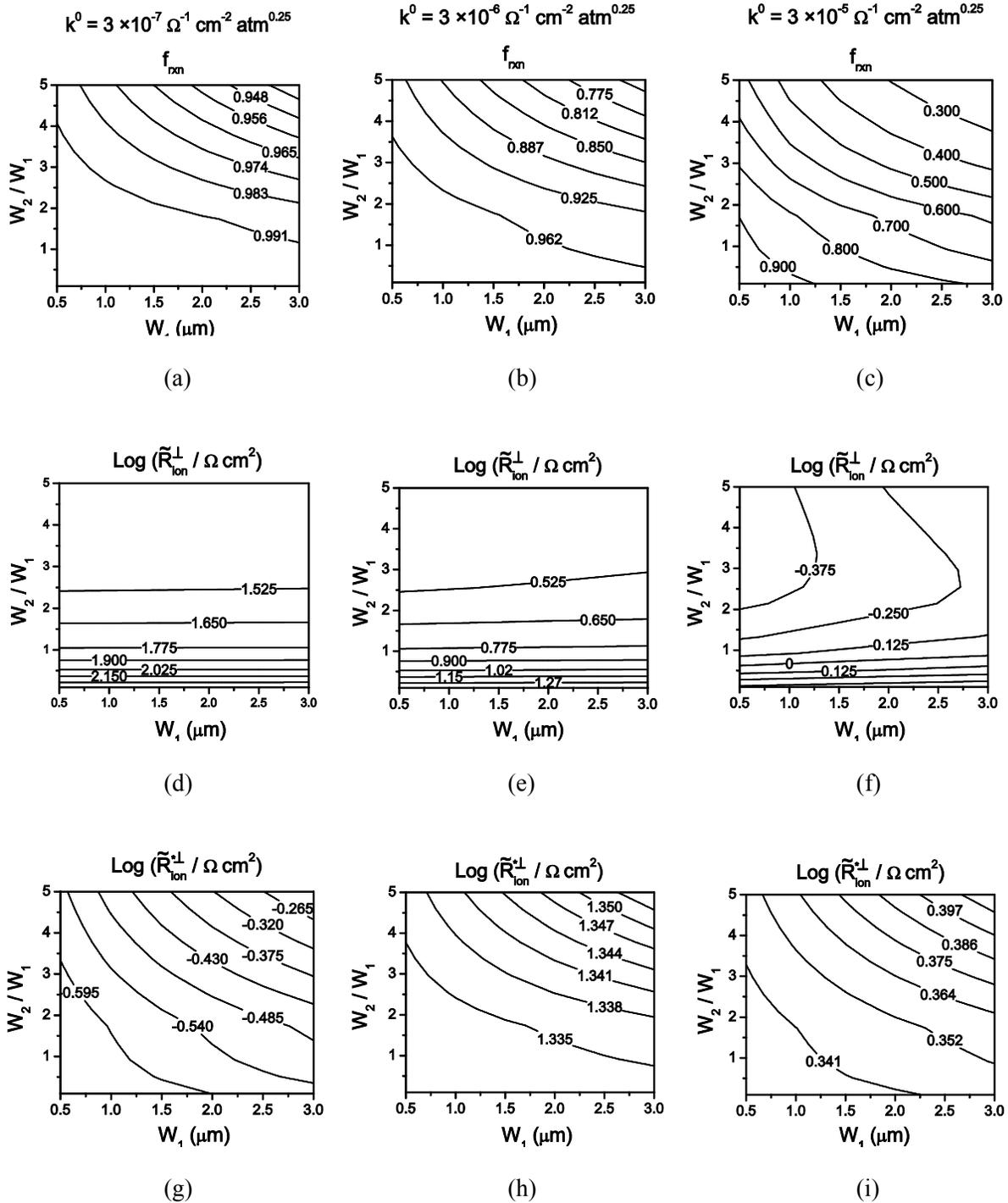
Figure 3.18: Contour plots of the fractional surface reaction resistance (f_{rxn}) (top row), the area-specific electrode resistance normalized by the total electrode area (middle row), and the electrode resistance active reaction area (bottom row), as a function of W_1 and W_2, the metal current collector stripe width and the distance between stripes, respectively. Each column represents a particular value of the surface reaction rate-constant. T=650 °C and p_{O_2} = 4.1 × 10^{-26} atm.

stripe distance ($2W_2$), represented in the plots by W_2/W_1 and W_1. Presented in the top row of images is the behavior of the fractional surface resistance, in the middle row is the total electrode resistance normalized by the total electrode area ($\tilde{R}_{ion}^{\perp}$), and in the bottom row the electrode resistance normalized by the active reaction area ($\tilde{R}_{ion}^{*\perp}$), each computed for three values of k^0.

At relatively low k^0 (Figure 3.18, left column), the interfacial process is dominated by the slow reaction rate and f_{rxn} remains close to one over the entire range of current collector geometries examined. Under these conditions, the macroscopically measured interfacial resistance, $\tilde{R}_{ion}^{\perp}$, is independent of the dimensions of the metal current collector, so long as the ratio W_2/W_1, which is a measure of the fraction of the MIEC surface that is available to support the electrochemical reaction, is fixed. Analogously, normalization by the active area gives an interfacial impedance $\tilde{R}_{ion}^{*\perp}$ that is essentially independent of current collector geometry (varying by less than 6% over the range of geometries considered). Thus, in the low k^0 regime, electron diffusion-drift does not contribute to the macroscopic electrode resistance (even for distances as long as 15 μm). Accordingly, assuming fixed material properties, minimizing the electrode resistance is achieved by maximizing the amount of active surface area available for electrochemical reaction, namely, the MIEC | gas interfacial area.

As the surface reaction rate increases (Figure 3.18, middle & right column), so does the influence of current collector geometry on electrode resistance. The fractional surface resistance attains values considerably lower than one and decreases with both increasing W_1 and W_2/W_1, indicating the electrode resistance is becoming increasingly dominated by in-plane electron diffusion. Consistent with the increased contribution from in-plane diffusion, the macroscopic

electrode resistance is no longer constant with respect to the inter-metal distance, evident in

Figure 3.18(e) and even more so in Figure 3.18(f). Furthermore, at the highest reaction rates $\tilde{R}_{ion}^{\perp}$

is no longer a monotonic function of W_2/W_1, indicating that the optimal geometry reflects a

balance between minimizing diffusion distance and maximizing reaction area. Lastly, the

electrode resistance normalized by the active area, $\tilde{R}_{ion}^{*\perp}$, displays the same trend as the fractional

surface resistance, confirming that in the regime where in-plane diffusion is no longer negligible,

current density along the MIEC | gas interface falls as the distance away from the current

collector increases.

3.7.2.4 *Comparison with Experimental Results*

Experimental data for the interfacial reaction resistance for hydrogen electro-oxidation on

SDC15 reported in Section 3.5 & 3.6 ('Au-1' & 'Pt-1') and from earlier measurements by Lai

and Haile[2] ('Pt-2') are compared to the computed results. Effective values for W_1 and W_2 for the

random porous electrodes are estimated by equating these geometric parameters to the

experimentally determined average pore size and interpore distance (obtained from

microstructural examinations). These values are summarized in Table 3.3. For these dimensions

and the limiting case of infinitely fast reaction rate, the expected total interfacial resistance, $\tilde{R}_{ion}^{\perp}$,

is on the order of 10^{-2} Ω cm^2 at 650 °C and 1×10^{-25} atm oxygen partial pressure. The

experimental value of $\tilde{R}_{ion}^{\perp}$ on the other hand, is approximately two orders of magnitude greater

than that, immediately indicating that electron diffusion-drift is not the rate-determining step. For

the case in which interfacial reaction resistance is rate-limiting, the appropriate normalization is

with respect to the active area (W_2) and, accordingly, the experimental $\tilde{R}_{ion}^{*\perp}$ values are compared

to the calculated values presented in Figure 3.16.

The comparison presented in Figure 3.16 (for the specific temperature of 650 °C) reveals several important features. Most significantly, although the interfacial impedance normalized to macroscopic area differs for the three different measurements by $\sim$ 3 times (as reported in the original works), the normalization according to active area yields experimental values that are in relatively good agreement with one another, consistent with a reaction-limited process. Moreover, observation of an experimental interfacial impedance that obeys a $p_{O_2}^{-1/4}$ rate law is not *a priori* expected. Earlier, it was speculated that this behavior, in part because it occurs for both Pt and Au current collectors, was due to a interfacial process that is limited by electron diffusion-drift, which, by definition, scales with $p_{O_2}^{-1/4}$. The present calculation, however, indicates that, barring highly unusual electron transport properties at the MIEC | gas interface, electron diffusion-drift is sufficiently rapid that it can be ruled out as the cause of the observed oxygen partial pressure dependence. The corollary of this conclusion is that some other factor, tentatively assigned as the reaction rate, must scale with $p_{O_2}^{-1/4}$. Accepting this implication, the experimental data imply a value for k^0 of approximately 6×10^{-7} Ω^{-1} cm^{-2} atm$^{1/4}$ (at $T =$ 650 °C). For the specific geometry of the Pt-1 electrodes, this value implies a penetration depth for the surface influence zone that is on the order of 0.6 μm (Figure 3.15(a)), and a fractional reaction contribution to the interfacial resistance, f_{rxn}, that is close one for all oxygen partial pressures and temperatures examined. Thus, the electrode resistance is dominated under all relevant conditions by the reaction occurring on the ceria surface, whereas the sizable penetration depth for the cross-plane electronic current suggests that any surface features are unlikely to directly influence the electron diffusion-drift behavior.
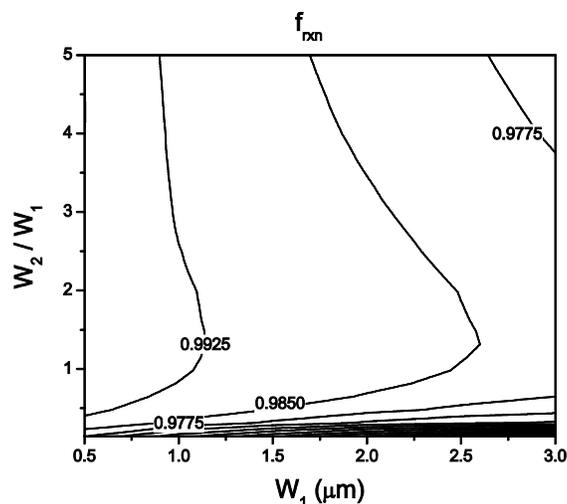
Figure 3.19: Quasi-sensitivity-analysis of the fractional surface resistance, obtained by fitting the model parameters to the Pt-1 experimental data while fixing the current collector dimensions to various values. Maximum and minimum f_{rxn} in this plot are 1.00 and 0.88, respectively. $T = 650\ °C$ and $p_{O_2} = 4.1 \times 10^{-26}$ atm.

Approximating a grid-like porous metal on ceria as line patterns could lead to errors in the fraction of MIEC | gas interface and the in-plane diffusion length. A quasi-sensitivity-analysis on f_{rxn} with respect to the geometric parameters (Figure 3.19) was performed by fitting k^0 to the experimental data (of Pt-1) at various fixed values of W_1 and W_2. Under the wide range of geometries analyzed, f_{rxn} is never lower than 0.88. Given that the fractional surface resistance is far larger than 0.5 (the case where surface reaction and electron diffusion-drift are equally co-limiting), errors in determining the current collector geometry will not shift the electrode reactions from one that is limited by surface reaction to one that is limited by in-plane diffusion.

3.8 Rate-Limiting Surface Electrochemical Step(s)

The experimental and numerical results in this Chapter concerning the hydrogen electro-oxidation reaction pathways of a metal-ceria composite electrode are summarized briefly. In

Section 3.5, by simultaneously varying hydrogen and water vapor pressure, it was shown that the rate-limiting step depends on oxygen partial pressure. In Section 3.6, the reaction mechanism is shown to be metal-independent, confirming that the metal serves mainly as a current collector rather than as a part of the 3PB active site. In Section 3.7, numerical calculations of the electrochemical potential and current distributions near the ceria surface predicts that the electron migration resistance to be on the order of 10^{-2} Ω cm^2 (T = 650 °C, p_{O_2} = 10^{-25} atm), more than two orders of magnitude smaller than the experimentally measured resistances here, effectively ruling out electron diffusion-drift between the active reaction site and the metal current collector as a rate-limiting step.

Many surface and near-surface phenomena can influence electrochemical reaction kinetics at the 2PB active region. These are: (1) adsorbate layers, (2) the surface core in which the crystal termination results in chemical and electrostatic fields, and (3) the space-charge layer as a consequence of the surface core. As depicted in Figure 3.20, surface reactions take place over the adsorbate layer and over the surface core, and electrons migrate laterally through all three layers to the metal; oxygen vacancies will migrate perpendicularly to the surface from the bulk, through the space-charge layer and then to the surface. As electron migration has been shown to be rapid, two possible rate-limiting steps remain: oxygen vacancy migration through the space-charge layer and surface reaction, where the latter is used loosely to include adsorption, chemical reactions, and ion and electron transfer reactions involving surface species. In theory, a complete model describing the surface reactions and surface core near equilibrium requires an understanding of the thermodynamics and kinetics of surface species as well as an atomistic picture of the surface. Such an analysis is beyond the scope of this work, in part due to the lack of experimentally measured parameters describing the state of the ceria surface at the
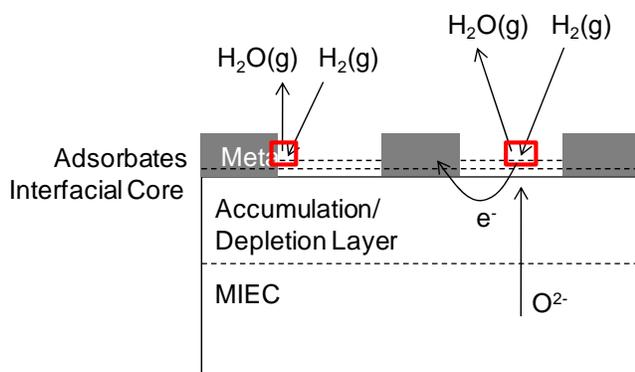
Figure 3.20: Simplified reaction pathway of a schematic porous metal – ceria electrode under reducing atmospheres. Though shown as discrete islands here, the metal features are interconnected electrically.

conditions of interest. Below, a qualitative discussion of the possible interfacial mechanisms that would give rise to the observed reaction orders is given.

Consider oxygen vacancy migration through the surface space-charge layer as the rate-limiting step. De Souza *et al.* have shown experimentally that the surface space-charge potential to be approximately 0.5 V in Fe-doped SrTiO$_3$.[93] If a sufficiently large, positive space-charge potential is also present on the SDC15 surface, significant oxygen vacancy depletion near the surface relative to the bulk is expected. Recognizing that the electrochemical potential for each carrier, in the absence of an externally applied bias or a chemical potential gradient, must be constant throughout the sample at equilibrium gives the carrier concentration profile in the space-charge layer:

$$c_i(x) = c_{i,\infty} \exp\left(-\frac{z_i e \Delta\phi(x)}{k_B T}\right) \tag{3.53}$$

where $c_{i,\infty}$ indicates the concentration of species i in the bulk (infinitely far from the interface) and dilute solution behavior is assumed. Within the framework of space-charge theory,[94-96]

oxygen partial pressure can affect vacancy migration through the space-charge layer by either modifying (1) the bulk carrier concentration or (2) the surface space-charge potential. In the case of SDC15 and under the range of p_{O_2} examined in this work, the bulk oxygen vacancy concentration is fixed by the high acceptor-doping level, so it cannot account for this observed dependence. On the other hand, the magnitude of the surface space-charge potential (*i.e.* the core charge) is likely to depend on gas atmosphere, due to the rearrangement of surface atomic structure and the variation in the coverage of charged adsorbates. While quantitative calculation of the partial pressure dependence of the surface space-charge potential, which inherently requires a detailed knowledge of the surface structure and adsorbate formation energies, is beyond the scope of this work, the observed p_{O_2} reaction order could plausibly be due to transport of oxygen vacancies in the depletion layer.

The possibility that surface reactions are rate-limiting can be assessed by examination of the p_{O_2} dependence of the surface reaction rate. Many reaction pathways are possible, and, for brevity, only one is considered below:

$$H_2(g) + 2V_{ad} \rightarrow 2H_{ad} \tag{3.54}$$

$$O_s^x \rightarrow O_{ad} + 2e_s^- + V_s^{\cdot\cdot} \tag{3.55}$$

$$H_{ad} + O_{ad} \rightarrow OH_{ad} \tag{3.56}$$

$$H_{ad} + OH_{ad} \rightarrow H_2O_{ad} \tag{3.57}$$

$$H_2O_{ad} \rightarrow V_{ad} + H_2O(g) \tag{3.58}$$

where the subscript "ad" indicates adsorbate phase and "s" indicates surface MIEC phase. Summing reactions (3.54) through (3.58) gives the global reaction:

$$H_2(g) + O_s^x \rightarrow H_2O(g) + V_O^{\cdot\cdot} + 2e_s^- \tag{3.59}$$

As a crude approximation, the adsorbate phase is assumed to behave as an ideal solution and the law of mass action applies. The MIEC surface is assumed to be nearly fully occupied with adsorbed neutral oxygen (such that the surface coverage $\theta_{O_{ad}} \approx 1$). Now, consider charge-transfer (3.55) to be the rate-limiting step, and all other reactions are taken to be reversible. For a general charge-transfer reaction

$$n_1 A_1 + n_2 A_2 + ... \rightarrow m_1 B_1 + m_2 B_2 + ... + ze^- \tag{3.60}$$
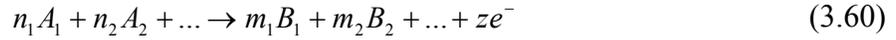
the reaction order near equilibrium conditions can be expressed as:[97-98]

$$\frac{d \log \tilde{R}_{ion}^{*\perp}}{d \log p_i} = \frac{d\left(\sum_j \log[A_i]^{0.5 n_j} + \sum_k \log[B_k]^{0.5 m_k} + \log[e^-]^{0.5 z} \right)}{d \log p_i} \tag{3.61}$$

where the brackets indicate concentration or surface coverage, p_i is the partial pressure, and the symmetry factor is assumed to be 0.5. To evaluate the reaction order, one needs to solve for the partial pressure dependence of reactant and product species of the charge-transfer reaction. The surface oxidation state and carrier concentrations ($[e_s^-]$ and $[V_s^{\cdot\cdot}]$) are expected to be substantially different from their corresponding bulk values.[99] While the exact pressure and temperature dependence of the surface oxygen vacancy and electron concentrations are not known experimentally, it is reasonable to assume that they exhibit a p_{O_2} dependence, like their bulk counterparts. As for $\theta_{O_{ad}^-}$, applying the law of mass action to reactions (3.54) and (3.56) to (3.58), the following scaling is obtained:

$$\theta_{O_{ad}^-} \propto \frac{p_{H_2O}}{p_{H_2}} \propto p_{O_2}^{1/2} \tag{3.62}$$

Therefore, the coverage/concentration of all species involved in reaction (3.55) are potentially

p_{O_2}-dependent, so, by Eq. (3.61), the exchange reaction rate is likely to depend on p_{O_2} (provided that the assumptions stated above are satisfied).

The qualitative discussion in this section shows that the experimentally observed reaction order in p_{O_2} is indeed physically possible. A significant number of pathways, rate-limiting steps, and even surface species beyond those discussed here are possible, and further theoretical and experiment work is necessary in order to advance the detailed understanding of the reaction mechanism in MIEC 2PB reactions.

Chapter 4
Electrochemistry of Thin Film Ceria

4.1 Summary

Pulsed-laser deposition and metal liftoff lithography were combined to fabricate epitaxial SDC15 and SDC20 electrochemical cells with well-defined dimensions. Kinetic and thermodynamic parameters were obtained through the precise control of microstructure and electrochemical impedance modeling. Specifically, experimentally measured thin film capacitance is decomposed into a thickness-dependent and -independent component, with the former associated with the oxygen storage capacity of ceria and the latter associated with the MIEC | gas electrochemical double-layer. Furthermore, by varying diffusion lengths and reaction site densities, the ceria | gas 2PB sites are shown to be the prevailing active sites.

4.2 Cell Configuration & Materials Characterizations

The electrochemical cell, illustrated in Figure 4.1, consists of an ion-conducting and electron-blocking substrate (IC, *e.g.* YSZ) with MIEC films (*e.g.* doped ceria) of thickness l on both sides placed in a uniform gas environment. Patterned current collectors (with stripe width $2W_1$ and inter-stripe spacing $2W_2$) directly represent the microfabricated patterns and approximate the porous metal current collectors. Symmetry of the metal patterns allows the system to be described by repeating domains, Figure 4.1(a). The flow of current in this electrochemical system (Figure 4.1(b)) consists of cross-plane ionic current and in-plane

Interconnected
Metal Patterns

MIEC

IC

MIEC

(a)

W_1

W_2

METAL

GAS

Γ_4

Γ_5

Γ_2

MIEC

Γ_3

l

Γ_6

IC

$\hat{y}$

$\hat{x}$

Γ_1

(b)

$H_2O(g)$ $H_2(g)$

METAL

GAS

e^-

MIEC

O^{2-}

IC

Figure 4.1: (a) Schematic of the electrochemical cell modeled: thin film MIEC with patterned metal current collectors on both sides of an ion-conducting, electron blocking substrate (IC). The modeling domain with the boundaries shown: Γ_1, Γ_2, and Γ_3 are symmetry lines, Γ_4 is the MIEC | metal interface, Γ_5 is the MIEC | gas interface, and Γ_6 is the MIEC | IC interface. $2W_1$ is the width of the metal current collector stripe, $2W_2$ is distance between each current collector stripe , and l is the thickness of the film. **(b)** Schematic of the two types of current in the electrochemical cell: in-plane electronic current and cross-plane ionic current. Not drawn to scale.

electronic current. This contrasts with the system modeled in Chapter 3 in that the electrons cannot flow in the cross-plane direction.

4.2.1 Ceria Thin Film by Pulsed-Laser Deposition

Thin films of SDC15 and SDC20 were deposited onto both sides of $Y_{0.16}Zr_{0.84}O_{1.92}$ (YSZ) (100), (110) and (111) oriented single crystal substrates via pulsed-laser deposition. Electron probe microanalysis confirmed that the film Sm/Ce ratio was identical, within error, to that of the polycrystalline target. XRD were employed to characterize the quality of the film (Figure 4.2). Out-of-plane XRD (2θ scan) showed only peaks corresponding to the substrate orientation and a lattice constant that was independent of film thickness. As a measure of the reproducibility of film growth, the lattice constant of deposited films varied by less than ± 0.1 % from sample to sample. Rocking curve measurements revealed a FWHM of 0.4 ° (for the (100) peak). The number of diffraction peaks observed by in-plane XRD (φ scan) was consistent, for each film orientation, with the rotational symmetry of the crystallographic plane normal to the incident beam, indicating alignment registry between the film and the substrate. The epitaxial nature of the SDC15 and SDC20 thin film was further confirmed by selective area diffraction and dark-field imaging using TEM (Figure 4.3); film thickness uniformity was found to be (± 4 %) by SEM. The independence of the lattice constant on film thickness suggests that residual stress in these films, despite their epitaxial nature, is small. In the case of molecular beam epitaxy (MBE) grown films, the ceria-cubic zirconia interface has been found to be semi-coherent with the lattice mismatch accommodated mainly by misfit dislocations,[100] and such a stress-release mechanism may also be operative here; alternatively, stresses in these relatively thick films, might not propagate far beyond the interface.

To examine thermal stability, films were annealed at 900 °C for 24 h. Electron microscopy observations, combined with chemical analysis by energy dispersive spectroscopy, showed insignificant morphological evolution and the absence of detectable cation or dopant interdiffusion between the substrate and the thin film. AFM characterization of the post-annealed film showed an average roughness of 1.4 nm (Figure 4.3).

(a)

(b)

(c)
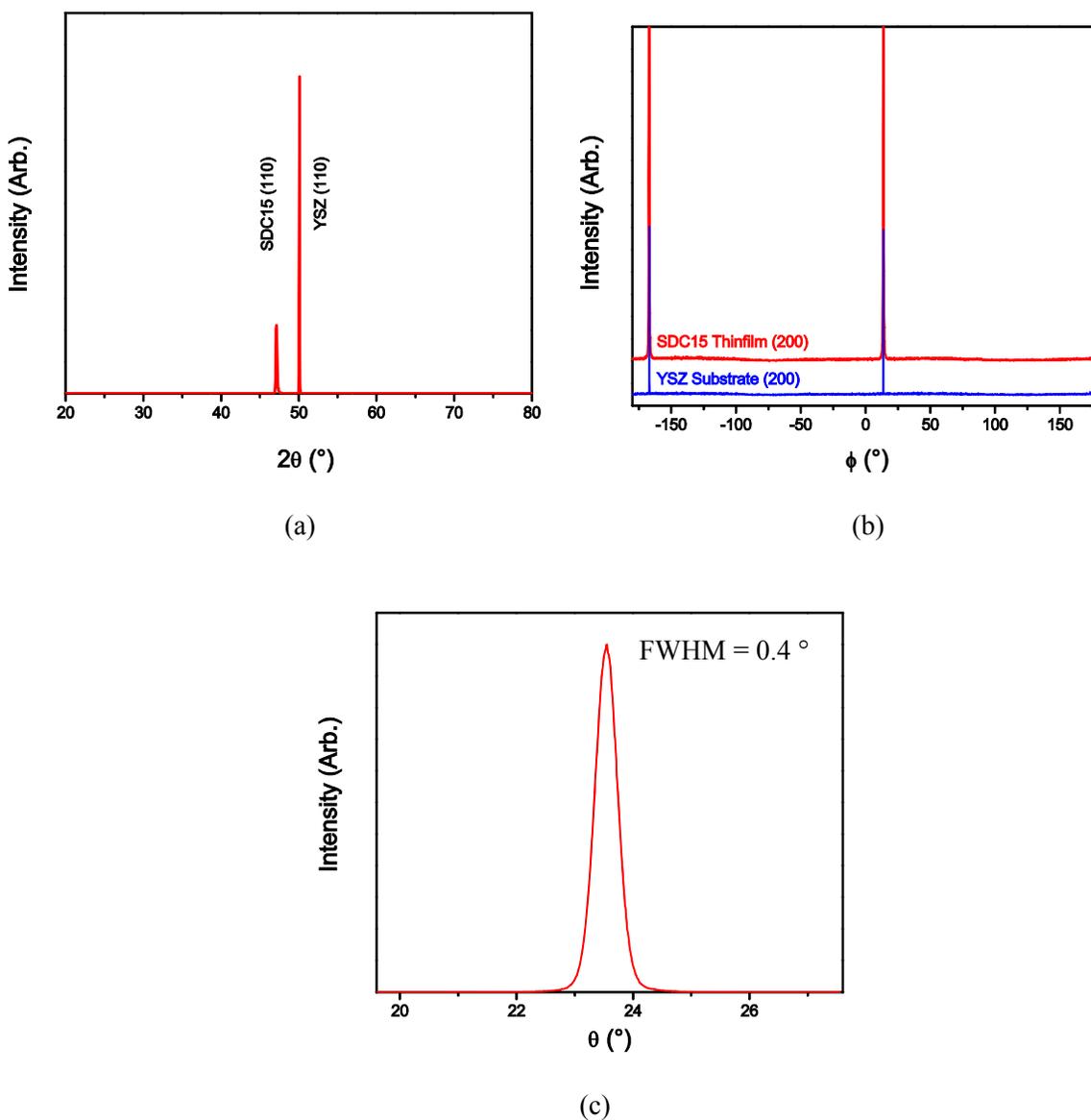
Figure 4.2: X-ray diffraction data for SDC15 epitaxial thin film grown by pulsed-laser deposition. **(a)** In-plane diffraction pattern, **(b)** out-of-plane diffraction pattern, and **(c)** rocking curve.
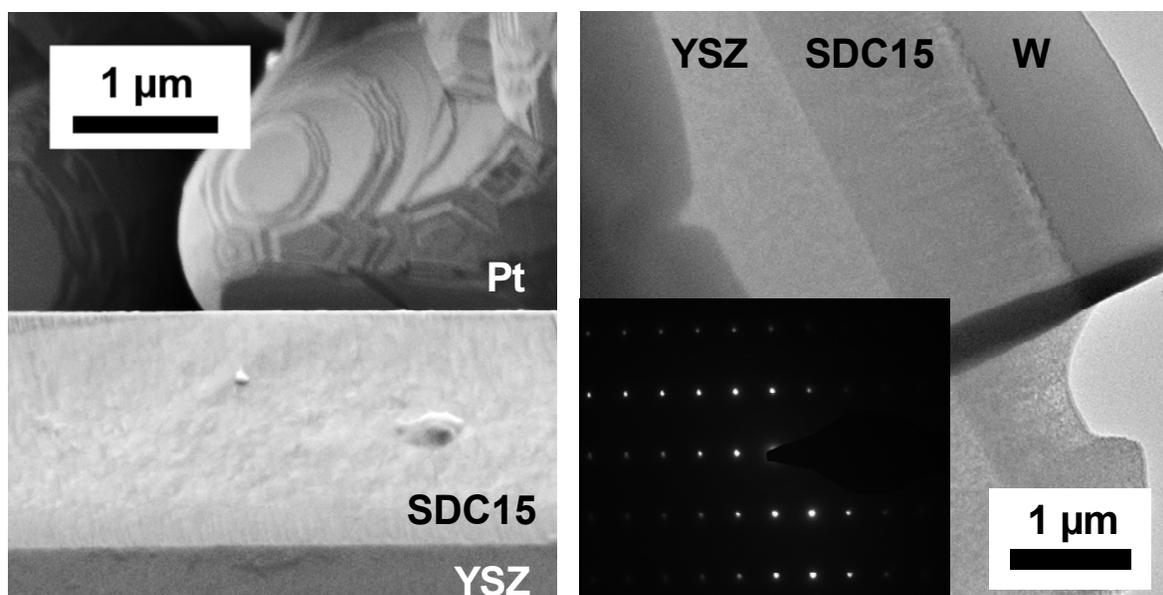
(a)

(b)
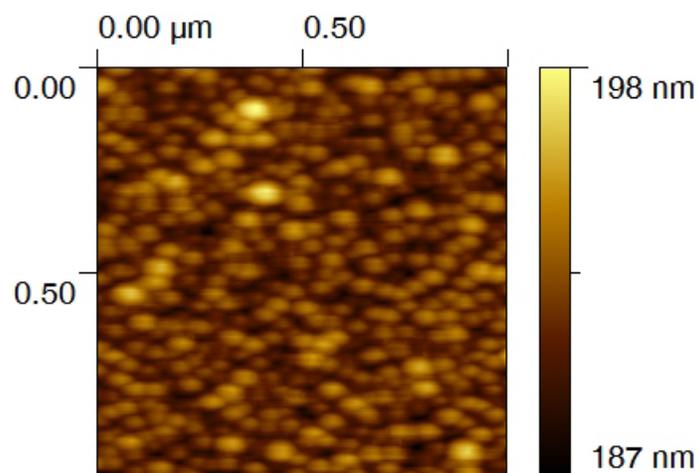
(c)

Figure 4.3: Characterization of SDC15 thin film grown by pulsed-laser deposition with various microscopy techniques. **(a)** Scanning electron micrograph showing a feature-less cross-section of the film. **(b)** Transmission electron micrograph with selective area diffraction confirming epitaxial nature of the film. **(c)** Surface topological micrograph from an atomic force microscope. The average surface roughness is 1.4 nm.

4.2.2 Current Collectors

Porous Pt current collectors were essentially identical to those used for the bulk-processed cells (Section 2.1.1), with an average metal feature width ($2W_1$) of 3 μm and a pore width ($2W_2$) of 5 μm. Microfabricated thin film current collectors (Ni, Pt) had precisely defined dimensions, summarized in Table 4.1. Owing to the small as-deposited crystallite size in the metal thin films and the tendency to coarsen at elevated temperatures, the morphology were examined and analyzed by SEM. A direct comparison of as-fabricated and tested samples (maximum temperature 650 °C) reveals that some coarsening occurred (Figure 4.4). Based on imaging analysis, the formation of holes and roughing of the metal pattern edges led to a maximum increase of ~30 % in the 3PB (*i.e.* metal | ceria interface). Adhesion of the porous and microfabricated current collector to SDC was satisfactory and no material could be removed by repeated application and removal of Scotch and carbon tape.

Table 4.1: Pattern dimensions used in the experiment. $2W_1$ is the width of the metal stripe and $2W_2$ is the distance between stripes.

W_1 (μm)	W_2 (μm)	3PB Length (cm)	2PB Area (cm^2)	3PB Density (cm^{-1})	2PB Density
2.50	2.50	1280	0.320	2010	0.500
10.0	10.0	324	0.320	500	0.500
20.0	20.0	164	0.320	250	0.500
40.0	40.0	84.4	0.320	125	0.500
5.00	75.0	84.8	0.600	125	0.938
20.0	60.0	84.6	0.480	125	0.750
40.0	40.0	84.4	0.320	125	0.500
75.0	5.00	84.1	0.0400	125	0.0625

(a)   (b)
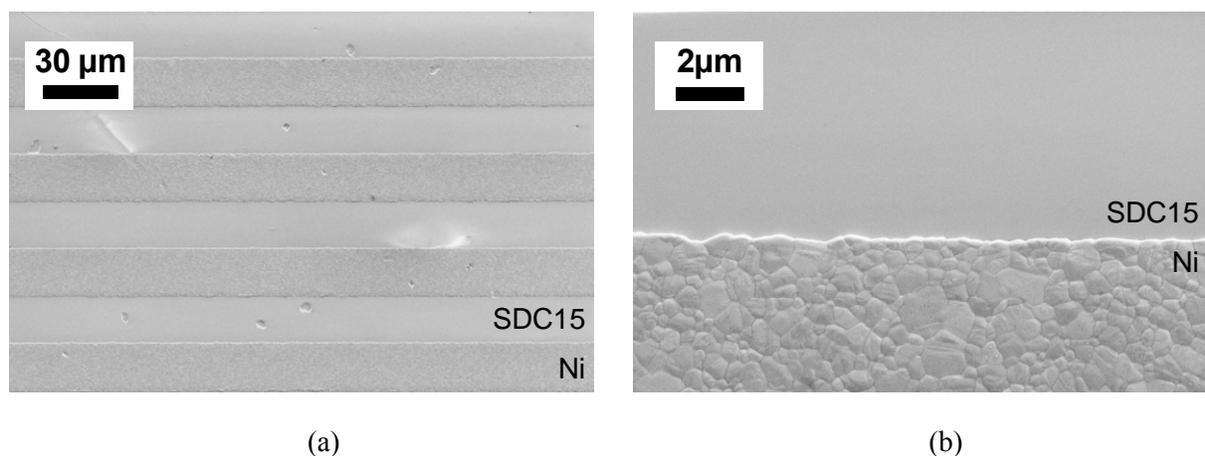
Figure 4.4: Scanning electron micrographs of Ni patterns on SDC15 thin film after electrochemical characterization (maximum temperature 650 °C). Sintering and coarsening of the nickel film led to slight roughening of the pattern edge.

4.3 Impedance Model

4.3.1 Derivation of Thin Film Impedance Model

Strictly speaking, treating diffusion-drift in both the in-plane and the cross-plane directions requires a full two-dimensional model, similar to the one developed in Section 3.7. In the interest of obtaining an analytical impedance expression, several assumptions can be made to reduce the complexity of the problem. First, the MIEC is taken to be sufficiently thin and ion-conducting such that the ion transport resistance across the film is negligible compared to all other processes. In other words, the electrochemical potential of ions is taken to be uniform within bulk of the film. Furthermore, in-plane electronic diffusion-drift is assumed to be purely

one-dimensional, which is typically valid for $W_1, W_2 \gg l$. Finally, the MIEC | IC interface is taken to be reversible to ions. With these assumptions, the problem is reduced to one dimension requiring only the treatment of electronic transport in the in-plane direction, the step-change in ionic electrochemical potential at the MIEC | gas interface, and the step-change in the electronic electrochemical potential at the MIEC | metal interface. It should be noted that treating interfaces as step-changes are in themselves approximations, which is generally valid when the microstructural dimensions are much greater than the Debye screening length L_D (0.18 nm in the case of SDC15).

4.3.1.1 Bulk Transport

It is intuitive to present the time-dependent, small perturbation impedance model in terms of an equivalent circuit that is mapped from the physical transport equations. For the same reasons outlined in Section 3.7, the small perturbation magnitude allows the material properties (namely, conductivity and relative dielectric constant, ε_r) to be approximated as bias-independent. Here, transport in a MIEC is described using the Nernst-Planck-Poisson formalism. The following transport equation is obtained for each charge carrier (*i.e.* ions and electrons) by inserting Eq. (1.25) into Eq. (1.24) :

$$j_i^{chg} = -\sigma_i^{eq} \frac{\partial \tilde{\mu}_i^{*(1)}}{\partial x} \tag{4.1}$$

where the superscript '(1)' signifies a perturbed quantity. Next, the continuity equation (Eq. (1.30)) can be rewritten in terms of the time-derivative of the chemical potential:

$$\frac{\partial j_i^{chg}}{\partial x} = -ez_i \left(\frac{\partial \mu_i^*}{\partial c_i} \right)^{-1}_{c_i = c_i^{eq}} \frac{\partial \mu_i^{*(1)}}{\partial t} \tag{4.2}$$

where, as described before, subscript 'eq' denotes equilibrium values. Finally, recognizing that the continuity equation applies to the sum of all charge carriers, the Poisson equation can be combined with it to yield:

$$\frac{\partial}{\partial x}\left[\sum_i j_i^{chg} - \frac{\partial}{\partial t}\left(\varepsilon_r^{eq}\varepsilon_0\frac{\partial\phi^{(1)}}{\partial x}\right)\right] = 0 \tag{4.3}$$

where the quantity inside the outer derivative operator is the position-independent total current, j_{tot}. The difference between j_{tot} and $\sum_i j_i^{chg}$ is the displacement current, expressed as:

$$j_{dis} = -\frac{\partial}{\partial t}\left(\varepsilon_r^{eq}\varepsilon_0\frac{\partial\phi^{(1)}}{\partial x}\right) \tag{4.4}$$

Eqs. (4.1), (4.2) and (4.3) constitute the complete set of coupled differential equations that describe one-dimensional, time-dependent transport in a MIEC.

Recall the following transport equations for electrical resistors and parallel-plate capacitors:

$$j = -\sigma\frac{\partial\phi}{\partial x} \tag{4.5}$$

$$j = \frac{C_{diel}d}{A}\frac{\partial}{\partial t}\frac{\partial\phi}{\partial x} \tag{4.6}$$

where C_{diel} is the dielectric capacitance. Comparing Eq. (4.1) to (4.5), it is immediately obvious that an electrochemical resistor (where the driving force is electrochemical rather than electrical compared to a normal resistor) can be used to represent Eq. (4.1). Similarly, comparing Eq. (4.4) to Eq. (4.6), the displacement current equation maps to a dielectric capacitor. Up to this point, the analogy between electrochemical transport equations and electrical circuit elements permits a
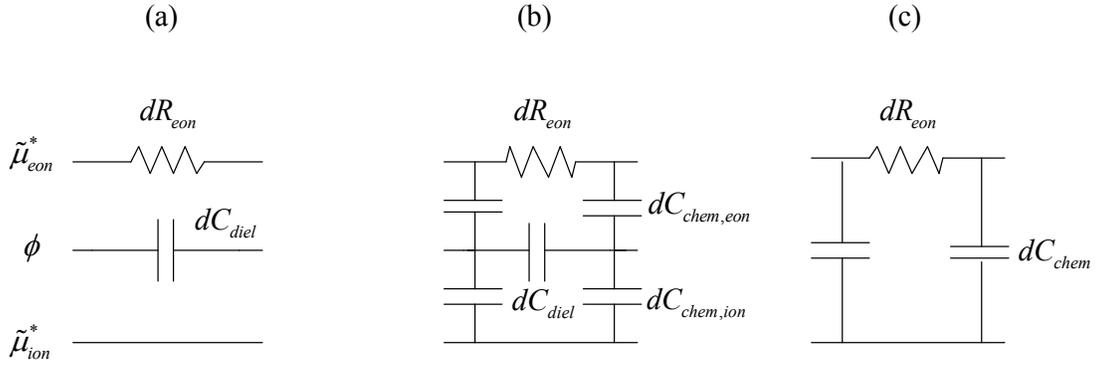
Figure 4.5: Equivalent circuit for a differential volume of a thin-film MIEC with negligible ionic transport resistance: **(a)** without and **(b)** with chemical capacitance. **(c)** Electroneutral approximation.

partial equivalent circuit to be drawn (Figure 4.5(a)), representing a differential volume within the bulk MIEC film. Three current rails are used, each representing the ionic, electronic, and displacement current, respectively. Differential resistors (with resistance $dR_i = \dfrac{dx}{\sigma_i A}$) and capacitors (with capacitance $dC_{diel} = \dfrac{\varepsilon_r \varepsilon_0 A}{dx}$) are utilized. Consistent with the assumption that the electrochemical potentials of ions are uniform within the thin film sample (indicated by the constant $\tilde{\mu}_{ion}^*\big|_{MIEC}$), all ionic differential resistors are shorted.

The remaining transport equation (Eq. (4.2), written using differential elements, is:

$$\frac{\partial j_i^{chg}}{\partial x} = \frac{j_i^{chg}(x) - j_i^{chg}(x+dx)}{dx} = -ez_i \left(\frac{\partial \mu_i^*}{\partial c_i}\right)_{c_i=c_i^{eq}}^{-1} \frac{\partial \mu_i^{*(1)}}{\partial t} \tag{4.7}$$

and implies

$$j_i^{chg}(x) - j_i^{chg}(x+dx) = -\frac{dC_{chem,i}}{A} \frac{\partial \mu_i^{*(1)}}{\partial t} \tag{4.8}$$

where the differential chemical capacitance (for species i) is given as

$$dC_{chem,i} = \left(\frac{\partial \mu_i^*}{\partial c_i} \right)^{-1}_{c_i = c_i^{eq}} ez_i A dx \qquad (4.9)$$

Because the time-varying driving force in Eq. (4.8) is the chemical potential (rather than the electrochemical potential, hence the nomenclature "chemical capacitor"), this differential capacitor is placed between the electrochemical (either ions or electrons) and the displacement rail (recall that $\mu_i^{*(1)} = \tilde{\mu}_i^{*(1)} - \phi^{(1)}$). Such a placement is also consistent with Kirchoff's Law (total current at any branch point in a circuit is zero) which requires one terminal of the differential chemical capacitor to be connected to the junction between two differential electrochemical resistors along the same current rail. The physical meaning of chemical capacitance is discussed in detail in Section 4.3.5. With the addition of the chemical capacitors, the bulk equivalent circuit is now complete and directly maps Eqs. (4.1), (4.2) and (4.3).

The equivalent circuit representing the bulk MIEC thin film can be further simplified by imposing bulk electroneutrality. Under this assumption, change in the ionic chemical capacitance (due to a change in the carrier concentration) must be precisely balanced by a matching change in the electronic chemical capacitance, so that there is no net charge accumulation or depletion in the MIEC. In other words, current flowing into the two chemical capacitors must be identical. As a result, the ionic and electronic differential chemical capacitors can be decoupled from the displacement current rail (since it is assumed that no current flows into that rail) and simply connected to each other, with the total capacitance given as:

$$dC_{chem} = \left(dC_{chem,ion}^{-1} + dC_{chem,eon}^{-1} \right)^{-1} \qquad (4.10)$$

4.3.1.2 Boundary Conditions

Three boundary conditions need to be specified in order to complete the equivalent circuit: (1) electron transfer between the MIEC and the metal (Γ_4), (2) electron transfer between MIEC and the gas phase (Γ_5), and (3) ion transfer between the MIEC and the gas phase. As one of the assumptions invoked to simplify the problem from two to into one dimension, the MIEC | IC ion transfer is taken to be reversible. Furthermore, for the same reason given in Section 3.7.1.2, MIEC | metal and MIEC | gas electron transfer resistance are also taken to be negligible compared to other resistance in the system. Specifically, for the MIEC | metal interface:

$$\tilde{\mu}_{eon}^{*(1)}\Big|_{\Gamma_4} = \tilde{\mu}_{eon}^{*(1)}\Big|_{M} \tag{4.11}$$

where $\tilde{\mu}_{eon}^{*(1)}\Big|_{M}$ is the externally applied bias on the metal. As for the remaining MIEC | gas interface, the boundary condition from Section 3.7.1.2 is used:

$$\mathbf{j}_{ion}^{chg}\Big|_{\Gamma_5} = -k_{rxn,2PB}\left(\tilde{\mu}_{eon}^{*(1)}\Big|_{\Gamma_5} - \tilde{\mu}_{ion}^{*(1)}\Big|_{MIEC}\right) \tag{4.12}$$

with

$$k_{rxn,2PB} = \tilde{R}_{rxn,2PB}^{*-1} \tag{4.13}$$

where $k_{rxn,2PB}$ is the surface reaction-rate constant at the 2PB and $\tilde{\mu}_{ion}^{*(1)}\Big|_{MIEC}$ is the perturbed electrochemical potential of ions in the MIEC (which is zero). For now, the surface reactivity is assumed to be homogeneous across the MIEC | gas 2PB interface (*i.e.* no activity enhancement at the 3PB). The above boundary condition takes the form of the resistor equation (Eq. (4.5)). Based on the form of this boundary condition, the MIEC | gas ion transfer (surface reaction)
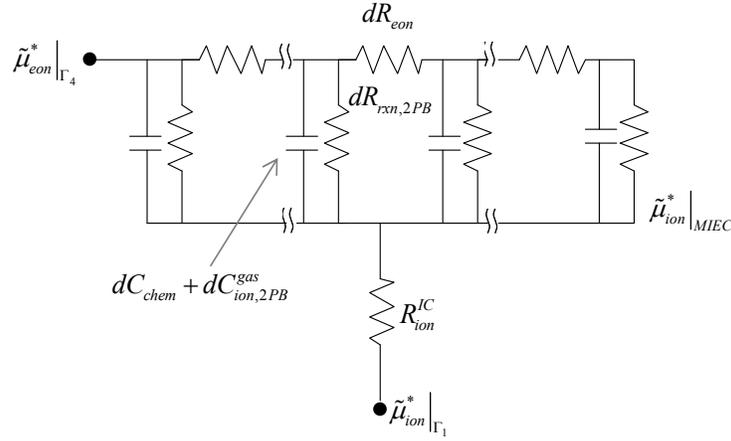
Figure 4.6: Equivalent circuit for thin-film MIEC on an ion-conducting, electron-blocking substrate. Area normalization not shown for clarity.

differential resistor can be placed between the ionic and electronic rail (in parallel to the differential chemical capacitor), Figure 4.6. Without an explicit specification of the underlying mechanism, an electrochemical capacitor (with capacitance $\tilde{C}^{gas}_{ion,2PB}$, tilde indicates an area-specific quantity) is added in parallel to the surface reaction resistor to account for double-layer charging, due to the formation of charged adsorbed layer, loss of electroneutrality, equilibrium space-charge effects, etc. Finally, while the MIEC | IC interface is taken to be reversible to oxygen ions, the bulk IC substrate has a finite ionic resistance ($\tilde{R}^{IC}_{ion}$). A resistor is used to connect the ionic rails between the two 2PB equivalent circuits representing each side of the symmetric cell.

4.3.1.3   Impedance Solution

The frequency-dependent impedance expression for the equivalent circuit is defined as

$$Z = \frac{\tilde{\mu}^{*(1)}_{eon}\Big|_{M1} - \tilde{\mu}^{*(1)}_{eon}\Big|_{M2}}{I} \tag{4.14}$$

where M1 and M2 denote the metal on both side of the symmetric cell and I is the current. To solve for the impedance function in the frequency domain, the Laplace-transformed complex impedance of resistors and capacitors are used:

$$Z_R = R \tag{4.15}$$

$$Z_C = \frac{1}{j\omega C} \tag{4.16}$$

where $j = \sqrt{-1}$ and ω is the angular frequency. Applying Kirchoff's and Ohm's Law to the equivalent circuit yields a system of differential equations which is solved analytically to give the impedance expression (normalized by the macroscopic sample area):

$$\tilde{Z}(\omega) = 2\left(\tfrac{1}{2}\tilde{R}_{ion}^{IC} + \tilde{Z}_{2PB}\right) \tag{4.17}$$

$$\tilde{Z}_{2PB}(\omega) = \frac{(W_1 + W_2)^2}{\sigma_{eon}l\beta\tanh\beta} \tag{4.18}$$

with

$$\beta = \sqrt{\frac{(W_1 + W_2)}{l\sigma_{eon}}\left(W_2 k_{rxn,2PB} + j\omega\left(\tilde{C}_{chem}(W_1 + W_2)l + \tilde{C}_{ion,2PB}^{gas}W_2\right)\right)} \tag{4.19}$$

$$\tilde{C}_{chem} = e^2\left[\left(\frac{1}{4}\frac{\partial\mu_{ion}}{\partial c_{ion}}\right)_{c_{ion}=c_{ion}^{eq}} + \left(\frac{\partial\mu_{eon}}{\partial c_{eon}}\right)_{c_{eon}=c_{eon}^{eq}}\right] \tag{4.20}$$

where the factor of 2 represents the two sides of the symmetric cell, $\tilde{C}_{chem}$ is the volumetric chemical capacitance and the tildes indicate quantities normalized by the macroscopic area. Here, $\tilde{Z}_{2PB}$ is used to signify that this equivalent circuit does not include 3PB effects. The derivative in Eq. (4.20) can be evaluated if the chemical potential of the carriers are known as a function of concentration. See Section 4.3.5 for details. In obtaining Eq. (4.18) to (4.20), it was
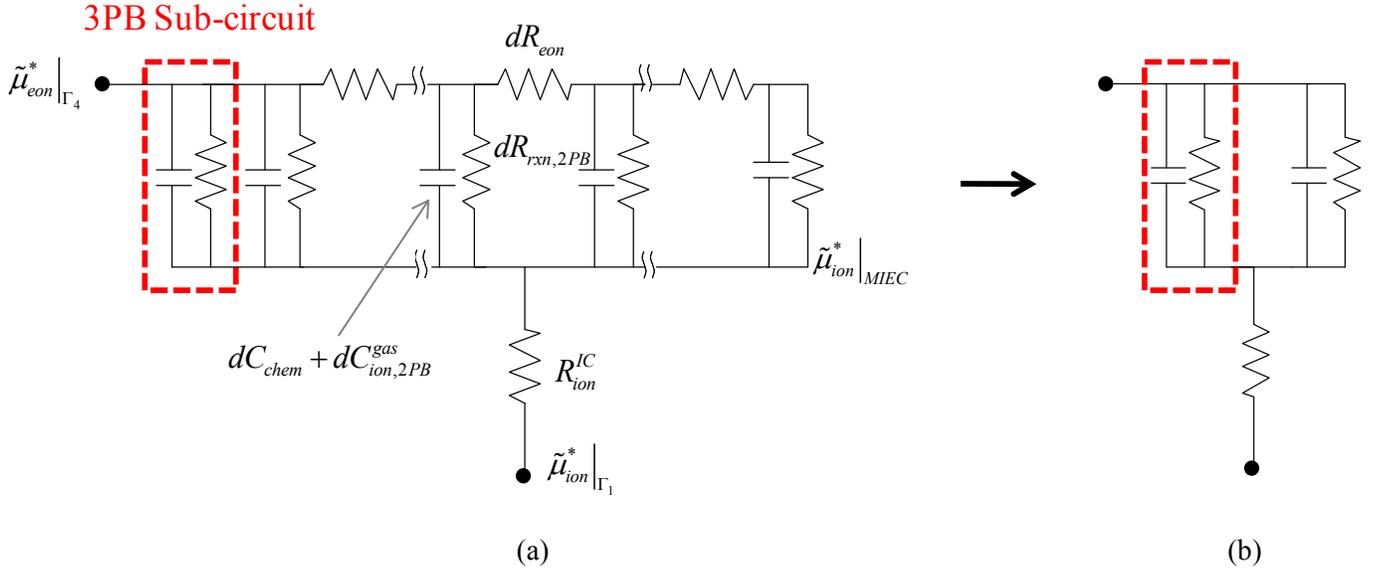
Figure 4.7: (a) Modification of the equivalent circuit to include 3PB effects. **(b)** Simplified circuit for a system is limited by surface reactions. Area normalization not shown for clarity.

tacitly assumed that electron injected at the MIEC | gas interface from the rightmost position in the computation domain (*i.e.* intersection of Γ_5 and Γ_3 boundaries) migrate to the MIEC | metal interface on the leftmost position in the domain (*i.e.* intersection of Γ_5 and Γ_2 boundaries). In other words, electron diffusion length ranges from 0 (for reaction taking place near the 3PB) to $W_1 + W_2$. The assumption that chemical potential of ions is uniform with the MIEC slab is required to avoid inconsistency in the present placement of chemical capacitors in the equivalent circuit.

4.3.2 Adding 3PB Effects

So far, the surface reaction rate-constant ($k_{rxn,2PB} = \tilde{R}^{*-1}_{rxn,2PB}$) is taken to be constant across

the entire Γ_4 boundary. In other words, the 3PB is assumed to have the same activity as the 2PB. In reality, the 3PB is likely to have a different activity then the 2PB due to the presence of the metallic phase. The assumption that the ionic electrochemical potential is constant within the MIEC permits a straightforward modification of the equivalent circuit to include 3PB effects. Using the same type of linearized boundary condition used to describe the 2PB, Eq. (4.12), the impedance expression representing the 3PB sub-circuit can be written as:

$$\tilde{Z}_{3PB}(\omega) = \left(\frac{1}{W_1 + W_2} k_{rxn,3PB} + (W_1 + W_2) j\omega \tilde{C}_{ion,3PB}^{gas} \right)^{-1} \tag{4.21}$$

where $k_{rxn,3PB}$ is the surface reaction rate-constant of the 3PB, and $\tilde{C}_{ion,3PB}^{gas}$ is a length-specific capacitor (the same type of electrochemical capacitor added in parallel to the 2PB surface reaction resistor in Section 4.3.1). Because the 3PB reactions occur directly on the metal, the sub-circuit is placed in parallel to the 2PB equivalent circuit (Figure 4.7), with the following combined impedance expression:

$$\tilde{Z}_{2PB+3PB} = 2\left[\tfrac{1}{2} \tilde{R}_{ion}^{IC} + \left(\tilde{Z}_{2PB}^{-1} + \tilde{Z}_{3PB}^{-1} \right)^{-1} \right] \tag{4.22}$$

where again the factor of two represents the two side of the symmetric cell.

4.3.3 Limiting Behaviors

Simulated impedance spectra, presented in Nyquist plots, Figure 4.10, reveal interesting limiting behaviors. First, the 2PB sub-circuit is discussed. Recall the following limits of a hyperbolic tangent function:

$$\lim_{x \to \infty} \tanh(x) = 1$$
$$\lim_{x \to 0} \tanh(x) = x$$

(4.23)

In the limit $W_2(W_1 + W_2) \gg \dfrac{l\sigma_{eon}}{k_{rxn,2PB}}$ (or $(W_1 + W_2)/(l\sigma_{eon} \cdot 1 \text{ cm}) \gg 1/(k_{rxn,2PB}W_2 \cdot 1 \text{ cm})$, where

the left-hand-side is the in-plane electronic diffusion-drift resistance and the right-hand side is

the surface reaction resistance), the 2PB impedance expression becomes

$$\tilde{Z}_{2PB}(\omega) = \frac{(W_1 + W_2)^2}{\sigma_{eon}l\beta}$$

(4.24)

with the impedance at the DC limit given as

$$\tilde{Z}_{2PB}(\omega \to 0) = \sqrt{\frac{(W_1 + W_2)^3}{W_2} \frac{1}{l\sigma_{eon}k_{rxn,2PB}}}$$

(4.25)

Physically, this limit corresponds to the diffusion-limited regime, where both the electronic

conductivity and the surface reaction rate contribute to the overall impedance. For reactions

occurring close to the metal current collector, the reaction rate is determined primarily by the

surface reaction rate-constant, whereas reactions occurring far from the metal current collector

are determined primarily by the electronic conductivity.

Now, consider the opposite limit where $W_2(W_1 + W_2)^2 \ll \dfrac{l\sigma_{eon}}{k_{rxn,2PB}}$. With the additional

constraint that $\omega \ll \left(\tilde{C}_{chem}(W_1 + W_2)l + \tilde{C}_{ion,2PB}^{gas}W_2 \right)^{-1}$, the 2PB impedance expression becomes:

(a)   (b)
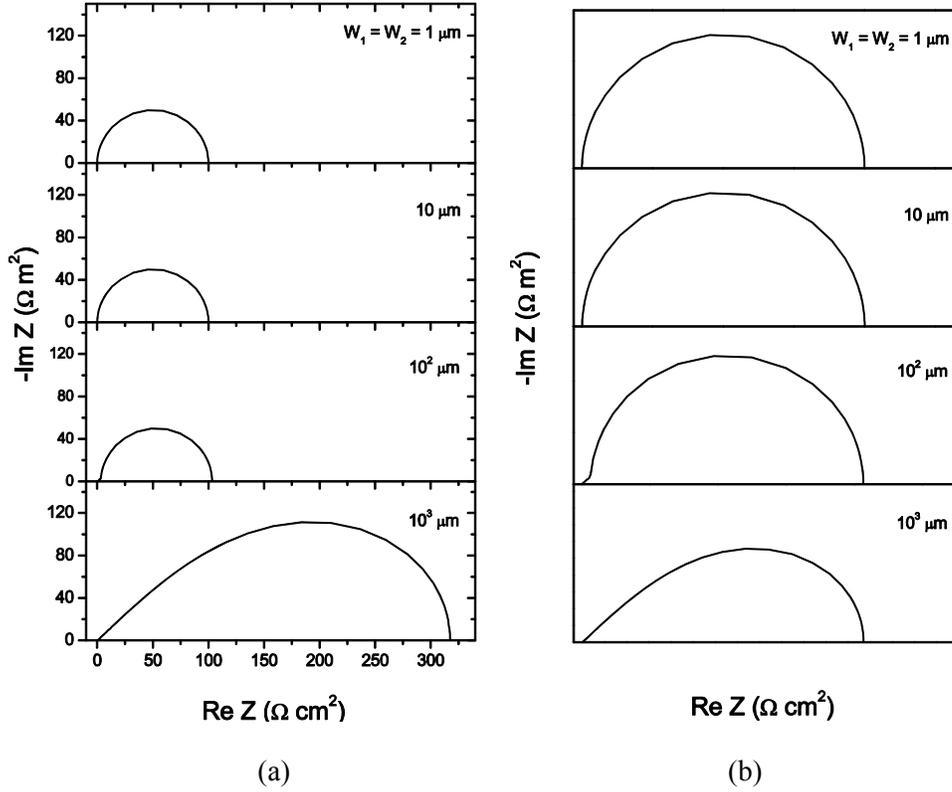
Figure 4.8: Simulated Nyquist impedance spectra for system without 3PB effects. The diffusion length is varied while holding the density of the 2PB reaction site constant. $\sigma_{eon} = 0.1\ \Omega^{-1}\ cm^{-1}$, $k_{ion,2PB}^{gas} = 0.01\ \Omega^{-1}\ cm^{-2}$, $l = 10^{-4}$ cm, $C_{chem} = 500$ F cm^{-3}, $\tilde{R}_{ion}^{IC} = 0$. (b) is rescaled plot of (a) such that the impedance arcs have the same width in the Nyquist plot.

$$\tilde{Z}_{2PB}(\omega) = \left(\frac{W_2}{(W_1 + W_2)} \left(k_{rxn,2PB} + j\omega \tilde{C}_{ion,2PB}^{gas} \right) + j\omega \tilde{C}_{chem} l \right)^{-1} \tag{4.26}$$

with the impedance at the DC limit given as

$$\tilde{Z}_{2PB}(\omega \to 0) = \frac{(W_1 + W_2)}{W_2} \frac{1}{k_{rxn,2PB}} \tag{4.27}$$

The above equation represents the circuit where a resistor and capacitor are connected in parallel (Figure 4.7). Indeed when the above limit is reached, the impedance spectra becomes a semicircle (Figure 4.10), the expected shape for a parallel resistor-capacitor circuit. Physically,

this limit corresponds to the surface-limited regime where in-plane electron diffusion-drift does not affect the transport behavior of the system. In other word, both electronic and ionic electrochemical potential are uniform within the bulk of the MIEC and gradients exist solely at interfaces.

3PB effects are added by considering Eq. (4.21) and (4.22). For the case that the 2PB reaction is diffusion-limited, the electrochemical current injected at the surface decreases away from the metal. In the limit that the total 2PB impedance is much greater than that of the 3PB , all electrochemical current is injected through the 3PB sites. Graphically speaking, this limit represents the case where all of the resistors in the 2PB sub-circuit are effectively opened. Therefore, only the 3PB sub-circuit remains, giving a semi-circle impedance spectrum in the Nyquist plot.

Now consider the opposite limit where the 2PB is surface-limited. Combining Eq. (4.21), (4.22), and (4.27), the overall equivalent circuit becomes a simple parallel resistor-capacitor network in series with a resistor representing the ionic resistance of the substrate (Figure 4.7(b)), with the area-specific resistance given by $(W_1 + W_2)\left(\dfrac{1}{k_{rxn,2PB}W_2} + \dfrac{1}{k_{rxn,3PB}} \right)$ and the capacitance given by $\tilde{C}_{chem}l + (W_1 + W_2)\tilde{C}_{ion,3PB}^{gas}$.

4.3.4 Relaxing Assumptions for the Surface-Limited Case

In the limit that transport is entirely surface-controlled, certain assumptions regarding the boundary conditions can be relaxed without loss of self-consistency. To obtain the full impedance expression (Eq. (4.18)), it was necessary to assume that the MIEC | IC interface is

reversible to ions. This assumption is no longer necessary in the surface-limited as there is no variation in transport along the lateral direction. A linear boundary condition is used to describe ion transfer across the MIEC | IC interface:

$$\mathbf{j}_{ion}^{chg}\Big|_{\Gamma_1} = -k_{ion}^{MIEC-IC}\left(\tilde{\mu}_{ion}^{*(1)}\Big|_{\Gamma_6} - \tilde{\mu}_{ion}^{*(1)}\Big|_{\Gamma_6,IC}\right) \tag{4.28}$$

with the transfer rate-constant

$$k_{ion}^{MIEC-IC} = \left(\tilde{R}_{ion}^{MIEC-IC}\right)^{-1} \tag{4.29}$$

The subscript 'Γ_6, IC' denotes the region in the substrate immediately beyond the MIEC-substrate interface. Similar to the MIEC | gas interface, a phenomenological electrochemical capacitor (with capacitance $\tilde{C}_{ion}^{MIEC-IC}$) is added to account for double-layer charging at the MIEC | IC interface. The equivalent circuit is shown in Figure 4.9.

4.3.5 Chemical Capacitance

In mapping MIEC transport equations to an equivalent circuit, chemical capacitors were used to represent the change in carrier concentrations in response to the change in chemical potentials. Such a capacitance is analogous to the conventional dielectric capacitance, given by

$$C_{diel} = \frac{\partial q}{\partial \phi} \tag{4.30}$$

$$\left.\tilde{\mu}^*_{eon}\right|_{\Gamma_4}$$

$$C_{chem} + C^{gas}_{rxn,2PB} + C^{gas}_{rxn,3PB} \qquad \left[\left(R_{rxn,2PB}\right)^{-1} + \left(R_{rxn,3PB}\right)^{-1}\right]^{-1}$$

$$\left.\tilde{\mu}^*_{ion}\right|_{MIEC}$$

$$C^{MIEC-IC}_{ion} \qquad R^{MIEC-IC}_{ion}$$

$$\left.\tilde{\mu}^*_{ion}\right|_{\Gamma_6,IC}$$

$$R^{IC}_{ion}$$

$$\left.\tilde{\mu}^*_{ion}\right|_{\Gamma_1}$$
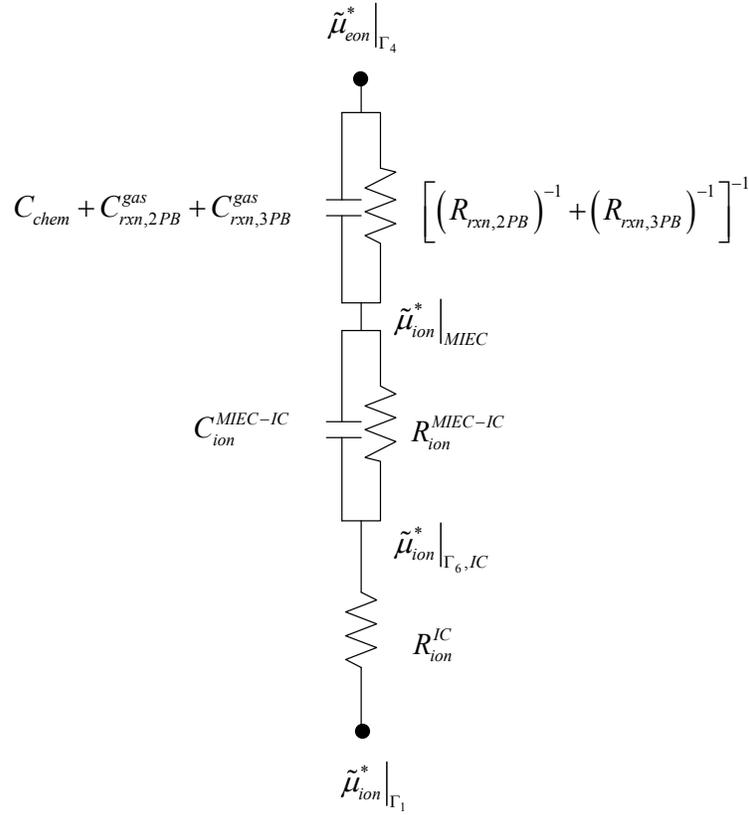
Figure 4.9: Equivalent circuit for a thin film MIEC limited by surface-reactions supported on an ion-conductor. Area normalization not shown for clarity.

where q is the accumulated charge. In the case of a metal oxide that undergoes a change in oxygen content in response to a change in oxygen chemical potential, the electrical equivalent of the chemical driving force similarly induces a change in stored charge.[2,8,65-66,101-104] Thus, chemical capacitance for the ith charge carrier is defined as

$$C_{chem,i} = \frac{dq_i}{d\mu_i^*} \qquad (4.31)$$

For a sample with a macroscopic volume V, the total charge due to species i is $q_i = ez_ic_iV$, where c_i is the volumetric carrier concentration. Combining these expressions, the chemical

capacitance can be written as:

$$C_{chem,i} = (ez_i)^2 V \frac{dc_i}{d\mu_i}$$

(4.32)

For electroneutral, nonstoichiometric metal oxides with oxygen vacancies and electrons as the charge carriers, the total chemical capacitor is simply the individual capacitor of the charge carriers connected in series (shown in Figure 4.5):

$$C_{chem} = \left(\frac{1}{C_{chem,ion}} + \frac{1}{C_{chem,eon}} \right)^{-1} = e^2 V \left(\frac{1}{z_{ion}^2} \frac{d\mu_{ion}}{dc_{ion}} + \frac{1}{z_{eon}^2} \frac{d\mu_{eon}}{dc_{eon}} \right)^{-1}$$

(4.33)

Assuming local equilibrium, the chemical potential of the neutral oxygen vacancy is the sum of the constituent defects (*i.e.* one oxygen vacancy and two electrons). Substituting Eq. (1.14) and the electroneutrality condition ($2dc_{ion} \approx dc_{eon}$) into (4.33) yields:

$$C_{chem} = -4e^2 V \left(\frac{dc_{eon}}{d\mu_O} \right)$$

(4.34)

Experimentally, it is convenient to vary the oxygen partial pressure instead of the chemical potential. Applying Eq. (1.11), one obtains

$$C_{chem} = -\frac{4e^2 V c_{eon}^{eq}}{k_B T} \left(\frac{d \ln c_{eon}}{d \ln p_{O_2}} \right)_T$$

(4.35)

Finally, the volumetric electron concentration can be expressed in terms of the oxygen nonstoichiometry δ by noting that $c_{eon} = 2\delta c_{eon}^0$:

$$C_{chem} = -\frac{8e^2 V c_{eon}^0 \delta}{k_B T} \left(\frac{d \ln \delta}{d \ln p_{O_2}} \right)_T$$

(4.36)

The inverse of the derivative term is known as the thermodynamic factor. In the dilute solution

limit, the factor is -¼ for doped ceria. In such a limit, the chemical capacitance is directly proportional to the oxygen nonstoichiometry (and the electronic carrier concentration):

$$C_{chem} = \frac{2e^2 V c_{eon}^0 \delta}{k_B T} = \frac{e^2 V c_{eon}^{eq}}{k_B T} \qquad (4.37)$$

The situation is slightly more complex if the thermodynamic factor is not known *a priori*, since integration of Eq. (4.36) will result in an integration constant that must be determined experimentally at each temperature.

4.4 Origin of Capacitances

In a sufficiently thick film or bulk sample the area-specific chemical capacitance is several orders of magnitude larger than the interfacial capacitances at MIEC | gas and MIEC | IC interfaces. For a typical 0.1 cm thick nonstoichiometric oxide (such as the SDC15 pellet studied in Chapter 3), the former falls in the range of 1 to 10^2 F cm^{-2}, whereas the latter is typically 10^{-3} to 10^{-5} F cm^{-2}.[2] As a result, the chemical capacitance can be treated as the prevailing capacitance and the interfacial capacitance ignored. In thin films, however, although the relative magnitudes of the capacitance terms are not *a priori* known, the interfacial capacitance, which is independent of film thickness, can become significant relative to the chemical capacitance, which is proportional to thickness. Difficulties in extracting the individual contributions to the observed capacitance as well as other experimental challenges have precluded establishment of a rigorous link between thin film chemical capacitance and carrier concentration.[105-110]

To investigate the various capacitive contributions the thin film MIECs, M | SDC15 | YSZ | SDC15 | M (where M is porous platinum and SDC15 varied in thickness
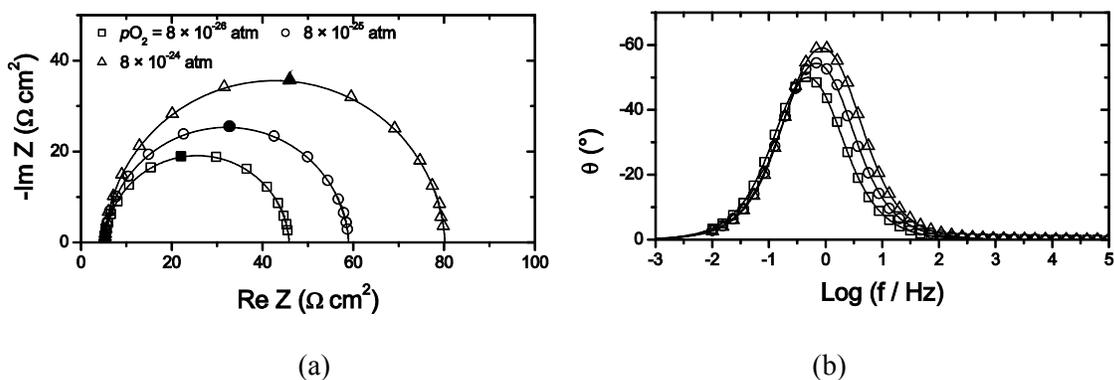
Figure 4.10: Typical impedance spectra collected at 650 °C and various oxygen partial pressures as indicated of 195 nm SDC15 deposited on both sides of a yttria-stabilized zirconia (YSZ) pure ionic conductor. In the Nyquist plot (a), the high frequency intercept corresponds to the resistance of the YSZ substrate and the Pt metal current collectors, the width of the nearly perfect semicircle corresponds to the surface reaction resistance, and the phase shift in the Bode-Bode plot (b) corresponds to the combined effect of chemical and interfacial capacitances. The solid symbols in the Nyquist plot shows the impedance at $f = 0.19$ Hz.

from 195 to 2241 nm) symmetric cells were characterized using impedance spectroscopy. To satisfy the dilute limit assumption as well as to minimize chemical expansion of SDC15 upon reduction, oxygen nonstoichiometry (δ) was kept below 0.014 during the experiment (corresponding to a chemical expansion ~ 0.1 %).[57] A porous electrode with relatively small feature sizes ($2W_1 \sim 3$ μm and $2W_2 \sim 5$ μm) was utilized to suppress in-plane electron diffusion-drift resistance. Under all experimental conditions, the impedance response, presented in a Nyquist plot (Figure 4.10), appeared as a large, nearly perfect, half circle displaced from the origin along the real axis by an amount that corresponds precisely to that expected for the area-normalized resistance of the YSZ single crystal substrate. Such impedance spectra are consistent with a surface-limited transport process (Section 4.3.1) where a semi-circle, rather than a tear-drop shape, impedance spectrum is expected. As a result, the equivalent circuit presented in Figure 4.9 is used to analyze the transport properties, specifically, the various capacitances in the

system.

Since only one arc is present in the Nyquist plot, one resistive process dominates (other than the bulk YSZ response – which does not manifest in an arc because extremely low dielectric capacitance of the substrate is beyond the frequency limit of the instrument). Based on the physically-derived equivalent circuit, there are two possible processes: the surface reaction at the MIEC | gas interface and ion transfer at the MIEC | IC interface. Because the former interface is directly exposed to the gas, the resistance is expected to scale with hydrogen and water vapor pressure. On the other hand, at a solid-solid interface, where both materials conduct strictly oxygen ions and electrons, the resistance should be a strict function of oxygen partial pressure (with $p_{O_2} \propto p_{H_2}^{-2} p_{H_2O}^{2}$). Analysis of the experimentally-measured resistance reveals that the process exhibited a $p_{H_2}^{0.5}$ and $p_{H_2O}^{0.5}$ dependence. The absence of the counter-dependence on hydrogen and water vapor pressure confirms that the resistance is p_{O_2}-independent and can be assigned to the surface reaction. Accordingly, the MIEC | IC ion transfer resistance ($\tilde{R}_{ion}^{MIEC-IC}$) is taken to be zero. As consequence of treating such interface as reversible, the accompanying electrochemical double-layer capacitance must also be zero. Moreover, the three remaining capacitors are now directly connected in parallel and can be represented as a single capacitor with a combined capacitance of $C_{tot} = \frac{1}{2}\left(C_{chem} + C_{ion,2PB}^{gas} + C_{ion,3PB}^{gas}\right)$, where a factor of ½ accounts for the presence of the two thin films on both sides of the substrate. The dielectric capacitance ($\sim 10^{-7}$ F cm^{-2} for a 200 nm thick SDC15 film) is more than 4 orders of magnitude smaller than the lowest observed capacitance, and is safely neglected.

The constant phase element (CPE) used to represent C_{tot} showed a relatively large exponent parameter, exceeding 0.93 for all conditions examined, indicating a relatively small

dispersion in the relaxation frequency of the system. Volume-specific capacitance (C_{tot}/AL) was

obtained as a function of p_{O_2} at temperatures between 500 and 650 °C for all of the films (Figure

4.11). For the thickest film examined (2241 nm, average thickness of films on both sides), the

isothermal capacitance is proportional to $p_{O_2}^{-1/4}$, which is expected if the capacitance is indeed

dominated by the chemical capacitance (as implied by Eqs. (4.37) & (1.20)). However, as the

film thickness decreases, the isothermal capacitance curves deviate strongly from the $p_{O_2}^{-1/4}$

dependence, approaching a constant at higher p_{O_2} and lower temperatures. The dependence of

the volume-specific capacitance on film thickness implies that contributions other than chemical

capacitance are indeed present in our system. Given that the volume-specific chemical

capacitance depends only on the electron carrier concentration (or equivalently, oxygen

nonstoichiometry), the total capacitance can be expressed as:

$$C_{tot} = \frac{e^2 A}{k_B T} c_{eon}(p_{O_2}^{*eq},T) \times L + C_{int}(p_{O_2}^{*eq},T) \tag{4.38}$$
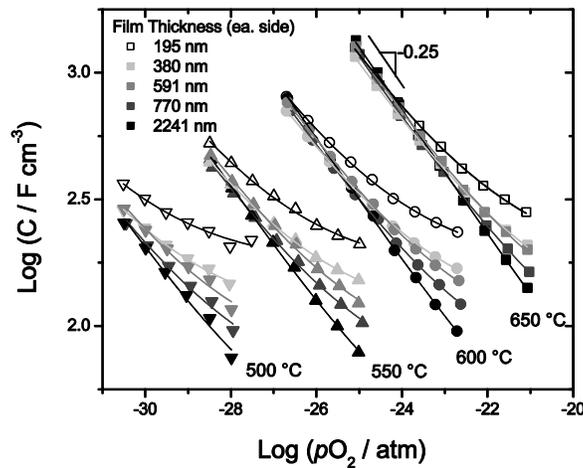
Figure 4.11: Dependence of the volume-specific capacitance on oxygen partial pressure for films of varying thickness and at various temperatures, as indicated. Symbols are the measured values and the solid lines are the best fit to Eq.(4.38). As the film thickness decreases, deviation from $p_{O_2}^{-1/4}$ dependence increases.

where $C_{int} = C_{ion,2PB}^{gas} + C_{ion,3PB}^{gas}$ is the sum of interfacial capacitances and it is implicitly assumed

that the Gibbs free energy of carrier formation is independent of film thickness, consistent with

the low residual stress of these relatively thick films. Figure 4.12(a) shows the capacitance

plotted as function of film thickness and fit to Eq. (4.38). Varying the film thickness while

holding the cell area constant permits the extraction of the thickness-dependent chemical

capacitance and the thickness-independent interfacial capacitances. The electron carrier

concentration and the oxygen nonstoichiometry computed from the chemical capacitance values

exhibit excellent agreement with the expected $p_{O_2}^{-1/4}$ dependence Figure 4.12(b). Furthermore, the

interfacial capacitances obtained from this analysis (Figure 4.13(a)) display a very weak p_{O_2}

(a)   (b)
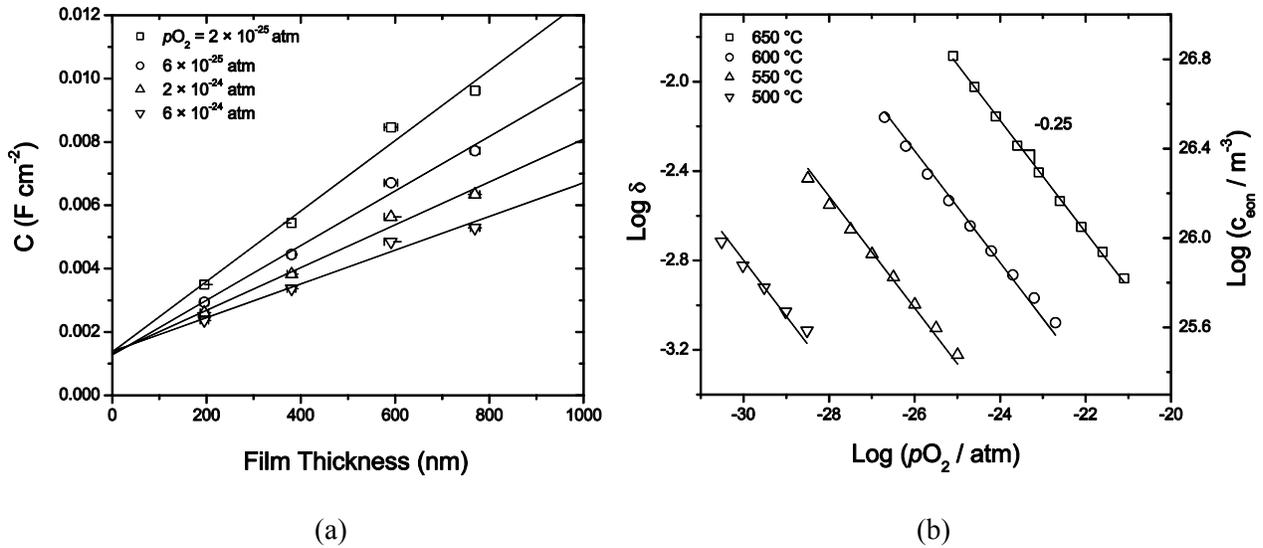
Figure 4.12: (a) Capacitance measured at 600 °C (various oxygen partial pressures) as a function of SDC15 film thickness. The solid lines are the best fit to Eq.(4.38). The slope gives the thickness-independent chemical capacitance while the intercept gives the sum of interfacial capacitances. **(b)** Oxygen nonstoichiometry (δ) and electron carrier concentration (c_{eon}) determined using the film thickness-dependent capacitance data (partially shown in (a)).
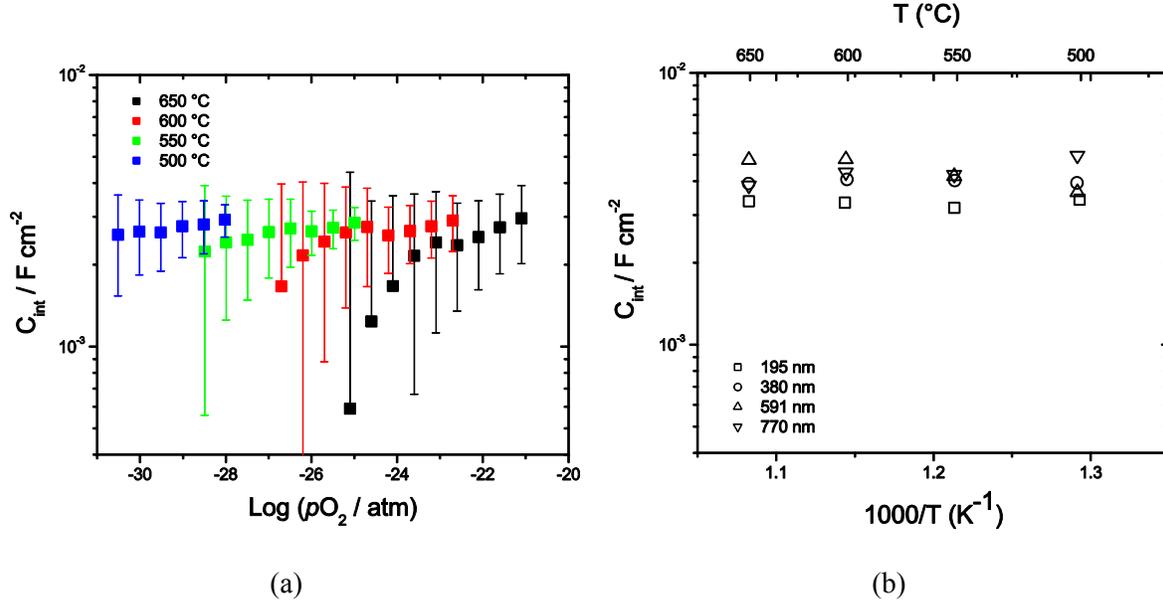
Figure 4.13: Interfacial capacitance extracted by **(a)** assuming that the interfacial capacitance is independent of oxygen partial pressure. (*i.e.* Eq. (4.39)), and **(b)** subtracting thickness-dependent chemical capacitance (*i.e.* Eq. (4.38)).

dependence and nearly no temperature dependence.

Having demonstrated the $p_{O_2}^{-\frac{1}{4}}$ dependence of C_{chem} and the relatively p_{O_2}-independent C_{int}, each isothermal capacitance data set in Figure 4.11 can be described according to the following approximation :

$$C_{tot} = \frac{e^2 AL}{k_B T} \sqrt{\frac{2}{\left(c_{dop}^{*eq}\right)}} \exp\left(\frac{\Delta G_O^0}{2 k_B T}\right) \left(p_{O_2}^{*eq}\right)^{-\frac{1}{4}} + C_{int}(T) \tag{4.39}$$

where Eq. (1.20) is utilized to specify $c_{eon}(p_{O_2}^{*eq}, T)$. In contrast to the analysis associated with Eq. (4.38) for which multiple films of differing thicknesses are used to deconvolute capacitance terms, application of Eq. (4.39) requires only the capacitance of one sample measured under

Table 4.2: Comparison of standard enthalpies (ΔH_{oxd}) and entropies (ΔS_{oxd}) for the oxidation reaction $\tfrac{1}{\delta}CeO_{2-\delta} + \tfrac{1}{2}O_2(g) \rightarrow \tfrac{1}{\delta}CeO_2$ (implying $Ce^{3+} \rightarrow Ce^{4+}$), on a per mole atomic oxygen basis, obtained in thin film and bulk materials. Electron carrier formation enthalpy is given by $-\Delta H_{oxd}/2$. Number after "SDC" indicates doping level (%).

	$-\Delta H_{oxd}(eV)$	$-\Delta S_{oxd}$ $(10^{-3}\ eV\ K^{-1})$	*Measurement Method*	**Ref**
SDC15(100) 195 nm	4.16 ± 0.02	1.13 ± 0.03	Thin Film Impedance	This Work
SDC15(100) 380 nm	4.17 ± 0.03	1.15 ± 0.03	Thin Film Impedance	This Work
SDC15(100) 591 nm	4.18 ± 0.04	1.18 ± 0.04	Thin Film Impedance	This Work
SDC15(100) 770 nm	4.18 ± 0.04	1.18 ± 0.04	Thin Film Impedance	This Work
SDC15(100) 2241 nm	4.18 ± 0.02	1.19 ± 0.03	Thin Film Impedance	This Work
SDC15(110) 2124 nm	4.19 ± 0.06	1.20 ± 0.07	Thin Film Impedance	This Work
SDC15(111) 2124 nm	4.18 ± 0.05	1.22 ± 0.06	Thin Film Impedance	This Work
SDC15 (polycrystalline)	4.18 ± 0.05	1.18 ± 0.05	Bulk Impedance	[2]
SDC10 (polycrystalline)	4.15	1.10	Thermogravimetry	[3]
SDC20 (polycrystalline)	3.99	1.13	Thermogravimetry	[3]

several oxygen partial pressures. Utilizing ΔG_O^0 obtained from Eq. (4.39) at multiple temperatures, the $Ce^{3+} \rightarrow Ce^{4+}$ standard oxidation enthalpy and entropy (related to the energy of electronic carrier formation) is computed for each of the films. The thermodynamic quantities (Table 4.2) are not only essentially independent of film thickness and orientation, but also identical, within experimental error, to the values measured for bulk materials. The agreement demonstrates that the chemical capacitance has been correctly extracted from the total capacitance, and that impedance spectroscopy, under ideal conditions, can be utilized to determine carrier concentrations and thermodynamic quantities even in thin films. The results further imply that SDC15 films are essentially bulk-like in nature, with low strain energy, consistent with the thickness independent lattice constant, and minimal influence of low-angle tilt boundaries present in the growth direction, consistent with the narrow FWHM measured in

the rocking curve diffraction experiment. In contrast, in very thin films, 10 nm or less,[111] and in nanostructured bulk materials[112] large decreases in reduction enthalpy have been reported, indicating that size and strain effects can, under different circumstances, induce substantial deviations in chemical bonding state.

Turning to the interfacial capacitance, the independence of this term (with a magnitude of $\sim 4 \times 10^{-3}$ F cm^{-2}) to both temperature and oxygen partial pressure (Figure 4.13) points to an origin that is connected to the bulk vacancy concentration, a quantity set by the extrinsic dopant concentration and hence fixed throughout the parameter space of the experiments. Even under much more oxidizing atmospheres ($p_{O_2} = 0.21$ atm, $T = 650$ °C), the interfacial capacitance was found to be relatively unchanged, at $\sim 2 \times 10^{-3}$ F cm^{-2}. An alternative interpretation, such as an origin due to electronic effects at the is MIEC | IC interface, is deemed unlikely as such effects would be expected to depend on the electron carrier concentration, a quantity that clearly has a strong temperature and oxygen partial pressure dependence. Similarly, a pseudocapacitance associated with diffusion or adsorption processes at the MIEC | gas interface is unlikely as such effects would also be expected to depend strongly on environmental conditions. A remaining possibility is that that the interfacial capacitance is due to a change in oxygen vacancy carrier concentration near the surface in response to the electrochemical perturbation, with the screening length given by the Debye length. The theoretical double-layer capacitance, assuming the interface is flat and reversible to electrons, can be determined by[66]

$$C_{ion,2PB}^{gas} \approx \sqrt{\frac{4\varepsilon\varepsilon_0 e^2 c_{ion}}{k_B T}} \approx 3 \times 10^{-4} \text{ F cm}^{-2} \tag{4.40}$$

where, as a first approximation, ε and c_{ion} are taken to be the same as in the bulk. The capacitance is similar to that measured experimentally ($\sim 4 \times 10^{-3}$ F cm^{-2}) and does not depend

strongly on temperature (500 to 650 °C) nor oxygen partial pressure.

4.5 Active Reaction Sites in Metal-Ceria Composite Systems

The role of metal 3PB on electrochemical reactions in metal-ceria composite system was explored in Section 3.6 using bulk-processed samples. As noted, however, the lack of control over the current collector microstructure complicated analysis. Inherently, the smooth surface of thin films grown on polished single crystal substrates is compatible with microfabrication. Thin films of SDC20 with lithographically-defined 2PB and 3PB site densities were characterized by impedance spectroscopy.

To ascertain the relative contributions of the ceria | metal | gas 3PB sites, the ceria | gas 2PB sites, and in-plane electron diffusion-drift, current collector dimensions W_1 and W_2 as well as the metal type (Pt, Ni) were varied. Because 3PB density ($d_{3PB} = (W_1 + W_2)^{-1}$, unit m^{-1}), 2PB density ($d_{2PB} = W_2/(W_1 + W_2)$, unitless), and electron diffusion length (W_2) are not independent quantities, it is not possible to vary each parameter individually. In the first sequence of samples, $W_1 + W_2$ was fixed at 80 μm (*i.e.* fixed 3PB site density), while W_1 was varied between 5 and 75 μm (Table 4.1). In the second sequence of samples, $W_2/(W_1 + W_2)$ was fixed at 0.5 (half of the SDC20 surface open to the gas phase and the other half covered by the metal patterns, *i.e.* fixed 2PB site density), while $W_1 + W_2$ was varied between 5 and 80 μm. Impedance spectra were recorded for each sample at temperatures between 600 and 650 °C and under various H$_2$-H$_2$O-Ar atmospheres. Relative errors in the electrode resistance, mainly from run-to-run variation during fabrication, were determined by measuring four identical samples.
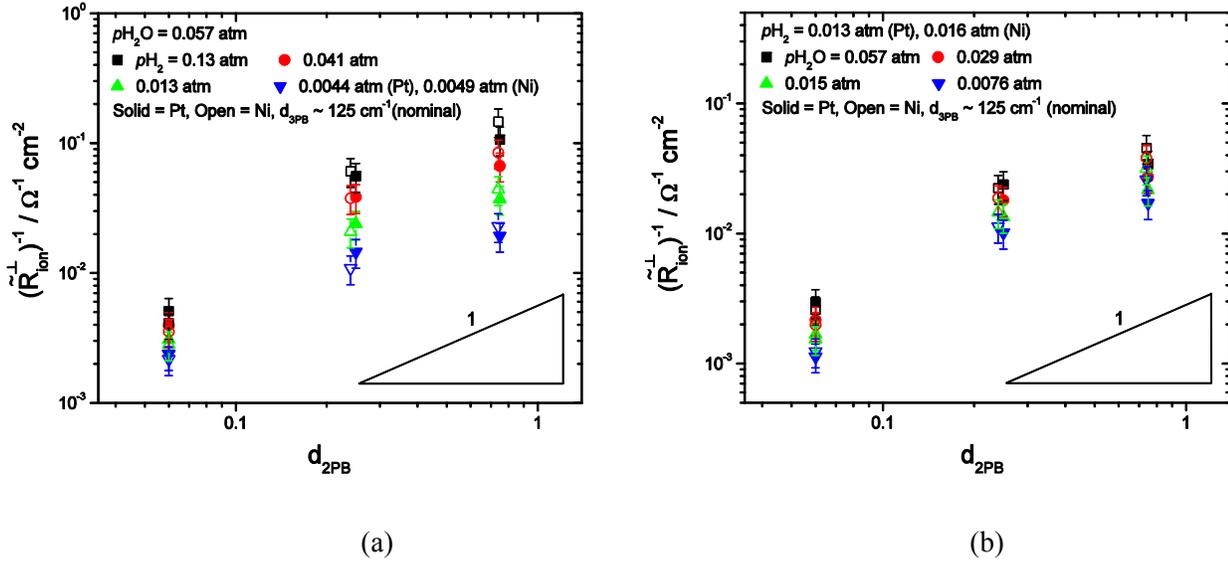
Figure 4.14: Inverse electrode resistance for SDC20 as a function of metal | ceria 2PB density with metal | ceria | gas 3PB density fixed (125 cm^{-1} nominal). **(a)** As a function of hydrogen pressure and **(b)** water vapor pressure. Slope of 1 in the log-log plot confirms that contributions from intentional and unintentional 3PB (due to cracks and holes in the metal film) are negligible.

For samples with fixed 3PB site density, varying the 2PB density allows the activity of the latter to be determined through linear fitting. Under the assumption the diffusion resistance is negligible, the overall area-normalized reaction rate given by:

$$r = d_{2PB}k_{ion,2PB}^{gas} + d_{3PB}k_{ion,3PB}^{gas} = W_2/(W_1 + W_2)k_{ion,2PB}^{gas} + (W_1 + W_2)^{-1}k_{ion,3PB}^{gas} \qquad (4.41)$$

In the $\log r$ vs. $\log d_{2PB}$ representation, a slope of 1 would indicate that reactions occur entirely at the MIEC | gas 2PB (*i.e.* $d_{2PB}k_{ion,2PB}^{gas} \gg d_{3PB}k_{ion,3PB}^{gas}$), whereas a slope of 0 would indicate that the reactions either occur entirely over the 3PB. Experimentally, average slopes of 1.0 ± 0.3 and 1.2 ± 0.3 were obtained for the Pt and Ni metal patterns in the log-log plot (Figure 4.14),
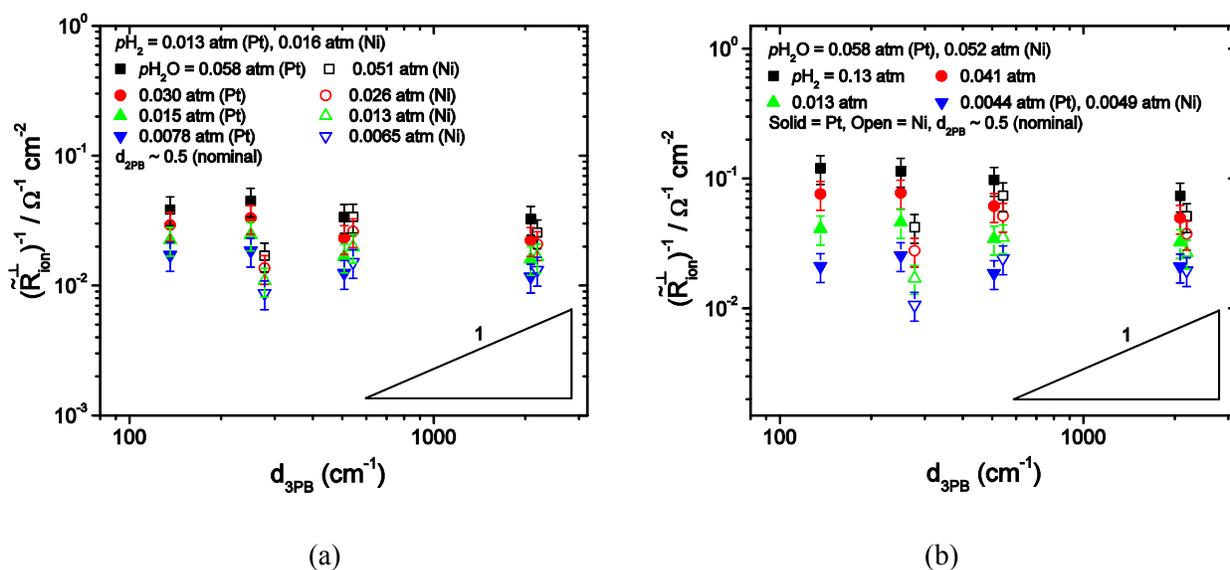
Figure 4.15: Inverse electrode resistance for SDC20 as a function of metal | ceria | gas 3PB density with metal | ceria 2PB density fixed at 0.5. **(a)** As a function of hydrogen pressure and **(b)** water vapor pressure.

confirming that at the relatively low 3PB:2PB relative site density utilized (a nominal value of 125 cm^{-1}) the reactions are occurring preferentially over the 2PB.

The above results can also be used to assess the quality of the current collector, specifically the density of unintended 3PB due to coarsening of the metal patterns under the relatively high experimental temperatures (a maximum of 650 °C). Two contributions are expected: (1) roughening of the metal pattern borders, and (2) formation of holes in the supposedly dense regions of the metal patterns. Since the theoretical 3PB is held constant, roughening of the patterns shift would simply increase the reaction site density equally for all samples. If sufficiently severe, the slope in the log-log plot (Figure 4.14) will shift towards zero. On the other hand, formation of holes in the metal stripes is expected to be proportional to the

metal area (which ranges from 0.40 to 0.96, including the border of the current collector with no intentional 3PBs) and will affect samples with larger metal stripe areas more severely. Under the extreme limit where the electrochemical current injected at the 3PBs created due to the holes in the metal pattern dominates, slope in the log-log plot will turn negative. Because a slope of close to 1 was observed in Figure 4.14, it can be concluded that unintentional hole formation on the metal patterns did not contribute to the measured reaction rates significantly. This is also consistent with morphological examination of tested samples with SEM, Section 4.2.

Next, the sample sequence with fixed 2PB site density was examined with the goal of assessing the relative activity of the 3PB to the 2PB sites. The 3PB site density values spans a wide range ($d_{3PB} : d_{2PB}$ ranging from 140 to 4,000 cm^{-1}), with the upper bound value comparable to a typical metal-(metal oxide) composite electrode (with $d_{3PB} : d_{2PB}$ typically on the order of 20,000 cm^{-1}. Here, in the $\log(\tilde{R}_{ion}^{\perp})^{-1}$ vs. $\log d_{3PB}$ representation (*i.e.* slope in Figure 4.15), a slope of 1 would indicate that reactions either occur entirely at the MIEC | gas 3PB or are limited by in-plane electron diffusion, whereas a slope of 0 would indicate that reactions occur entirely over the 2PB (Eq. (4.41)). Under the wide range of conditions examined, the slope is close to zero for both Pt and Ni on SDC20, indicating that the current injected at the 3PB is low.

It should be noted that the trend of inverse electrode resistance increasing with 3PB site density can also be explained by increased diffusion length (recall that in this series of sample $W_1 + W_2$, the length in which electrons migrate, was varied). The shape of the impedance spectra as well as the magnitude of the electrode resistance will be discussed to assess the extent in which diffusion contributes to the measured data. According to calculated impedance spectra in Section 4.3, for reaction that is surface-limited, the spectra adopts a semi-circle shape; for

reaction that is limited by diffusion, the spectra adopts a tear-drop shape. For a system in the transition between the surface- and diffusion-limited regimes, a straight-line with a slope of 45 ° is visible in the high-frequency portions of the Nyquist plot (Figure 4.8). Experimentally, for all samples examined, the impedance spectra consist of nearly perfect semi-circles, strongly suggesting that the electrodes are limited by surface reactions rather than diffusions. Furthermore, taking the electronic conductivity in SDC20 films to be the same as the values measured in bulk samples (Section 3.4), diffusion contribution to the measured resistance was calculated. In the worst-case scenario (long diffusion length and low electronic conductivity), diffusion contribution to the total electrode resistance is expected to be at most 5.8 %. Thus, in-plane electron diffusion cannot account for the observed dependence of resistance on the 3PB density.

Based on the experimental results for thin film ceria and metallic current collectors with well-defined geometry, it can be concluded that, under all conditions examined, the activity of Pt and Ni 3PBs are negligible compared to that of SDC20 2PBs toward hydrogen electrochemical oxidation and hydrolysis near open-circuit conditions.

Chapter 5
Non-electrochemical Gas-Solid Catalysis in Ceria

5.1 Summary

In ceria-based oxides, a change in the valence state of Ce is charge balanced a change in oxygen stoichiometry. As shown in Chapters 3 & 4, the variation of oxygen content in ceria enables ceria to act as an oxygen reservoir and is the basis for numerous catalytic and electro-catalytic reactions. In this Chapter, the oxygen nonstoichiometry in ceria is cycled thermochemically and is coupled with the decomposition of H_2O and/or CO_2 to produce H_2, CO, hydrocarbons, and O_2. The thermodynamics and kinetics of fuel and oxygen generation were investigated. Thermally-driven oxygen evolution was characterized by temperature-programmed reduction, and fuel evolution by quantification of gaseous and solid products. By numerical analysis of reaction rates, ambipolar diffusion of neutral oxygen in ceria was found to be the rate-limiting step in both oxygen and fuel evolution reactions. Furthermore, a high selectivity towards CO during oxidation of ceria by CO_2 was observed and is attributed to the unfavorable energetics of carbon formation on the surface of ceria. Finally, thermochemical cycling was demonstrated as an effective method for solar H_2O- and CO_2-splitting using a custom-designed solar reactor, with a solar-to-fuel efficiency approaching 1 %.

5.2 Thermodynamics of Ceria Reduction and Oxidation for Fuel Production

In a thermochemical fuel production cycle, a metal oxide is cycled between two temperatures (T_H and T_L) and two gas atmospheres (typically inert during ceria reduction and H_2O and/or CO_2 during ceria oxidation). In this section, the thermodynamics of ceria reduction and oxidation are examined. In the case of undoped ceria, direct measurements of the oxygen nonstoichiometry have been carried out over a wide range of conditions,[1] including those relevant for thermochemical fuel production, Figure 5.1. Where such extensive measurements have not been carried out, the high temperature behavior can be approximated from an extrapolation of properties measured at more accessible conditions. For the specific case of SDC15, the experimentally determined standard enthalpy and entropy of the oxidation reaction are -4.18 ± 0.05 eV and -1.15 ± 0.05 meV K^{-1}, respectively,[2,59] and the dilute defect model has been shown to apply for δ up to 0.04.[50] Using these values and Eq. (1.16) & (1.18), the computed
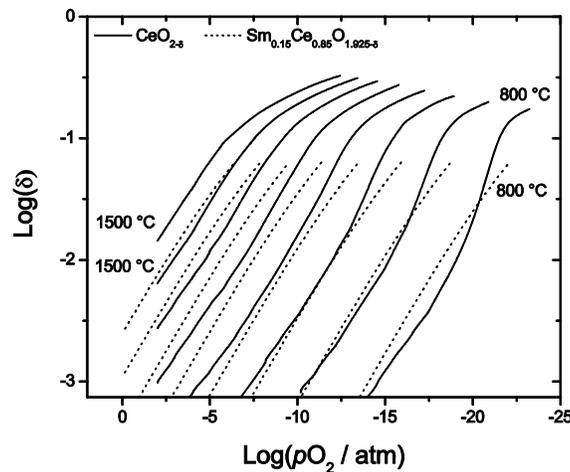
Figure 5.1: Solid lines: Oxygen nonstoichiometry, δ, in $CeO_{2-\delta}$ measured at 100 °C intervals using thermogravimetry. After Panlener *et al.*[1]. **Dotted lines:** High-temperature oxygen nonstoichiometry in $Sm_{0.15}Ce_{0.85}O_{1.925-\delta}$, estimated by extrapolation, under the assumption of ideal solution behavior, from data collected from 500 to 650 °C.

nonstoichiometry in SDC15 varies as shown in Figure 5.1. From the two sets of data provided in Figure 5.1, it is evident that, at T_H = 1,500 °C under inert gas with an oxygen partial pressure of 10^{-5} atm, a nonstoichiometry in the range of δ = 0.03 - 0.05 is expected for SDC15 (accounting for the uncertainty in the enthalpy and entropy values), compared to the measured value of 0.06 for undoped ceria. In turn, these δ values are equivalent to the release in the reduction half-cycle at T_H of 2 to 3 mL O_2 per gram of fully oxidized SDC15 and to 4 mL O_2 per gram of fully oxidized CeO_2 (hereafter simply mL g^{-1}, irrespective of doping).

Turning to the fuel production half-cycle at T_L (ceria oxidation), and the particular case of hydrogen production, the overall reaction can be expressed as the sum of the ceria oxidation reaction and the steam dissociation reaction:

$$\tfrac{1}{2}O_2(g) + 2Ce_{Ce}' + V_O^{\bullet\bullet} \rightarrow 2Ce_{Ce}^x + O_O^x \tag{5.1}$$

$$+ \qquad H_2O(g) \rightarrow H_2(g) + \tfrac{1}{2}O_2(g) \tag{5.2}$$

$$\overline{H_2O(g) + 2Ce_{Ce}' + V_O^{\bullet\bullet} \rightarrow H_2(g) + 2Ce_{Ce}^x + O_O^x} \tag{5.3}$$
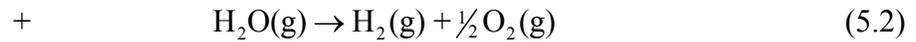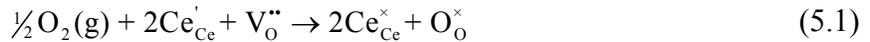
If the reaction is carried out with excess steam, thermodynamics predicts the complete reoxidation of the reduced ceria, and the quantity of fuel produced will be exactly equal, within a stoichiometric factor, to the nonstoichiometry achieved at T_H. However, operation of the system with excess steam implies tremendous energy penalties as excess quantities of gas must be heated and cooled in each cycle. A more realistic scenario is one in which the quantity of gas phase reactant is fixed at some value that appropriately balances the available oxygen nonstoichiometry. The quantity of fuel produced in this scenario depends not only on the oxygen nonstoichiometry attained at T_H, but also on the relative reducing potential of the ceria, and can

be computed, much as in the case of the reduction half-cycle at T_H, from a knowledge of the thermodynamic parameters.

The equilibrium constant for the overall reaction of reduced ceria with steam, K_{TL}, is simply given as $K_{oxd}K_{WS}$, where K_{WS} is the equilibrium constant for steam dissociation (*i.e.* reaction (5.2)) and K_{oxd} is as given in Eq. (1.18). Taking the system comprised of reduced ceria plus steam to be closed and hence to obey mass conservation, one finds

$$K_{TL} = K_W K_{oxd}(T_L) = \frac{(1-x-2\delta_f)^2(1-\frac{x}{4}-\frac{\delta_f}{2})}{4\delta_f^{\ 2}(\frac{x}{4}+\frac{\delta_f}{2})} \frac{\alpha}{(n_{H_2O,i}-\alpha)} \tag{5.4}$$

where $\delta_f = \delta_i - \alpha / n_{CeO_y}$, δ_i is the initial nonstoichiometry attained in the high temperature reduction step, x is the doping amount, n_{CeO_y} is the number of moles of ceria, $n_{H_2O,i}$ is the initial number of moles of water, and α as the extent of reaction in moles. Solving for α yields the amount of hydrogen produced at equilibrium. Gaseous oxygen, which is assumed to take on a very low concentration during fuel production, is excluded here from the mass balance for computational simplicity. If the defect model and hence K_{oxd} are not well-known, one can alternatively predict the equilibrium fuel productivity from knowledge of the partial molar free energy of lattice oxygen, ΔG_O, as a function of temperature and nonstoichiometry according to the relationship:

$$\Delta G_O(T_L, \delta = \delta_i - \alpha / n_{CeO_y}) = RT_L \ln\left(\frac{K_W(n_{H_2O,i}-\alpha)}{\alpha}\right) \tag{5.5}$$

In the case where the input reactant is CO_2 (rather than H_2O), an expression analogous to Eq. (5.4) or (5.5) can be obtained. Here one begins with the reduction of CO_2, where both CO

and C(graphite) are considered as possible products through the reactions

$$CO_2(g) \rightarrow CO(g) + \tfrac{1}{2}O_2(g) \tag{5.6}$$

$$CO_2(g) \rightarrow C(graphite) + O_2(g) \tag{5.7}$$

Again, the extent of reaction yields the equilibrium quantity of CO and/or C produced. Taking the process one step further, one can consider the simultaneous dissociation of CO_2 and H_2O to yield methane as a product through the reaction

$$2H_2O(g) + CO_2(g) \rightarrow CH_4(g) + 2O_2(g) \tag{5.8}$$

where the water-gas-shift equilibrium is taken into account implicitly.

With this formalism the equilibrium gas phase compositions were computed for $\delta_i = 0.05$ and (i) $n_{H_2O,i} = \delta_i n_{CeO_y}$ (ii) $n_{CO_2,i} = \tfrac{1}{2}\delta_i n_{CeO_y}$, and (iii) $n_{H_2O,i} = 2n_{CO_2,i} = \tfrac{1}{2}\delta_i n_{CeO_y}$ for SDC15. While the quantity of reactant supplied under this set of conditions is stoichiometrically sufficient for full reoxidation of the ceria, thermodynamic considerations indicate that the reoxidation will not proceed to completion and instead the ceria will attain, upon system equilibration, a non-zero nonstoichiometry, δ_f. The fuel production capacity in the oxidation half-cycle is given in such a case not by the initial nonstoichiometry achieved at high temperature, δ_i, but by the change in oxygen nonstoichiometry

$$\Delta\delta = \delta_i - \delta_f \tag{5.9}$$

Each mole of stoichiometry change in bulk oxygen content corresponds to either 1 mole of H_2, 1 mole of CO, 0.5 mole of C(graphite) or 0.25 mole of CH_4 produced. The results of the computation, Figure 5.2, show that the amount of fuel produced increases as T_L is lowered,

consistent with the greater driving force for ceria oxidation at lower temperatures relative to hydrogen or carbon oxidation.
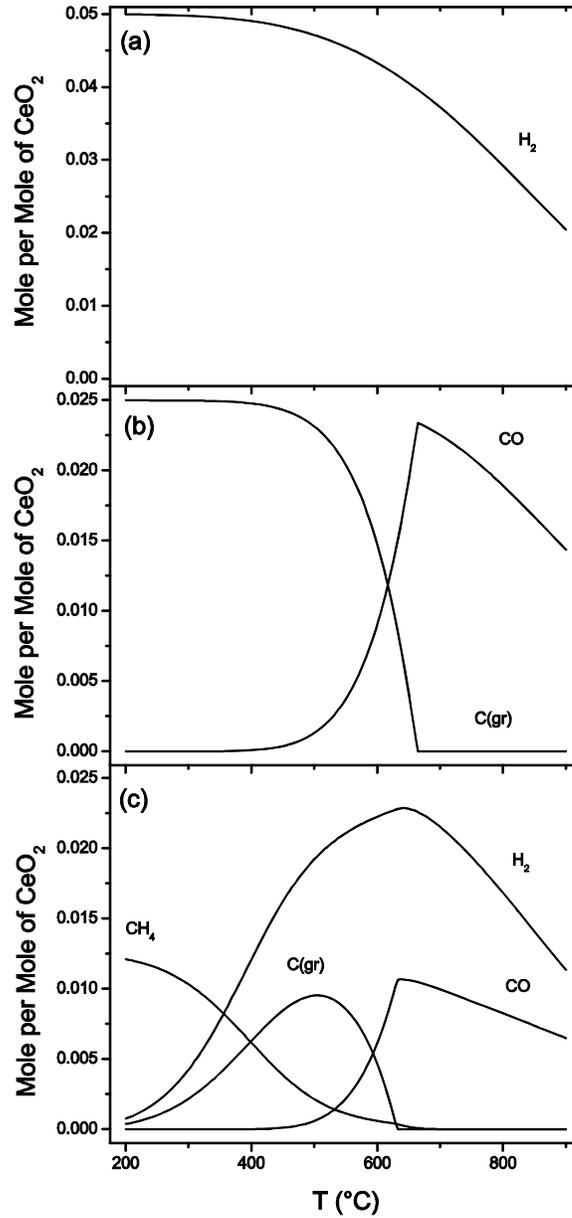
Figure 5.2: Equilibrium compositions for the fuel production half-cycle over SDC15 calculated at 1 atm for **(a)** $n_{H_2O,i} = \delta_i n_{CeO_y}$ **(b)** $n_{CO_2,i} = \frac{1}{2}\delta_i n_{CeO_y}$, and **(c)** $n_{H_2O,i} = 2n_{CO_2,i} = \frac{1}{2}\delta_i n_{CeO_y}$ where the initial oxygen nonstoichiometry, δ_i, is taken to be 0.05. Initial $p_{H_2O} = 0.064$ atm and $p_{CO_2} = 0.032$ atm.
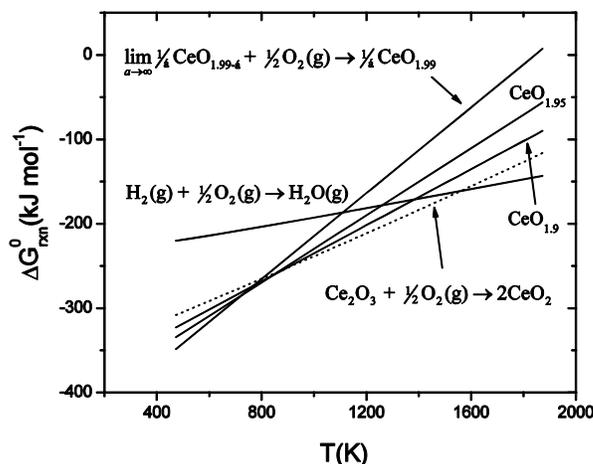
Figure 5.3: Comparison of the Gibbs free energy of the hydrogen oxidation reaction (with the gas species at 1 atm) and that of CeO_2 oxidation (with the oxygen partial pressure at 1 atm and the oxygen nonstoichiometry at the indicated values).

An arguably more common method for assessing the thermodynamic suitability of a potential thermochemical reaction medium is through a direct consideration of the ΔG_{oxd} in comparison to the ΔG_{rxn} for hydrogen oxidation (or equivalently, water-splitting), Figure 5.3, for standard state conditions ($p_{\text{gas}} = 1$ atm). A subtlety arises here in that the initial and final δ values in the calculation of ΔG_{oxd} of ceria are inherently arbitrary. For simplicity, the reaction is considered in the limit in which the nonstoichiometry change is infinitesimal (as in the case of Eq. (1.9)), and several selected values of δ are considered. The data are also compared to the stoichiometric reaction $Ce_2O_3 + \frac{1}{2}O_2(g) \rightarrow CeO_2$, which has no contribution from defect configurational entropy). The figure reveals graphically the thermodynamic underpinnings of the thermochemical reaction approach. In general, where ΔG_{oxd} of ceria lies below that of ΔG_{rxn}^0 of hydrogen oxidation, *i.e.* at low temperatures, the ceria has sufficient reducing power that it will induce dissociation of steam as the ceria becomes oxidized. At high temperatures, the reducing

power of ceria decreases, as indicated by the decrease in magnitude of ΔG_{oxd}, and where ΔG_{oxd} becomes positive, ceria releases oxygen (under 1 atm p_{O_2}). The clear dependence of ΔG_{oxd} on δ results from the dependence of both the cerium-oxygen bond enthalpy and the configurational entropy on defect concentrations. As evident from Figure 5.3, the dependence is such that at a given temperature, T_H, it is increasingly more difficult to liberate additional oxygen from ceria (ΔG_{oxd} becomes increasingly more negative with increasing δ). Similarly, at a given T_L, it is increasingly more difficult to reoxidize ceria because the difference $\Delta G_{oxd} - \Delta G_{rxn}$ becomes less negative with decreasing δ. These considerations thus reveal subtle differences in the manner which the redox thermodynamics of nonstoichiometric compounds and stoichiometric reactions apply to thermochemical reactions.

5.3 Thermally-driven Reduction and Oxidation of Ceria by H₂O

To evaluate the thermodynamics and kinetics of fuel production, $CeO_{2-\delta}$ was thermochemically cycled using a rapid heating, infrared-furnace-based reactor system described in Section 2.2.3. The results, Figure 5.4, indicate that ceria is remarkably well suited as a thermochemical reaction medium. On aggressive heating (1,000 °C min^{-1}) to 1,500 °C under inert atmosphere (p_{O_2} = 10^{-5} atm), an almost immediate release of oxygen is observed (Figure 5.4 (a)). The total quantity of oxygen detected by a mass spectrometer, 4.3 ± 0.3 mL g^{-1}, corresponding to a δ of 0.066 ± 0.005, is within error of the value of 4 mL g^{-1} determined via thermogravimetry.[1] An identical oxygen release amount, within experimental error, was obtained for lower ramp rates (*e.g.* 100 °C min^{-1}). Moreover, the oxygen release reaches 70 % completion within 5.0 min of the initiation of the heating and largely keeps pace with the rate of temperature
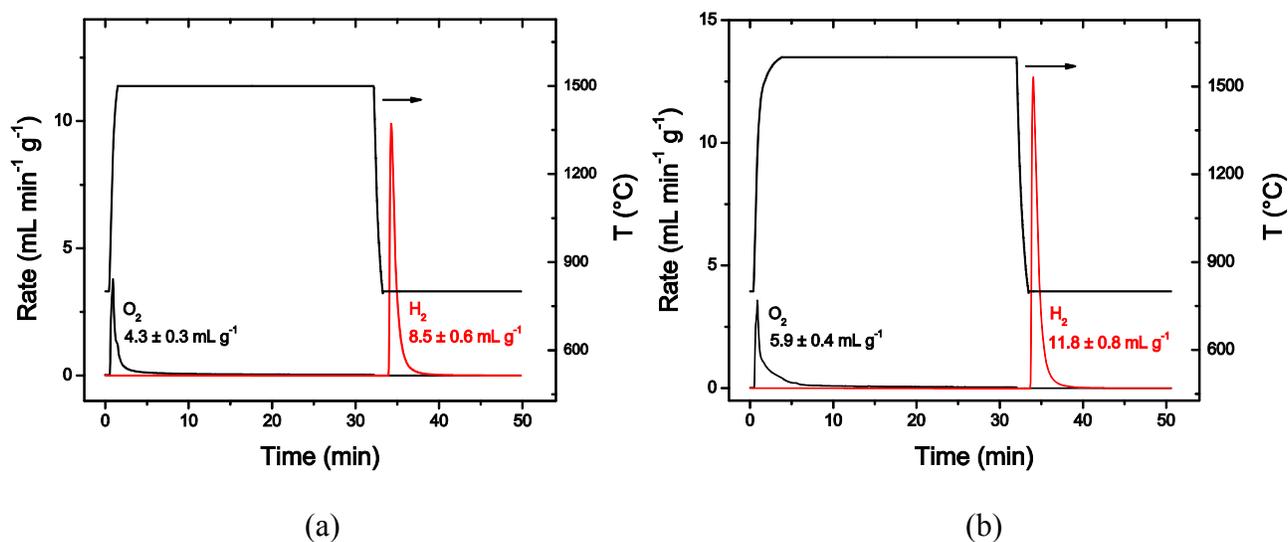
Figure 5.4: Thermochemical cycling behavior of CeO_2 (high temperature oxygen release and lower temperature water dissociation) as measured by mass spectrometry at an oxygen release temperature of **(a)** 1,500 °C and **(b)** 1,600 °C and a water dissociation temperature of 800 °C. The integrated oxygen and hydrogen productivities are indicated. The oxygen partial pressure during the oxygen release half-cycle is 10^{-5} atm and the total gas flow rate (FR_{tot}) is 1,000 mL min^{-1}. The water partial pressure during the hydrogen release step is between 0.25 and 0.27 atm and FR_{tot} between 267 and 274 mL min^{-1}.

rise throughout heating. Upon lowering the temperature to 800 °C and introducing steam (p_{H_2O} = 0.25 - 0.27 atm) rapid hydrogen production is observed with 90 % of the fuel produced within 1.8 min of initiation. Furthermore, the total amount of hydrogen produced, 8.5 ± 0.6 mL g^{-1}, implies complete reoxidation of the reduced ceria and hence full utilization of the available nonstoichiometry. Together, these values correspond to an average hydrogen production rate of 4.6 mL min^{-1} g^{-1} (instantaneous reaction rate averaged over the time required to reach 90 % of the extent of reaction).

Raising the temperature of the oxygen release step is expected, on thermodynamic grounds, to increase the extent of oxygen nonstoichiometry, Figure 5.1, and indeed experimentally such behavior is observed, Figure 5.4(b). Ceria reduction at 1,600 °C increases

oxygen release from 3.4 to 5.9 ± 0.4 mL g^{-1}, or to $\delta = 0.091 \pm 0.006$. After cooling and steam injection at 800 °C, the entirety of the structural nonstoichiometry is again utilized in the fuel production step, with 11.8 ± 0.8 mL g^{-1} now produced. The rate 6.2 mL min^{-1} g^{-1}, is higher than that for the less reduced material, possibly as a result of increased surface vacancy concentrations leading to higher reaction rates.

For the production of fuel via thermochemical cycling, oxygen release as well as fuel production segments of the cycle require both heterogeneous surface reaction on ceria and oxygen bulk diffusion in ceria to occur in series. In principle, either or both reaction steps may be rate-limiting. The time scale for the bulk diffusion of oxygen can be estimated from knowledge of the ambipolar diffusion coefficient (Section 1.3.2). Taking the dilute solution approximation for ceria, it follows from Eq. (1.35) that

$$\tilde{D}_O = \frac{4 D_{ion} D_{eon} c_{ion} c_{eon}}{4 D_{ion} c_{ion} + D_{eon} c_{eon}} \left(\frac{1}{4 c_{ion}} + \frac{1}{c_{eon}} \right) \tag{5.10}$$

The p_{O_2}-dependent oxygen vacancy and polaron concentrations can be obtained from the thermodynamic treatment in Section 1.2. If not directly available, the diffusivities may be obtainable from the electrical mobilities, $\bar{\mu}$, through the Nernst-Einstein relationship (Eq. (1.25)). Using the mobility data reported for SDC15,[2] such an analysis yields the ambipolar diffusion coefficient presented in Figure 5.5, where both the directly measured[2] and computed $\tilde{D}_O$ values for a range of temperatures and oxygen partial pressures are presented. The slight deviations between the two sets of values are due to slight dependences of the mobilities on carrier concentrations, a consideration not explicitly accounted for in the calculation. In principle the p_{O_2}-dependent mobilities can be directly utilized for the computation, however, for high

temperatures outside of the measurement range of the earlier experiments, the nature of the p_{O_2} dependence is unknown, precluding extrapolation of the measured data to the higher temperatures of interest for thermochemical cycling. As the diffusion coefficient is, overall, relatively insensitive to both oxygen partial pressure and temperature, these subtleties are not explored further here. Under the limiting conditions in which the doped material is held deep in the electrolytic regime such that $D_{eon}c_{eon} \ll D_{ion}c_{ion}$ (requiring $c_{eon} \ll \dfrac{c_{ion}}{10}$ because of the higher mobility of electrons), Eq. (5.10) reduces to $\tilde{D}_O \sim D_{eon}$. Deep in the electronic regime in which $2c_{ion} \cong c_{eon}$, the ambipolar diffusion coefficient reduces to $\tilde{D}_O \sim \dfrac{3D_{ion}D_{eon}}{2D_{ion} + D_{eon}}$. For fixed mobilities, $\tilde{D}_O$ of acceptor-doped ceria decreases with increasing defect concentrations (increasing δ, decreasing p_{O_2}) as the transport process transforms from one that is determined entirely by the electron mobility to one that is an appropriately weighted average of both the electron and vacancy mobilities. More significant is the overall remarkably high value of $\tilde{D}_O$, falling within the range of 1.7×10^{-5} to 1.1×10^{-4} cm^2 s^{-1} at 800 °C and within 2.1×10^{-4} and 3.6×10^{-4} cm^2 s^{-1} at 1,500 °C.

For undoped ceria, the electron and oxygen ion vacancy concentrations are related according to $2c_{ion} = c_{eon}$ under all relevant oxygen partial pressures and temperatures and, accordingly, the latter limiting expression for $\tilde{D}_O$ applies under all conditions. This consideration implies, in turn, that the ambipolar diffusion coefficient is independent of defect concentration under the ideal solution limit. Assuming that the vacancy and polaron mobilities are the same in doped and undoped ceria, the value for this fixed ambipolar diffusion coefficient
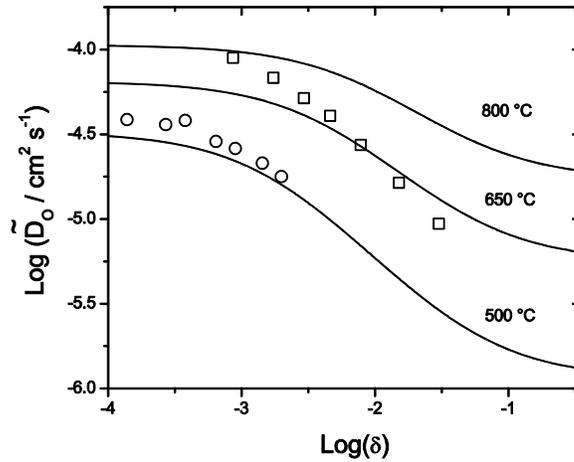
Figure 5.5: Computed (solid lines) and experimental (points) values for the neutral oxygen ambipolar diffusion coefficient in SDC15 as a function of oxygen nonstoichiometry, assuming ideal solution behavior. Computed values based on reported mobilities and defect concentrations (extrapolated values employed for 800 °C calculation) after Lai & Haile.[2] Deviation between the measured and the calculated diffusivities are primarily due to a slight dependence of the measured electronic mobility on oxygen partial pressure, not accounted for in the calculation.

corresponds to the minimum value encountered in doped ceria, *i.e.*, that at high δ. At low oxygen nonstoichiometry (close to ambient oxygen partial pressures) the chemical diffusion coefficient in SDC15 is substantially higher than it is in undoped ceria. The difference is about one order of magnitude at 700 °C and increases at lower temperature due to the larger enthalpy of vacancy ion migration than electron migration.

With the values of the ambipolar diffusion coefficient at hand, it is possible to obtain the characteristic time, $t \sim \dfrac{l^2}{4\tilde{D}_O}$, for a diffusion-limited process, where l is the diffusion length. Using the lowest value of $\tilde{D}_O$ (SDC15) for each temperature in the 500 to 900 °C range and a diffusion length of 5 μm (a typical grain size in porous ceria), the characteristic diffusion time falls in the range of only 4 to 0.2 ms. A more rigorous calculation which takes into the account

Table 5.1: Simulation parameters for calculating oxygen diffusion profile in a ceria sphere. c_O^0
is the concentration of oxygen in the fully oxidized CeO_2 (4.8×10^{28} m^{-3}).

Symbol	Parameter	Value	Reference
$2l$	Diameter of sphere	10^{-5} m	
c_{gas}	Effective gas phase lattice oxygen concentration	$0.9625 \times c_O^0$	
c_{dop}	Trivalent dopant concentration	$0.075 \times c_O^0$	
$c_O(t=0)$	Initial lattice oxygen concentration	$0.9375 \times c_O^0$	
$D_i(T)$	Oxygen ion diffusion coefficient	$10^{-3357/T - 6.062}$ m^2 s^{-1}	2
$D_e(T)$	Small polaron diffusion coefficient	$10^{-1423/T - 6.647}$ m^2 s^{-1}	2
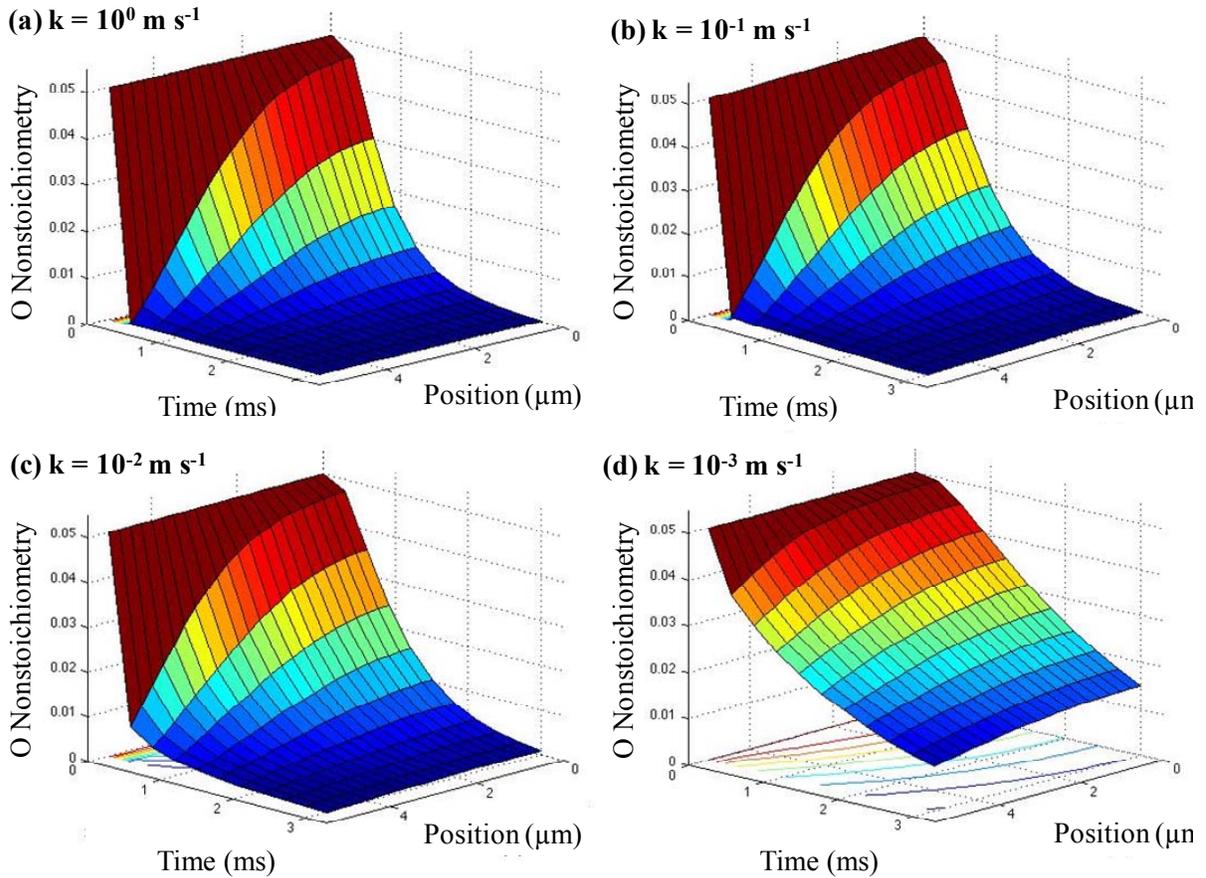
Figure 5.6: Numerical calculation of oxygen nonstoichiometry during oxidation of SDC15 spheres at 900 °C. Initial oxygen nonstoichiometry at 0.05 throughout the sphere. For a sufficiently high surface activity (k), the solution is independent of k. When limited by oxygen ambipolar diffusion in SDC15, the reaction time is approximately 2 ms.

the temporal and positional variation of $\tilde{D}_O$ as the reaction proceeds is given below.

The transport equations (Eqs. (1.33), (1.34), and (5.10)) are solved numerically to obtain the time-dependent oxygen concentration profiles in a MIEC sphere (spherical symmetry) with a radius $r = l$ under isothermal, non-equilibrium conditions. Specifically, the initial oxygen concentration $c_O(t = 0)$ is assumed to be uniform in the sphere and takes on a value equivalent to $\delta = 0.05$. The effective lattice oxygen concentration in the gas phase, c_{gas} is set to a value equivalent to $\delta = 0$. Given that the purpose of this computation is to evaluate the contribution of $\tilde{D}_O$ to the concentration profile, a simple, first order Chang-Jaffe boundary condition is used to describe the surface exchange kinetics:

$$j\big|_{r=l} = k(c_O\big|_{r=l} - c_{gas})$$
(5.11)

where k is the surface reaction rate-constant. By definition, $j\big|_{r=0} = 0$. Boundary layer and gas phase mass transport effects are not considered, and c_{gas} is taken to be position and time independent. The simulation parameters are listed in Table 5.1.

The concentration surface contour plots computed at 900 °C and at $k = 10^0$ m s^{-1} and $k = 10^{-1}$ m s^{-1} (Figure 5.6(a-b)) show negligible differences, confirming that for sufficiently large values of k, surface exchange coefficients cease to affect the bulk oxygen concentration profile. In other words, the oxidation reaction is limited exclusively by the bulk diffusion of ions and small polarons. In this case, the time required for the oxidation reaction to proceed to 90 % completion is approximately 2 ms. For $k < 10^{-3}$ m s^{-1}, surface kinetics can no longer be neglected and results in a significant increase in the total reaction time. Calculations carried out at 500 °C yields similar behavior, with a reaction time of $\sim$ 40 ms in the diffusion-limited regime.

The diffusion times calculated above are compared with values observed experimentally. The measured oxidation reaction time is 3 min at 800 °C (*i.e.* time required to produce 90 % of the total product produced), Figure 5.4, and is more than 3 orders of magnitude greater than the computed diffusion time. Therefore, it is safe to conclude that the reduction and oxidation reactions are not limited by oxygen ambipolar diffusion of oxygen.

5.4 Oxidation of Ceria by CO_2

The kinetics of ceria oxidation by CO_2, both independently and as a mixture with H_2O, was examined experimentally using an electric-furnace-based system described in Section 2.2.3. SDC15 was pretreated at 1,500 °C for 24 h to simulate possible deactivation due to sintering and then reduced to an oxygen nonstoichiometry of 0.05 using a H_2-H_2O-Ar mixture. Unlike the system used in Section 5.3, the experimental setup used here cannot achieve the temperature necessary for thermal reduction in an inert gas. Under differential reactor conditions of relatively low reactant partial pressures (0.01 − 0.08 atm) and moderate temperatures (500 − 700 °C), it was possible to slow the reaction sufficiently so that the temporal dependence of H_2 and CO production could be accurately captured by a gas chromatograph (GC), which provides greater sensitivity towards the CO signal than the mass spectrometer used in Section 5.3. In the case of SDC15 oxidation with CO_2 between 500 and 700 °C, CO_2-to-CO conversion was achieved without carbon deposition, as verified by post situ temperature programmed oxidation (TPO) (this observation contradicts thermodynamic expectations, Figure 5.2, and will be discussed below). Overall, the activation energy for CO_2 dissociation is 0.80 ± 0.02 eV and the reaction order, *n*, for CO production is 0.77 ± 0.02 (assuming a power law for the reaction rate, $r = k p_{CO_2}^n \delta^m$). Turning to water-splitting, the activation energy is lower than that of CO_2-

(a)

(b)

(c)

(d)
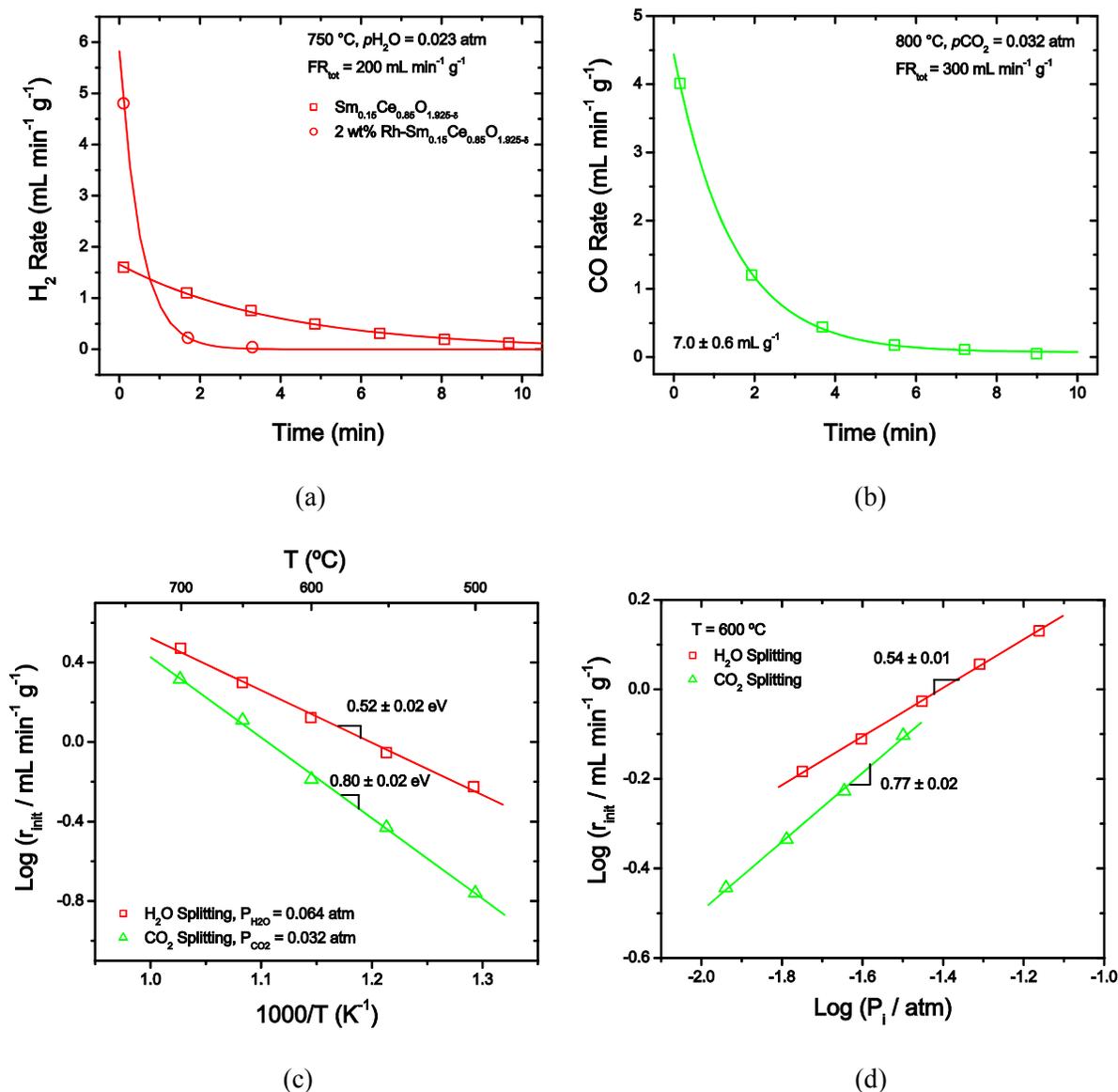
Figure 5.7: (a) H_2 production rate as a function of time, as measured by GC, upon reaction of H_2O with reduced SDC15 ($\delta = 0.05$) with and without Rh catalyst at the conditions indicated. **(b)** CO production rate as a function of time at the conditions indicated. No carbonaceous species were detected as verified by post situ temperature programmed oxidation. Initial production rates of H_2 and CO as functions of **(c)** temperature and **(d)** reactant partial pressures when H_2O and CO_2 are individually reacted with reduced SDC15, respectively. The initial state of SDC15 is assumed to be at the same in all cases. The instantaneous reactant conversion rate was kept below 20 % to satisfy the gradient-less reactor and isothermal approximations ($\Delta T < 3$ °C). To avoid equilibrium limitations in the fuel production reactions, reactant flow rates were kept sufficiently high such that the $p_{H_2O} : p_{H_2}$ and $p_{CO_2} : p_{CO}$ ratios at the exhaust were always above 9 (for determining reaction orders) and above 5 (for determining activation energies).

According to thermodynamic predictions (Section 5.2), reaction of H_2O and CO_2 simultaneously with reduced SDC15 should yield a pure mixture of H_2 and CO (synthesis gas, or syngas) at temperatures above 715 ºC. Below this temperature, significant amounts of solid carbon and/or CH_4 are thermodynamically preferred. For example, ~ 89 % of the C atoms are expected to be in the form of solid carbon at 650 ºC, and further reductions in temperature increasingly favor CH_4 formation (Figure 5.2). To evaluate kinetics of carbon and CH_4 formation, simultaneous oxidation of ceria by a mixture of H_2O and CO_2 was carried at temperatures between 400 and 900 °C (inlet $H_2O:CO_2$ = 2:1, pH_2O = 0.06 – 0.13 atm). In agreement with thermodynamic expectations, a technologically desirable $H_2:CO$ ratio of 2:1 was achieved at 900 °C, with 90 % of ceria oxidized under 2 min (Figure 5.8). However, experiments conducted at 400 - 700 °C, and even at an extremely low space velocity (4300 h^{-1}), did not yield any CH_4 or solid carbon (the latter confirmed by a subsequent TPO experiment on the reacted SDC15) and but, rather, resulted in a 100 % selectivity for syngas (Figure 5.9, Table 5.2).
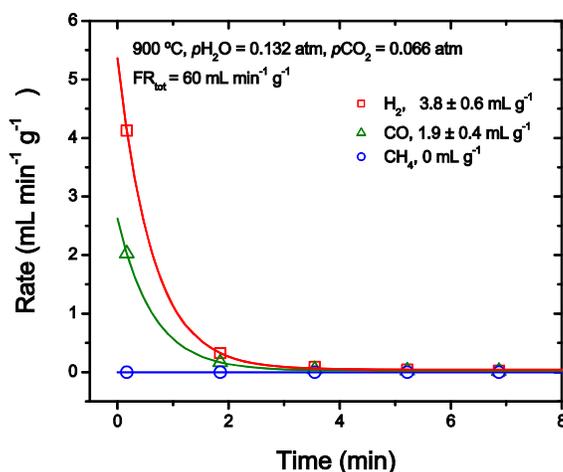
Figure 5.8: Typical synthesis gas (CO + H_2) production curve upon reaction of H_2O and CO_2 with reduced SDC15.
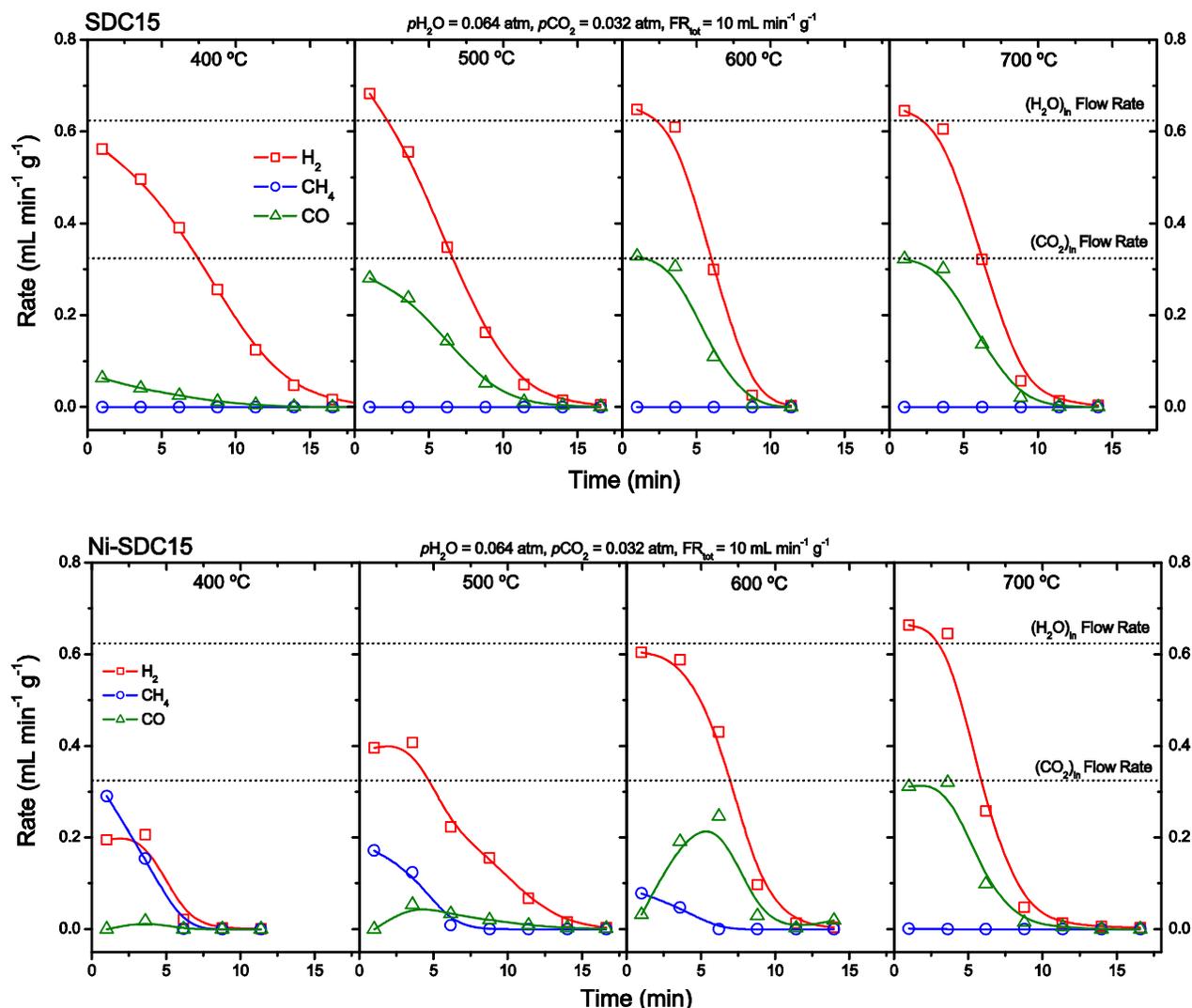
Figure 5.9: Production rate of H_2, CO, and CH_4 when reacting H_2O and CO_2 with reduced SDC15 **(top)** and with reduced Ni-SDC15 **(bottom)** at the indicated conditions. Despite thermodynamic driving forces, no CH_4 or carbonaceous species were formed in the absence of Ni catalysts.

Table 5.2: Product distribution corresponding to SDC15 in Figure 5.9

Temperature (°C)	V_{H2} (mL g⁻¹)	V_{CH4} (mL g⁻¹)	V_{CO} (mL g⁻¹)	S_{CH4} (%)	$\Delta\delta$
400	4.7 ± 0.4	0	0.36 ± 0.08	0	0.039 ± 0.003
500	4.5 ± 0.4	0	1.8 ± 0.1	0	0.049 ± 0.004
600	3.9 ± 0.3	0	1.8 ± 0.1	0	0.044 ± 0.004
700	4.1 ± 0.3	0	2.0 ± 0.2	0	0.047 ± 0.004

Table 5.3: Product distribution corresponding to Ni-SDC15 in Figure 5.9

Temperature (°C)	V_{H2} (mL g⁻¹)	V_{CH4} (mL g⁻¹)	V_{CO} (mL g⁻¹)	S_{CH4} (%)	$\Delta\delta$
400	1.0 ± 0.1	1.1 ± 0.1	0.05 ± 0.01	80	0.041 ± 0.003
500	3.2 ± 0.3	0.7 ± 0.1	0.28 ± 0.02	46	0.049 ± 0.004
600	4.3 ± 0.3	0.30 ± 0.02	1.3 ± 0.1	18	0.053 ± 0.004
700	4.1 ± 0.3	0	1.9 ± 0.2	0.2	0.046 ± 0.004

Since thermodynamics favors CH_4 production at moderate temperatures, the introduction of a catalyst that interacts more strongly with carbon than does ceria could facilitate production of CH_4 rather than syngas. Ni is a well-known CO hydrogenation and methanation catalyst[114] and has been shown to interact with ceria support strongly to enhance the performance of dry methane reforming.[115] Accordingly, CH_4 generation was explored using SDC15 impregnated with 10 wt% Ni deposited (Ni-SDC15). Reduced Ni-SDC15 was exposed to mixtures of diluted H_2O and CO_2 ($H_2O:CO_2$ = 2:1) at temperatures between 400 °C and 700 °C. The results, Figure 5.9 and Figure 5.10 reveal a remarkably high selectivity for CH_4 generation, defined as $S = 4V_{CH_4}\big/\left(4V_{CH_4} + V_{H_2} + V_{CO}\right)$, where V_i is the component gas volume, reaching almost 80 % at 400 °C. Considering the sum of all fuels generated, the extent of reaction (defined as the ratio of fuel produced to the theoretical fuel productivity as set by the initial oxygen deficiency), is unity, to within experimental error (Table 5.4). *Post situ* TPO analysis of reacted samples indicated the absence of solid carbon. Overall, the product composition is in good agreement with thermodynamic expectations in which CH_4 yield decreases with temperature, becoming
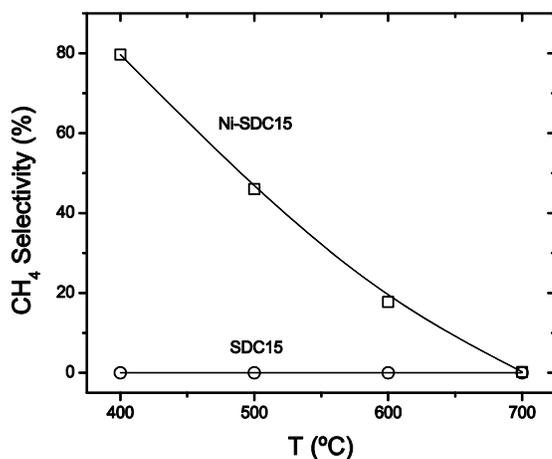
Figure 5.10: CH_4 product selectivity when reacting H_2O and CO_2 with reduced SDC15, with and without Ni catalyst (same reaction condition as indicated in Figure 5.9).
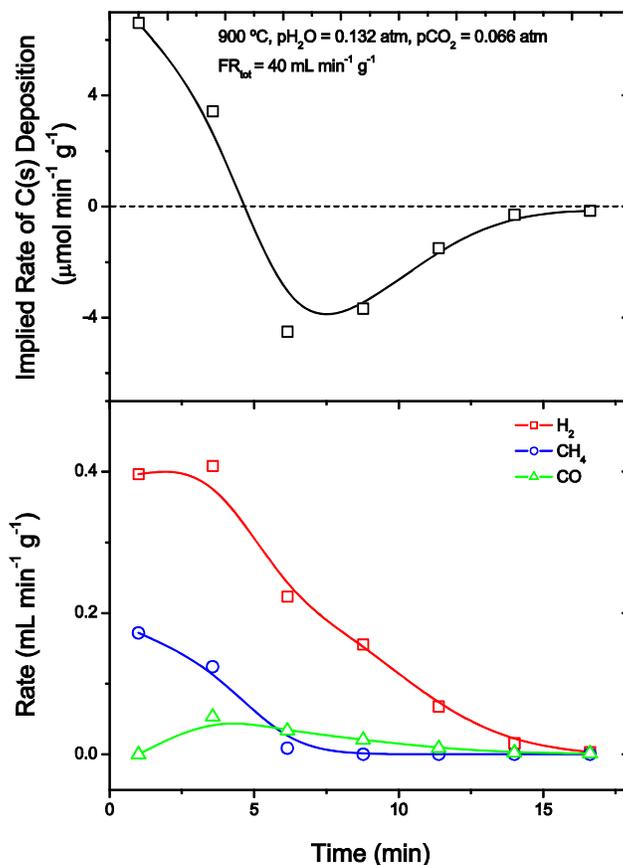
Figure 5.11: (Top) Implied rate of C(s) deposition that occurs upon reaction of H_2O and CO_2 with reduced 10 wt% Ni-SDC15 at the conditions indicated. **(Bottom)** fuel production rates. Solid carbon formation rate is calculated by taking the difference between the carbon in the product gases and that in the reactants. Integration of the carbon formation rate curve with time indicates zero carbon accumulation (within error).

negligible at 700 °C.

In contrast to experiments in the absence of Ni, the profiles of fuel production in the presence of the catalyst show a temporal evolution that is not a simple monotonic decay, Figure 5.9. In particular, at lower temperatures H_2 production is essentially flat before decreasing, whereas CO production is initially negligible, then rises and falls. The product formation rates is analyzed together with the transient solid carbon formation rate, calculated by taking the difference between the carbon in the product gases and that in the reactants (Figure 5.11). At the onset of

the reaction, CH_4 and H_2 formation are accompanied by carbon deposition. Approximately midway through the reaction, the CH_4 formation rate becomes negligible and carbon formation rate turns negative, indicating that the deposited carbon is being oxidized. Integration of the carbon formation rate curve over the entire reaction yields zero carbon accumulation (within error), indicating that there is no net carbon formation over the full course of the reaction was found to be zero, consistent with the TPO data for the reacted sample.

It is proposed that, in the presence of Ni, surface carbonaceous species (collectively referred to as C(s)) form on the metal catalyst surface and/or near the metal-ceria interface and that these intermediate species react with the rapidly produced hydrogen to yield CH_4. Because C(s) is consumed due to deposition, it is not available to form CO. As the reaction progresses, the local hydrogen concentration is no longer sufficient to remove the surface C(s) and the Ni (Ni | SDC15 | gas triple-phase boundary) becomes deactivated, leaving CO_2 to be reduced to CO as it would in the absence of Ni. Simultaneously, the residual carbon reacts with excess H_2O to generate additional CO and H_2, effectively regenerating the Ni surface for subsequent cycles.

To further probe the hypothesis that transient carbonaceous species play a key role in CH_4 production over Ni-SDC15, the kinetics of CO_2 splitting to C(s) and CO were examined using TPO. First, 85 ± 5 μmol g^{-1} of CO_2, (as in the fuel productivity, normalized by the mass of fully oxidized ceria), a quantity insufficient for complete oxidation of the reactant ceria, was injected over reduced SDC15 ($\delta = 0.05$) for 6 min at 500 °C (p_{CO_2} = 0.032 atm) and the product stream monitored. For both SDC15 and Ni-SDC15, CO_2 conversion was complete; that is, no CO_2 was detected in the effluent gas, an expected result given the low injection rate and amount of CO_2 (Figure 5.12(a)). However, while the CO_2 is nearly entirely converted to CO over reduced SDC15, the conversion to CO over Ni-SDC15 was negligible, implying that the CO_2 is,
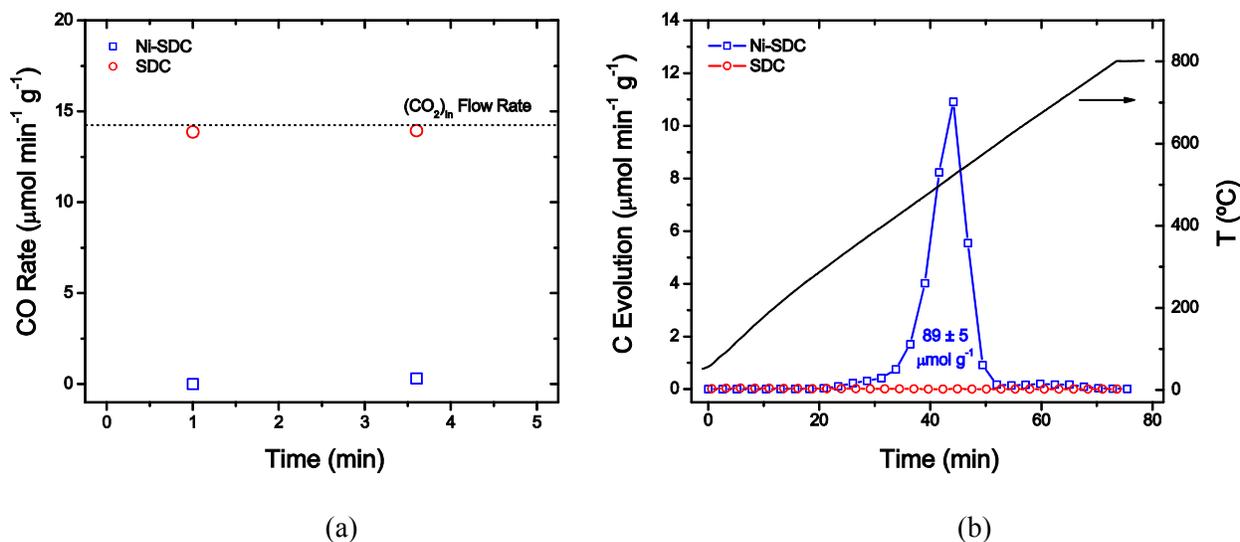
Figure 5.12: (a) Rate of CO production when reacting CO_2 with reduced SDC15, with and without Ni catalyst. **(b)** Post situ TPO reveals that all of CO_2 was converted to C(s) over Ni-SDC15, and none over SDC15.

in the latter case, almost entirely converted to C(s). The occurrence of C(s) was verified *post situ* via a TPO experiment (Figure 5.12(b)). For Ni-SDC15, a large oxidation peak (maximum ~525 °C), with an integrated intensity (corresponding to 89 ± 5 µmol g^{-1}of deposited C(s)) that accounts for ~100 % conversion of the injected CO_2 to C(s), was recorded. In contrast, no carbon oxidation peak was observed for neat SDC15. Therefore, in the absence of H_2O, and under reactant limited conditions, CO_2 is completely reduced to C(s) over Ni-SDC15, whereas it is converted only to CO over SDC15. These observations suggest that the inactivity of neat SDC15 for methane generation is related to the absence of C(s) formation on the oxide surface upon dissociation of CO_2.

5.5 Demonstration of Solar Fuel Production via Thermochemical Cycling

The solar reactor constructed for the purposes of demonstrating thermochemical cycling is shown schematically in Figure 2.2 and described in detail in Section 2.2.4. It consists of a cavity-receiver with a windowed aperture through which concentrated solar radiation enters. The selected dimensions ensure multiple internal reflections and efficient capture of incoming solar energy; the apparent absorptivity exceeds 0.94, approaching the ideal blackbody limit. The reactive ceria, assembled from quarter-circular-arc pieces into the form of a cylinder (325 g in mass, 35 mm in outer diameter, 102 mm in height, and 80% in porosity as-fabricated), is placed inside the cavity and subjected to multiple heat-cool cycles under appropriate gases to induce fuel production, Figure 5.13. The peak solar flux intensity to which the reactor was exposed exceeded 2,000 suns (1 sun = 1 kW m^{-2}). An annular gap between the ceria and the alumina insulation tiles suppressed undesired reactions between the two components. *Post situ* x-ray diffraction showed that, with the exception of the portion which was in direct contact with the insulation material, the ceria remained phase-pure and free of detectable alumina incorporation.

To drive oxygen evolution, the solar reactor was purged with flowing argon ($p_{O_2} = 10^{-5}$ atm) and the incident radiation power ramped to approximately 1.9 kW at a mean solar flux intensity of 1,500 suns, typical of a commercial solar concentration system. The temperature of the ceria tube rose to values between 1,420 and 1,640 °C, with the exact temperature dependent on the position within the reactor and on the cycle (Figure 5.13(a)). The rise in temperature was rapid below 1,250 °C, at an average rate of 140 °C min^{-1}, and slowed to an average of 8 °C min^{-1} as the temperature approached steady-state due to increasing heat dissipation by re-radiation through the aperture and conduction heat transfer through the
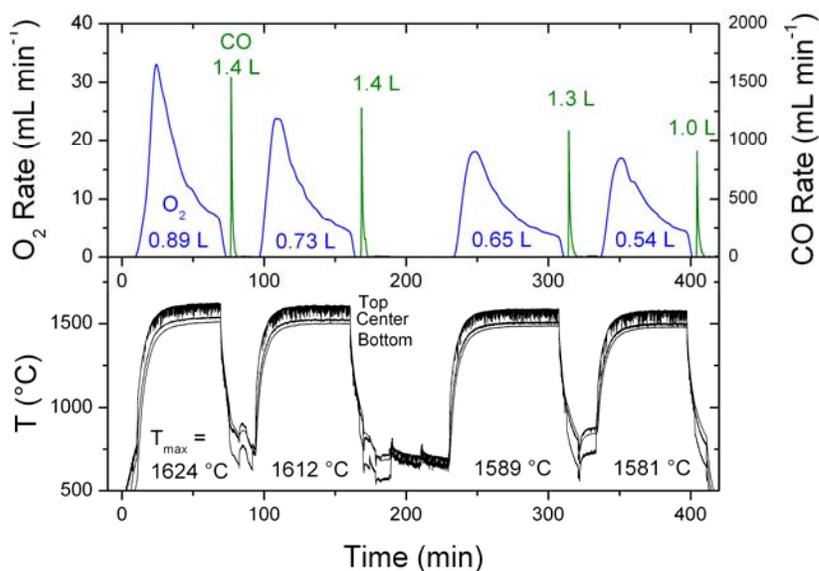
(a)
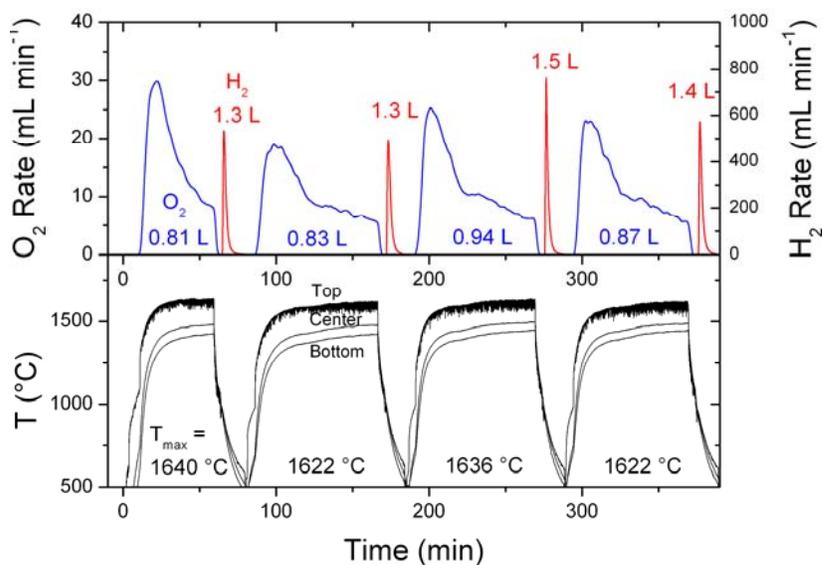
(b)

Figure 5.13: Thermochemical cycling of CeO_2 (325 g) using the solar reactor with **(a)** CO_2 and **(b)** H_2O as oxidant. The oxygen and fuel evolution rate as well as the total volume of gas evolved are shown. Temperatures were measured at three positions along the height of the ceria tube. Maximum temperatures (T_{max}) attained in the reactor are shown. Conditions for (a): Ar sweep gas at a flow rate of 0.0062 L min^{-1} g^{-1} during the ceria reduction half-cycle, and CO_2/Ar at $pCO_2 =$ 0.78 atm and a flow rate of 0.035 L min^{-1} g^{-1} during the ceria oxidation half-cycle. Conditions for (b): Ar sweep gas at a flow rate of 0.023 L min^{-1} g^{-1} during the ceria reduction half-cycle, and H_2O/Ar at $pH_2O = 0.78$ atm and a flow rate of 0.023 L min^{-1} g^{-1} during the ceria oxidation half-

insulation. Oxygen evolution from ceria was observed at an onset temperature of approximately 900 °C, consistent with equilibrium thermogravimetry measurements (Figure 5.1) The rate of evolution increased with temperature, reaching a peak value of 34 ± 2 mL min^{-1} and an average value of 16 ± 1 mL min^{-1} (defined as the instantaneous reaction rate averaged over the time required to reach 90 % of the extent of reaction) on the first cycle (Figure 5.13(a)). When the rate dropped to 20 % of the peak value, the evolution reaction was terminated by decreasing the intensity of the incident radiation flux. Upon cooling to ~ 900 °C, CO_2 was injected into the solar reactor. Production of CO was immediately observed, reaching a remarkable peak rate of $1.5 \pm 0.1 \times 10^3$ mL min^{-1} and an average rate of $5.9 \pm 0.4 \times 10^2$ mL min^{-1} (Figure 5.13(a)). Consistent with the fact that there was no water present in the reactant stream, no gas-phase C_1, C_2, or C_3 hydrocarbons were detected by the gas chromatograph. Carbon-neutral balance (< 3 % C unaccounted, well within error) was achieved by summing the flow rates of CO_2 in the reactant stream and CO_2 and CO in the product steam. As verification, temperature-programmed oxidation was performed on ceria after the CO_2 dissociation reaction by flowing oxygen into the solar reactor while ramping the temperature to 1,000 °C. Both CO and CO_2 levels were below the detection-limit, confirming that no appreciable amount of carbonaceous species was deposited onto ceria during CO_2 dissociation, and that a 100 % selectivity towards CO production was achieved. Upon the termination of CO production, the radiation flux was increased and the entire cycle repeated. An analogous set of experiments was also performed for H_2O dissociation, with H_2 production rate reaching a peak value of $7.6 \pm 0.8 \times 10^2$ mL min^{-1} and a maximum average value of $3.1 \pm 0.3 \times 10^2$ mL min^{-1} (Figure 5.13(b)). A total of 23 cycles were performed. An experimental run performed without the ceria confirmed the absence of O_2, CO, or H_2 evolution under corresponding reaction conditions.

The characteristics of solar-thermochemical fuel production from ceria reveal several important features of the cyclic process. Although the behavior is generally reproducible between cycles, some run-to-run variations are evident. The oxygen evolution reaches a peak value between 17 and 34 mL min^{-1} whereas the total amount evolved ranges from 0.54 to 0.94 L for 325 g ceria. These differences are correlated with the peak reactor temperature obtained, variations in which are attributed to unsteady heat transfer. Taking this temperature variability into account, the total oxygen evolution is found to be generally consistent with thermodynamic expectations (Figure 5.1). The total fuel produced in the ceria oxidation half-cycle, either CO or H_2, is furthermore close to the 2-to-1 volumetric ratio relative to the O_2 released expected for full utilization of the ceria nonstoichiometry. Specifically, for CO_2 dissociation, the $CO:O_2$ ratio ranges from $1.6 \pm 0.2{:}1$ to $2.0 \pm 0.2{:}1$, whereas for H_2O dissociation, the $H_2:O_2$ ratio was $1.6 \pm 0.2{:}1$.

Perhaps the most obvious feature of the cycling behavior, Figure 5.13, is the much faster rate of fuel production than that of O_2 release. It was observed that lowering the purge gas flow rate during ceria reduction by a factor of 4 had no significant impact on the oxygen evolution rate, indicating that the mass transport of oxygen gas through the pores of the ceria is not the rate-limiting step. One can consider, as an alternative, that the oxygen evolution kinetics in the solar reactor are limited by the heating rate, a factor that does not impact fuel production as this step occurs isothermally. If the heating rate is slow relative to the surface reaction and solid-state diffusion steps involved in oxygen release, the oxygen evolution rate can be expressed as $d\delta/dt \approx \left(d\delta/dT \right)_{T=T(t)} \left(dT/dt \right)$. Using the spatially-averaged temperature profile in the first cycle in Figure 5.13(a)f, a maximum oxygen evolution rate of 65 mL min^{-1} is obtained, which, given the approximate nature of the calculation, is comparable to the observed rate.
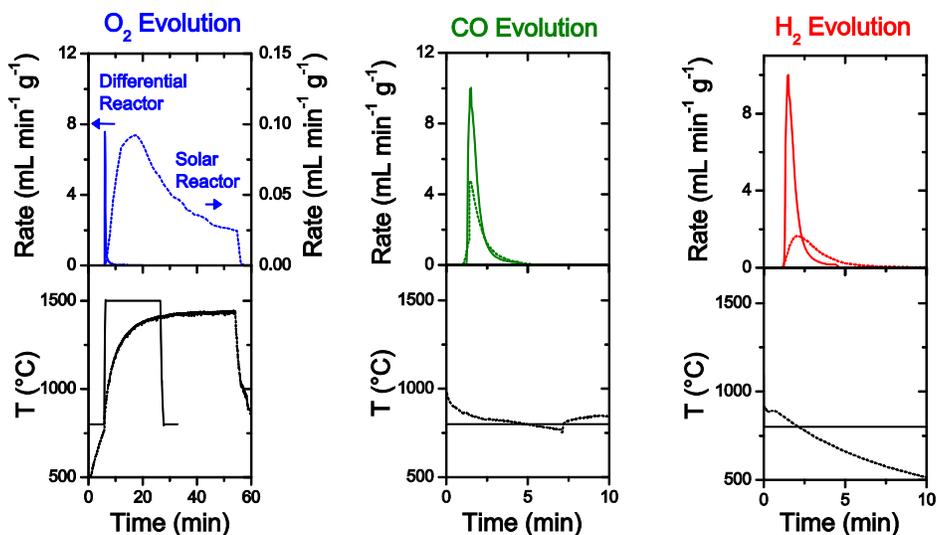
Figure 5.14: Comparison of **(a)** O_2, **(b)** H_2, and **(c)** CO evolution between the solar reactor (dotted lines) and the infrared-furnace-based differential reactor (solid lines). Experimental conditions for the solar reactor are the same as those for Figure 5.13. In the differential reactor, 0.429 g of CeO_2 was cycled between 1,500 °C (Ar sweep gas flow rate = 2.3 L min^{-1} g^{-}, 20 min) and 800 °C (CO_2-splitting: pCO_2 = 0.5 atm, flow rate = 1.2 L min^{-1} g^{-1}, 10 min ; H_2O-splitting: pH_2O = 0.44 to 0.52 atm, flow rate = 2.1 to 2.5 L min^{-1} g^{-1}, 10 min).

To assess the effect of mass and heat transfer, the oxygen and fuel evolution rates obtained using the solar reactor are compared to those obtained using the infrared-furnace-based reactor. Thermochemical cycling of ceria was carried out using identically-prepared monolithic porous samples 0.4 g in mass. Such an experimental setup permitted operating the thermochemical cycle under high-flow, differential reactor conditions, in which the sample temperature can be changed rapidly (average ramp rate of 1,700 °C min^{-1}) and the gas composition approach uniformity within the porous media. Under these ideal conditions in which only surface chemical reactions and solid-state oxygen diffusion in ceria limit the overall reaction rate, oxygen-evolution (Figure **5.14**) attained a peak instantaneous rate that is ~ 80 times faster than the solar reactor, reaching a remarkable average rate of 2.2 ± 0.2 mL min^{-1} g^{-1}$_{ceria}$; CO_2 and H_2O dissociation reactions were ~ 2 and 4 times faster (though the reactant partial pressures differ slightly between the

differential and solar reactor), with rates of 5.1 ± 0.4 and 5.3 ± 0.4 mL min^{-1} g^{-1}$_{ceria}$, respectively. These rates support the proposition that oxygen evolution kinetics in the solar reactor are limited predominantly by the heating rate.

The solar-to-fuel energy conversion efficiency is defined as:

$$\eta = \frac{r_{fuel}\Delta H_{fuel}}{P_{solar} + r_{inert}E_{inert}} \tag{5.12}$$

where r_{fuel} is the molar fuel production rate, ΔH_{fuel} is the higher heating value of the fuel, P_{solar} is the incident solar radiation power, r_{inert} is the flow rate of the inert gas during oxygen evolution, and E_{inert} is the energy required to separate the inert sweep gas from air (usually N_2; Ar was utilized in this work entirely for reasons of experimental convenience). Based on the experimental data, the peak instantaneous efficiencies for CO_2 and H_2O dissociations reached 0.8 % and 0.7 %, respectively. No heat recuperation strategy was employed. Upon averaging the efficiencies over the time required to produce 80% of the fuel, they become 0.4 % (for both CO_2 and H_2O dissociations). These experimentally measured efficiencies reflect both intrinsic material properties as well as the solar reactor design and operation. An energy-balance analysis reveals that 50 % of the energy loss resulted from heat conduction through the reactor wall and 41 % resulted from re-radiation through the aperture. The former energy penalty can be dramatically reduced by improving thermal insulation and by scaling up because of the volume-to-area ratio. The latter can be minimized by augmenting the solar flux such that the aperture size can be reduced. Decreasing heat loss also has the added benefit of increasing the temperature ramp rate. As shown in the earlier comparison of the oxygen-evolution kinetics under slow and rapid heating rates, the oxygen evolution kinetics and conversion efficiency are closely related to
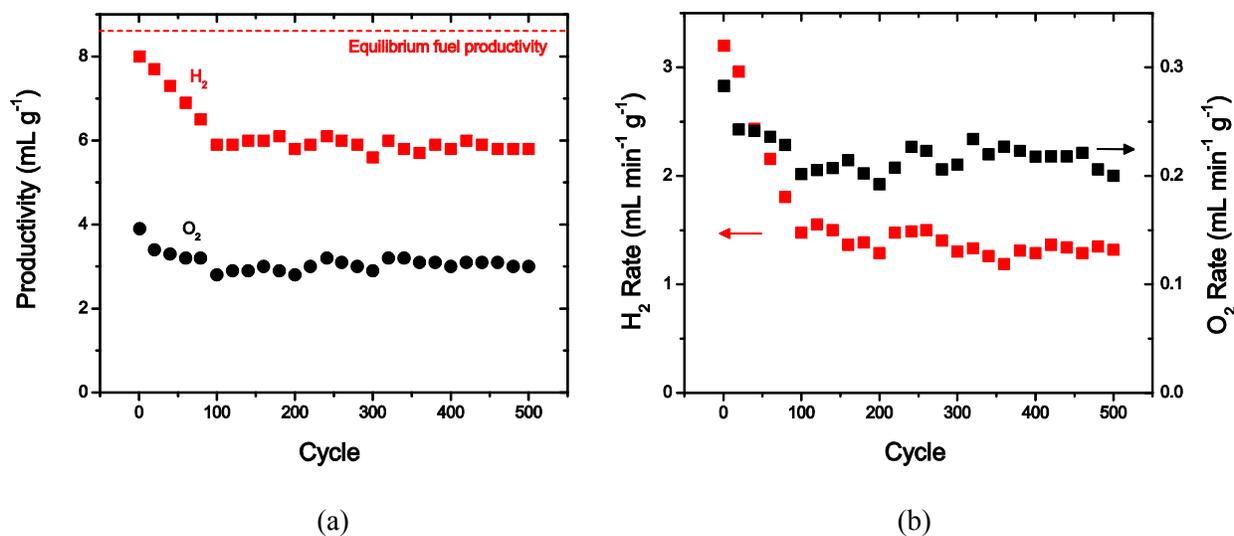
Figure 5.15: (a) H_2 and O_2 productivity (dotted line indicates equilibrium value under an excess H_2O reactant condition) and **(b)** isothermal H_2 production rate as a function of cycle count. CeO_2 was thermochemically cycled between 1,500 °C ($pO_2 = 10^{-5}$ atm, $FR_{tot} = 1,000$ mL min^{-1}, 10 min) and 800 °C ($pH_2O = 0.13 – 0.15$ atm, $FR_{tot} = 230$ to 235 mL min^{-1}, 10 min). Fuel production rate is calculated by averaging the instantaneous rate over the time required to reach 90% of the fuel produced.

the rates at which the active ceria materials can be heated and cooled.

Beyond efficiency, material stability is an essential criterion for a viable thermochemical process. In any technologically significant thermochemical process, fuel productivity (fuel per unit of oxide, mL g^{-1}) and production rates (fuel per time per unit of oxide, mL min^{-1} g^{-1}) must remain high over thousands of cycles. Using the differential reactor system, which enables rapid access to multiple cycles, 500 cycles of water dissociation were performed without interruption. What is evident from the long-term cycling behavior, Figure 5.15 ($T_H = 1,500$ °C, $T_L = 800$ °C), is that the hydrogen production rate decreases by about 50 % over the first 100 cycles, then maintains a stable value of 1.3 mL min^{-1} g^{-1} for the remaining 400 cycles. The hydrogen and oxygen productivity mirror the hydrogen production rate, decreasing, respectively, from initial

values of 8.0 and 4.0 mL g^{-1} to stable values of 6.0 and 3.0 mL g^{-1} after about 100 cycles. Most significant is that for all cycles all of the nonstoichiometry created in the ceria during high temperature reduction is subsequently utilized in the low temperature water dissociation step, despite the clear loss in rate for this reaction. That is, the volumetric ratio of hydrogen to oxygen produced remains at approximately 2 throughout cycling. The overall decrease in productivity (of both oxygen and hydrogen) can be understood to be a result of the decreased reaction rates in combination with a fixed cycle time (10 min for each half-cycle) that is no longer sufficient for complete reaction. At the conclusion of the cycling experiment, it was verified that an oxygen release amount of 4 mL g^{-1} can indeed be obtained if the reaction is allowed to proceed to completion.

The decrease in reaction rates is most likely due to a loss in ceria surface area, Figure 5.16, which limits the available sites for reaction to occur. Prior to thermochemical cycling, the ceria was formed into a porous monolith with a specific surface area of 0.1 m^2 g^{-1} by sintering in the presence of a fugitive pore-former. The resulting material was subsequently annealing for 3 h at 1,500 °C in an attempt to stabilize the microstructure. By this process, a highly porous structure (~ 70% porosity) formed of grains with an average size of ~5 μm was obtained. After completion of the 500 cycles, coarsening of the microstructure is clearly evident, with the average grain size increasing to ~ 15 μm and each grain becoming significantly more faceted. These results emphasizes that any path to higher overall fuel production rates (based on shorter cycle times) should focus on the surface characteristics of ceria.
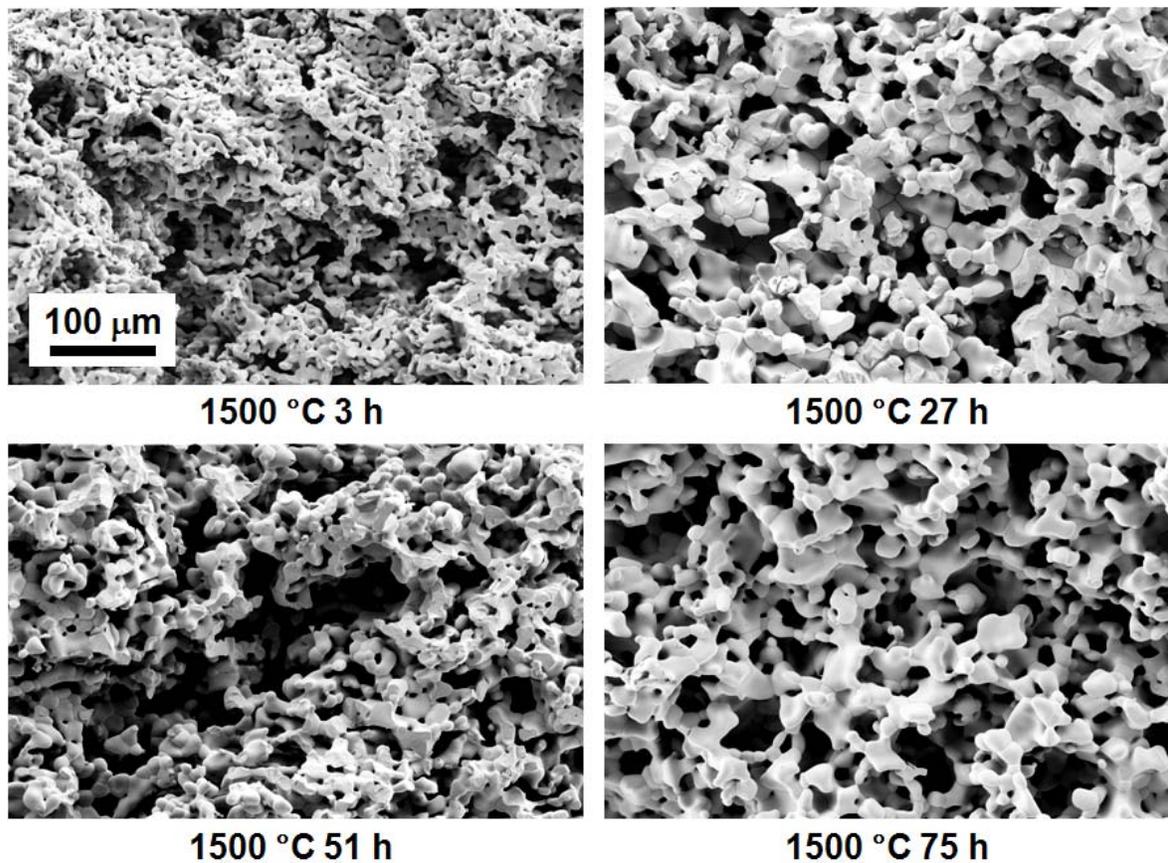
Figure 5.16: Evolution in the ceria morphology after sintering porous CeO$_2$ at 1,500 °C for the indicated number of hours.

Chapter 6

Summary & Conclusion

The electrochemical and thermochemical properties of ceria were investigated, with particular emphasis on surface catalysis, near-surface transport, and bulk transport. Relevant to solid oxide fuel cell and electrolyzer applications, it was shown that:

(1) Doped ceria is an exceptional electro-catalyst towards hydrogen oxidation and hydrolysis near open circuit conditions. The mixed ionic and electronic conducting nature of ceria permits electrochemical reactions to be carried out far away from the metal current collector, thereby increasing the area available for reactions.

(2) The metallic phase in metal-ceria composite electrodes mostly serves as the current collector and does not contribute significantly to the overall electrochemical current.

(3) Despite the relatively low bulk electronic conductivity in ceria, electron migration between the active site and the metal current collector is relatively facile compared to the surface reaction rate, for typical electrode microstructures.

(4) Electronic carrier concentration in thin film ceria can be obtained by a careful treatment of chemical and interfacial capacitances.

Relevant to ceria-based thermochemical fuel production, it was found that:

(1) Both reduced undoped and samaria-doped ceria are active towards the decomposition of H_2O and CO_2.

(2) Bulk amibpolar diffusion of oxygen is facile and at least four orders of magnitude faster than the surface reaction step for both H_2O and CO_2 dissociations.

(3) Surface carbon does not form on ceria under thermodynamically favored conditions and leads to 100 % selectivity towards CO when reacting CO_2 with reduced ceria at a wide range of temperatures.

Furthermore, demonstration of the ceria-based thermochemical cycle in a custom-design solar reactor achieved solar-to-fuel efficiency of close to 1 % for both H_2 and CO production.

Appendix

A. Equations & Boundary Conditions for the Small-Bias DC Model

The partial differential equations and the boundary conditions solved numerically in Section 3.7.1 are listed below:

$$\nabla^2 c_{eon}^{*(1)} = 0 \tag{A.1}$$

$$\nabla^2 \phi^{*(1)} = 0 \tag{A.2}$$

$$\phi^{(1)}\Big|_{\Gamma_1} = 0 \tag{A.3}$$

$$c_{eon}^{*(1)}\Big|_{\Gamma_1} = 0 \tag{A.4}$$

$$\frac{\partial c_{eon}^{*(1)}}{\partial x}\Bigg|_{\Gamma_2,\Gamma_3} = 0 \tag{A.5}$$

$$\frac{\partial \phi^{*(1)}}{\partial x}\Bigg|_{\Gamma_2,\Gamma_3} = 0 \tag{A.6}$$

$$\frac{\partial c_{eon}^{*(1)}}{\partial y}\Bigg|_{\Gamma_4} = -4\frac{c_{ion}^{eq}}{c_{eon}^{eq}}\frac{\partial \phi^{*(1)}}{\partial y}\Bigg|_{\Gamma_4} \tag{A.7}$$

$$\phi^{*(1)}\Big|_{\Gamma_4} = 1\text{V}\left(\frac{k_B T}{e}\right)^{-1} \tag{A.8}$$

$$\frac{\partial c_{eon}^{*(1)}}{\partial y}\Bigg|_{\Gamma_5} = -\frac{k_B T}{e^2}\frac{k c_{eon}^{*(1)}}{4 D_{ion} c_{ion}^{eq}}\left(1+\frac{4 D_{ion} c_{ion}^{eq}}{D_{eon} c_{eon}^{eq}}\right)\Bigg|_{\Gamma_5} \tag{A.9}$$

$$\frac{\partial \phi^{*(1)}}{\partial y}\Bigg|_{\Gamma_5} = -\frac{k_B T}{e^2}\frac{k c_{eon}^{*(1)}}{4 D_{ion} c_{ion}^{eq}}\left(1-\frac{D_{ion}}{D_{eon}}\right)\Bigg|_{\Gamma_5} \tag{A.10}$$

The boundary condition embodied in Eq. (A.8) requires some comment. In an experimental system, ultimately one fixes the electrochemical potential of electrons and not the electric field at the MIEC | metal interface. In the present analysis, however, the electric field rather than the electron electrochemical potential is taken to be the fixed quantity. In a one-dimensional linear system, the computational results for these two choices are identical in terms of extracted quantities such as impedance. In the present two-dimensional, linear system, there is a small numerical difference between the two. In the case in which the electrochemical potential is fixed, then the electronic current will only flow in a direction normal to the MIEC | metal interface. In the case in which the electric potential is fixed, then the electronic current need not be orthogonal to the interface. The computed differences between these two situations are sufficiently small that there is little impact of the choice on the global conclusions. In the absence of detailed knowledge of the physical properties of the metals, a fixed electric potential along the MIEC | metal interface is assumed largely to avoid the counter-intuitive restriction on electronic current flow implied by a fixed electron electrochemical potential. Moreover, a fixed electric potential is more readily compared to a one-dimensional solution in that the electric field in the metal becomes one-dimensional.

References

1   R. J. Panlener, R. N. Blumenthal & J. E. Garnier. A Thermodynamic Study of Nonstoichiometric Cerium Dioxide. *J. Phys. Chem. Solids* **36**, 1213-1222 (1975).

2   W. Lai & S. M. Haile. Impedance Spectroscopy as a Tool for chemical and Electrochemical Analysis of Mixed Conductors: A Case Study of Ceria. *J. Am. Ceram. Soc.* **88**, 2979-2997 (2005).

3   T. Kobayashi, S. Wang, M. Dokiya, H. Tagawa & T. Hashimoto. Oxygen nonstocihiometry of $Ce_{1-y}Sm_yO_{2-0.5y-x}$ (y=0.1,0.2). *Solid State Ionics* **126**, 349-357 (1999).

4   L. Eyring. *The binary lanthanide oxides: synthesis and identification.* 201 (Kluwer, 1991).

5   M. Mogensen, N. M. Sammes & G. A. Tompsett. Physical, chemical and electrochemical properties of pure an doped ceria. *Solid State Ionics* **129**, 63-94 (2000).

6   A. Trovarelli. Catalytic properties of ceria and CeO_2-containing materials. *Cat. Rev. - Sci. Eng.* **38**, 439-520 (1996).

7   A. J. Jacobson. Materials for Solid Oxide Fuel Cells. *Chem. Mater.* **22**, 660-674 (2010).

8   S. Adler. Factors Governing Oxygen Reduction in Solid Oxide Fuel Cell Cathodes. *Chem. Rev.* **104**, 4791-4844 (2004).

9   S. M. Haile. Fuel cell materials and components. *Acta Materialia* **51**, 5981-6000 (2003).

10   S. P. Jiang & S. H. Chan. A review of anode materials development in solid oxide fuel cells. *J. Mater. Sci.* **39**, 4405-4439 (2004).

11   K. Eguchi, T. Setoguchi, T. Inoue & H. Arai. Electrical properties of ceria-based oxides and their application to solid oxide fuel cells. *Solid State Ionics* **52**, 165-172 (1992).

12   M. Godickemeier & L. J. Gauckler. Engineering of Solid Oxide Fuel Cells with Ceria-based Electrolytes. *J. Electrochem. Soc.* **145**, 414-421 (1998).

13   B. C. H. Steele. Appraisal of Ce1-yGdyO2-y/2 electrolytes for IT-SOFC operation at 500C. *Solid State Ionics* **129**, 95-110 (2000).

14   Z. P. Shao & S. M. Haile. A high-performance cathode for next generation of fuel cells. *Nature* **431**, 170-173 (2004).

15   A. Evans, A. Bieberle-Hutter, J. L. M. Rupp & L. J. Gauckler. Review on microfabricated micro-solid oxide fuel cells membranes. *J. Power Sources* **194**, 119-129 (2009).

16   P.-C. Su, C.-C. Chao, J. H. Shim, R. Fasching & F. B. Prinz. Solid Oxide Fuel Cell with Corrugated Thin Film Electrolyte. *Nano Lett.* **8**, 2289-2292 (2008).

17   Y.-H. Huang, R. I. Dass, Z.-L. Xing & J. B. Goodenough. Double Perovskite as Anode Materials for Solid-Oxide Fuel Cells. *Science* **312**, 254-257 (2006).

18   M. D. Gross, J. M. Vohs & R. J. Gorte. A Strategy for Achieving High Performance with SOFC Ceramic Anodes. *Electrochem. Solid. St.* **10**, B65-B69 (2007).

19   C. Lu, W. L. Worrell, J. M. Vohs & R. J. Gorte. A Comparison of Cu-Ceria-SDC and Au-Ceria-SDC Composites for SOFC Anodes. *J. Electrochem. Soc* **150**, A1357-A1359 (2003).

20   O. A. Marina, C. Bagger, S. Primdahl & M. Mogensen. A solid oxide fuel cell with a gadolinia-doped ceria anode: preparation and performance. *Solid State Ionics* **123**, 199-208 (1999).

21   H. Uchida, T. Osuga & M. Watanabe. High-Performance Electrode for Medium-Temperature Solid Oxide Fuel Cells: Control of Microstructure of Ceria-Based Anodes

with Highly Dispersed Ruthenium Electrocatalysts. *J. Electrochem. Soc* **146**, 1677-1682 (1999).

22   H. Uchida, S. Suzuki & M. Watanabe. High Performance Electrode for Medium-Temperature Solid Oxide Fuel Cells: Mixed Conducting Ceria-Based Anode with Highly Dispersed Ni Electrocatalysts. *Electrochem. Solid. St.* **6**, A174-A177 (2003).

23   S. Wang *et al.* Ni/Ceria Cermet as Anode of Reduced-Temperature Solid Oxide Fuel Cells. *J. Electrochem. Soc* **149**, A927-A933 (2002).

24   T. Tsai & S. A. Barnett. Increased solid-oxide fuel cell power density using interfacial ceria layer. *Solid State Ionics* **98**, 191-196 (1997).

25   T. Tsai & S. A. Barnett. Effect of Mixed-Conducting Interfacial Layers on Solid Oxide Fuel Cell Anode Performance. *J. Electrochem. Soc* **145**, 1696-1701 (1998).

26   E. P. Murray, T. Tsai & S. A. Barnett. A direct-methane fuel cell with a ceria-based anode. *Nature* **400**, 649-651 (1999).

27   T. Nakamura *et al.* Electrochemical Behavior of Mixed Conducting Oxide Anodes for Solid Oxide Fuel Cells. *J. Electrochem. Soc.* **155**, 563-569 (2008).

28   N. S. Lewis & D. G. Nocera. Powering the planet: Chemical challenges in solar energy utilization. *Proc. Nat. Acad. Sci. U.S.A.* **103**, 15729-15735 (2006).

29   National Academy of Sciences, and National Research Council. *Electricity from Renewable Resources: Status, Prospects, and Impediments*. (The National Academies Press, 2009).

30   J. E. Funk. Thermochemical hydrogen production: past and present *Int. J. Hydrogen Energy* **26** 185-190 (2001).

31   T. Kodama & N. Gokon. Thermochemical Cycles for High-Temperature Solar Hydrogen

Production. *Chem. Rev.* **107**, 4048−4077 (2007).

32   T. Nakamura. Hydrogen production from water uilitzing solar heat at high temperatures. *Solar Energy* **19**, 467-475 (1977).

33   A. Steinfeld. Solar thermochemical production of hydrogen - a review. *Solar Energy* **78**, 603-615 (2005).

34   A. Steinfeld, S. Sanders & R. Palumbo. Design aspects of solar thermochemical engineering - a case study: Two-step water-splitting cycle using the Fe_3O_4/FeO redox system. *Solar Energy* **65**, 43-53 (1999).

35   Y. Tamaura, A. Steinfeld, P. Kuhn & K. Ehrensberger. Production of solar hydrogen by a novel, 2-step, water-splitting thermochemical cycle. *Energy* **20**, 325-330 (1995).

36   A. Steinfeld. Solar hydrogen production via a two-step water-splitting thermochemical cycle based on Zn/ZnO redox reactions. *Int. J. Hydrogen Energy* **27**, 611-619 (2002).

37   T. Melchior, N. Piatkowski & A. Steinfeld. H_2 production by steam-quenching of Zn vapor in a hot-wall aersol flow reactor. *Chem. Eng. Sci.* **64**, 1095-1101 (2009).

38   K. Wegner, H. C. Ly, R. Weiss, S. Pratsinis & A. Steinfeld. In situ formation and hydrolysis of Zn nanoparticles for H2 production by the 2-step ZnO/Zn water-splitting thermochemical cycle. *Int. J. Hydrogen Energy* **31**, 55-61 (2006).

39   N. Gokon, T. Mizuno, Y. Nakamuro & T. Kodama. Iron-Containing Yttira-Stabilized Zirconia System for Two-Step Thermochemical Water Splitting. *J. Sol. Energy Eng.* **130**, 011018 (2008).

40   T. Kodama, Y. Nakamuro & T. Mizuno. A Two-Step Thermochemical Water Spliting by Iron-Oxide on Stabilized Zirconia. *J. Sol. Energy Eng.* **128**, 3-7 (2006).

41   J. E. Miller *et al.* Metal oxide composites and structures for ultra-high temperature solar

thermochemical cycles *J. Mater. Sci.* **43**, 4714-4728 (2008).

42   O. Demoulin, M. Navez, J.-L. Mugabo & P. Ruiz. The oxidizing role of CO_2 at mild temperature on ceria-based catalysts *Appl. Catal., B* **70**, 284-293 (2007).

43   T. Jin, T. Okuhara, G. J. Mains & J. M. White. Temperature-Programmed Desorption of CO and COP from Pt/CeO,. An Important Role for Lattice Oxygen in CO Oxidation *J. Phys. Chem.* **91**, 3310-3315 (1987).

44   S. Park, J. M. Vohs & R. J. Gorte. Direct oxidation of hydrocarbons in solid-oxide fuel cell. *Nature* **404**, 265-267 (2000).

45   S. Abanades & G. Flamant. Thermochemical hydrogen production from a two-step solar-driven water-splitting cycle based on cerium oxides. *Sol. Energy* **80**, 1611-1623 (2006).

46   H. Kaneko *et al.* Cerium ion redox system in $CeO_2–xFe_2O_3$ solid solution at high temperatures (1,273–1,673 K) in the two-step water-splitting reaction for solar H2 generation *J. Mater. Sci.* **43**, 3153-3161 (2008).

47   H. Kaneko *et al.* Reactive ceramics of $CeO_2–MO_x$ (M = Mn, Fe, Ni, Cu) for H2 generation by two-step water splitting using concentrated solar thermal energy *Energy* **32**, 656-663 (2007).

48   H. Kaneko & Y. Tamaura. Reactivity and XAFS study on $(1-x)CeO_2-xNiO$ (x = 0.025 - 0.3) system in the two-step water-splitting reaction for solar H2 production. *J. Phys. Chem. Solids* **70**, 1008-1014 (2009).

49   K.-S. Kang, C.-H. Kim, C.-S. Park & J.-W. Kim. Hydrogen Reduction and Subsequent Water Splitting of Zr-Added CeO2 *J. Ind. Eng. Chem.* **13**, 657-663 (2007).

50   T. Kobayashi, S. Wang, M. Dokiya, H. Tagawa & T. Hashimoto. Oxygen nonstoichiometry of Ce1-ySmyO2-0.5y-x (y=0.1, 0.2). *Solid State Ionics* **126**, 349-357

(1999).

51   E. Ruiz-Trejo & J. Maier. Electronic Transport in Single Crystals of Gd-Doped Ceria. *J. Electrochem. Soc* **154**, 583-587 (2007).

52   H. L. Tuller & A. S. Nowick. Small Polaron Electron-Transport in Reduced CeO_2 Single-Crystals. *J. Phys. Chem. Solids* **38**, 859-867 (1977).

53   A. J. Bosman & H. J. v. Daal. Small-polaron versus Band Conduction in some Transition-metal Oxides. *Adv. Phys.* **19**, 1-117 (1970).

54   T. Otake *et al.* Nonstoichiometry of $Ce_{1-x}Y_xO_{2-0.5x-d}$ (X=0.1, 0.2). *Solid State Ionics* **161**, 181-186 (2003).

55   S. Wang, H. Inaba & H. Tagawa. Nonstoichiometry of $Ce_{0.8}Gd_{0.2}O_{1.9-x}$. *J. Electrochem. Soc.* **144**, 4076-4080 (1997).

56   S. Wang, H. Inaba, H. Tagawa, M. Dokiya & T. Hashimoto. Nonstoichiometry of $Ce_{0.9}Gd_{0.1}O_{1.95-x}$. *Solid State Ionics* **107**, 73-79 (1998).

57   S. R. Bishop, K. L. Duncan & E. D. Wachsman. Defect equilibria and chemical expansion in non-stoichiometric undoped and gadolinium-doped cerium oxide. *Electrochem. Acta* **54**, 1436-1443 (2009).

58   K. L. Duncan, Y. Wang, S. R. Bishop, F. Ebrahimi & E. D. Wachsman. The role of point defects in the physical properties of nonstoichiometric ceria. *J. Appl. Phys.* **101**, 044906 (2007).

59   W. C. Chueh & S. M. Haile. Electrochemical studies of capacitance in cerium oxide thin films and its relationship to anionic and electronic defect densities. *Phys. Chem. Phys. Chem.* **11**, 8144-8148 (2009).

60   H. J. M. Bouwmeester & A. J. Burggraaf. *Dense Ceramic Membranes for Oxygen*

Seperation. (CRC Press, 1997).

61   E. Barsoukov & J. R. Macdonald. *Impedance Spectrscopy: Theory, Experiment, and Applications*. (John Wiley & Sons, 2005).

62   M. E. Orazem & b. Tribollet. *Electrochemical Impedance Spectroscopy*. (John Wiley & Sons, 2008).

63   W. T. Welford & R. Winston. *High Collection Nonimaging Optics*. (Academic Press, 1989).

64   J. Petrasch *et al.* A 50-kW 11,000-suns novel high-flux solar simulator based on an array of Xenon arc lamps. *J. Sol. Energy Eng.* **129**, 405-411 (2007).

65   J. Jamnik & J. Maier. Treatment of the Impedance of Mixed Conductors: Equivalent Circuit Model and Explicit Approximate solutions. *J. Electrochem. Soc* **146**, 4183-4188 (1999).

66   J. Jamnik & J. Maier. Generalised equivalent circuits for mass and charge transport: chemical capacitance and its implications. *Phys. Chem. Chem. Phys.* **3**, 1668-1678 (2001).

67   T. Setoguchi, K. Okamoto, K. Eguchi & H. Arai. Effects of Anode Material and Fuel on Anodic Reaction of Solid Oxide Fuel Cells. *J. Electrochem. Soc.* **139**, 2875-2880 (1992).

68   F. Ciucci, W. C. Chueh, S. M. Haile & D. G. Goodwin. Two-dimensional electrochemical model for mixed conductors: a study of ceria. *arXiv:0707.0835 [Chemical Physics]* (2009).

69   F. Ciucci. *Continuum Modeling of Mixed Conductors: A Study of Ceria* Ph.D Thesis, California Institute of Technology, (2009).

70   H. M. Deng, M. Y. Zhou & B. Abeles. Diffusion-Reaction in Mixed Ionic-Electronic

Solid Oxide Membranes with Porous-Electrodes. *Solid State Ionics* **74**, 75-84 (1994).

71   M. L. Liu. Equivalent Circuit Approximation to Porous Mixed-Conducting Oxygen Electrodes in Solid-State Cells. *J. Electrochem. Soc* **145**, 142-154 (1998).

72   S. B. Adler, J. A. Lane & B. C. H. Steele. Electrode Kinetics of Porous Mixed-Conducting Oxygen Electrodes. *J. Electrochem. Soc.* **143**, 3554-3564 (1996).

73   F. S. Baumann, J. Fleig, H.-U. Habermeier & J. Maier. Impedance spectroscopic study on well-defined (La,Sr)(Co,Fe)O$_{3-d}$ model electrodes. *Solid State Ionics* **177**, 1071-1081 (2006).

74   F. Ciucci, Y. Hao & D. G. Goodwin. Impedance spectra of mixed conductors: a 2D study of ceria. *Phys. Chem. Chem. Phys.* **11**, 11243-11257 (2009).

75   G. W. Coffey, L. R. Pederson & P. C. Rieke. Competition Between Bulk and Surface Pathways in Mixed Ionic Electronic Conducting Oxygen Electrodes. *J. Electrochem. Soc.* **150**, A1139-A1151 (2003).

76   R. Das, D. Mebane, E. Koep & M. Liu. Modeling of patterned mixed-conducting electrodes and the importance of sheet resistance at small feature sizes. *Solid State Ionics* **178**, 249-252 (2007).

77   J. Descure, Y. Bultel, L. Dessemomd & E. Siebert. Modelling of dc and ac responses of planar mixed conducting oxygen electrode. *Solid State Ionics* **176**, 235-244 (2005).

78   J. Fehribach & R. OHayre. Triple Phase Boundaries in Solid-Oxide Cathodes. *SIAM J. Appl. Math.* **70**, 510-530 (2009).

79   J. Fleig. On the width of the electrochemically active region in mixed conducting solid oxide fuel cell cathodes. *J. Power Sources* **105**, 228-238 (2002).

80   J. Fleig & J. Maier. The polarization of mixed conducting SOFC cathodes: Effects of

surface reaction coefficients, ionic conductivity, and geomtry. *J. Eur. Ceram. Soc.* **24**, 1343-1347 (2004).

81   R. D. Green, C.-C. Liu & S. B. Adler. Carbon dioxide reduction on gadolinia-doped ceria cathodes. *Solid State Ionics* **179**, 647-660 (2008).

82   Y. Lu, C. Kreller & S. B. Adler. Measurement and Modeling of the Impedance Characteristics of Porous $La_{1-x}Sr_xCoO_{3-d}$ Electrodes. *J. Electrochem. Soc.* **156**, B513-B525 (2009).

83   M. E. Lynch & M. Liu. Investigation of sheet resistance in thin-film mixed-conductor solid oxide fuel cell cathode test cells. *J. Power Sources* **195**, 5155-5166 (2010).

84   M. E. Lynch, D. S. Mebane, Y. Liu & M. Liu. Triple-Phase Boundary and Surface Transport in Mixed Conducting Patterned Electrodes. *J. Electrochem. Soc.* **155**, B635-B643 (2008).

85   D. S. Mebane & M. Liu. Classical, phenomenlogical analysis of the kinetics of reactions at the gas-exposed surface of mixed ionic electronic conductors. *J. Solid State Electrochem.* **10**, 575-580 (2006).

86   A. M. Svensson, S. Sunde & K. Nisancioglu. Mathematical Modeling of Oxygen Exchange and Transport in Air-Perovskite-Yttria-Stabilized Zirconia Interface Regions II. Direct Exchange of Oxygen Vacancies. *J. Electrochem. Soc.* **145**, 1390-1400 (1998).

87   F. S. Baumann, J. Maier & J. Fleig. The polarization resistance of mixed conducting SOFC cathodes: A comparative study using thin film model electrodes. *Solid State Ionics* **179**, 1198-1204 (2008).

88   W. C. Chueh, W. Lai & S. M. Haile. Electrochemical behavior of ceria with selected metal electrodes. *Solid State Ionics* **179**, 1036-1041 (2008).

89   H. C. Chang & G. Jaffe. Polarization in Electrolytic Solutions. 1. Theory. *J. Chem. Phys.* **20**, 1071-1077 (1952).

90   A. Quarteroni & A. Valli. *Numerical Approximation of Partial Differential Equations*. (Springer-Verlag, 1994).

91   F. Hecht & O. Pironneau.   (Universite Pierre et Marie Curie, 2007).

92   T. A. Davis. Algorithm 832: UMFPACK V4.3---an unsymmetric-pattern multifrontal method. *ACM Trans. Math. Softw.* **30**, 196-199 (2004).

93   R. A. D. Souza & M. Martin. Using 18O/16O exchange to probe an equilibrium space-charge layer at the surface of a crystalline oxide: method and application. *Phys. Chem. Chem. Phys.* **10**, 2356-2367 (2008).

94   J. Frenkel. *Kinetic Theory of Liquids*. (Oxford Univ. Press, 1946).

95   S. Kim, J. Fleig & J. Maier. Space charge conduction: Simple analytical solutions for ionic and mixed conductors and application to nanocrystalline ceria. *Phys. Chem. Chem. Phys.* **5**, 2268-2273 (2003).

96   J. Maier. *Physical Chemistry of Ionic Materials*. (Wiley, 2004).

97   W. G. Besseler, J. Warnatz & D. G. Goodwin. The influence of equilibrium potential on the hydrogen oxidation kinetics of SOFC anodes. *Solid State Ionics* **177**, 3371-3383 (2007).

98   A. J. Bard & L. F. Faulkner. *Electrochemical methods: Fundamentals and Applications, 2nd ed.*, (Wiley, 2001).

99   D. R. Mullins, S. H. Overbury & D. R. Huntley. Electron spectroscopy of single crystsal and polycrystalline cerium oxide surfaces. *Surf. Sci.* **409**, 307-319 (1998).

100   C. M. Wang, S. Thevuthasan & C. H. F. Peden. Interface Structure of an Epitaxial Cubic

Ceria Film on Cubic Zirconia. *J. Am. Ceram. Soc.* **86**, 363-365 (2003).

101   J. Maier. Electrochemical Investigation Methods of Ionic Transport Properties in Solids. *Solid State Phenomena* **39-40**, 35-60 (1994).

102   I. D. Raistrick, J. R. Macdonald & D. R. Franceschetti. *Impedance Spectroscopy*. 59 (John Wiley & Sons, Inc., 1987).

103   J. Bisquert. Chemical capacitance of nanostructured semiconductors: its origin and significance for nanocomposite solar cells. *Phys. Chem. Chem. Phys.* **5**, 5360-5364 (2003).

104   J. Bisquert *et al.* A review of recent results on electrochemical determination of density of electronic states of nanostructured metal-oxide semiconductors and organic hole conductors. *Inorganica Chemica Acta* **361** (2008).

105   J. Fleig, J.-R. Kim, J. Jamnik & J. Maier. Oxygen Reduction Kinetics of Lanthanum Manganite (LSM) Model Cathodes: Partial Pressure Dependence and Rate-Limiting Steps. *Fuel Cells* **5** (2008).

106   T. Kawada *et al.* Determination of Oxygen Vacancy Concnetration in a Thin Film of La0.6Sr0.4CoO3-d by an Electrochemical Method. *J. Electrochem. Soc* **149**, 242-259 (2002).

107   G. T. Kim, S. Wang, A. J. Jacobson, Z. Yuan & C. Chen. Impedance studies of dense polycrystalline thin films of La_2NiO_{4+d}. *J. Mater. Chem* **17**, 1316-1320 (2007).

108   M. Sasa *et al.* Electrode reaction and microstructure of La0.6Sr0.4CoO3-d thin films. *Solid State Ionics* **177**, 1961-1964 (2006).

109   G. la O & Y. Shao-Horn. OXygen Surface Exchange Kinetics on Sr-Substituted Lanthanum Manganite and Ferrite Thin-Film Microelectrodes. *J. Electrochem. Soc* **156**,

816-824 (2009).

110   W. Jung & H. L. Tuller. Investigation of Cathode Behavior of Model Thin-Film SrTi1−xFexO3−. *J. Electrochem. Soc* **155**, 1194-1201 (2008).

111   O. Costa-Nunes, R. M. Ferrizz, R. J. Gorte & J. M. Vohs. Structure and thermal stability of ceria films supported on YSZ(100) and a-Al_2O_3(0001). *Surface Science* **592**, 8-17 (2005).

112   Y.-M. Chiang, E. B. Lavik, I. Kosacki, H. L. Tuller & J. Y. Ying. Nonstoichiometry and Electrical Conductivity of Nanocrystalline CeO_{2-x}. *J. Electroceram.* **1**, 7-14 (1997).

113   N. Sakai *et al.* Determination of hydrogen solubility in oxide ceramics by using SIMS analyses. *Solid State Ionics* **125**, 325-331 (1999).

114   D. W. Goodman, R. D. Kelley, T. E. Madey & J. J.T. Yates. Kinetics of the Hydrogenation of CO over a Single Crystal Nickel Catalyst. *J. Catal.* **63**, 226-234 (1979).

115   V. M. Gonzalez-DelaCruz, J. P. Holgado, R. Pereniquez & A. Caballero. Morphology changes induced by strong metal-support interaction on a Ni-ceria catalytic system. *J. Catal.* **257**, 307 (2008).